Physik Department

Tension and contractile activity during adult muscle formation in *Drosophila*

Dissertation

von

Martina Lindauer

Technische Universität München

TECHNISCHE UNIVERSITÄT MÜNCHEN

Lehrstuhl für Biophysik E27

Tension and contractile activity during adult muscle formation in *Drosophila*

Martina Lindauer

Vollständiger Abdruck der von der Fakultät für Physik der Technischen Universität München zur Erlangung des akademischen Grades eines

Doktors der Naturwissenschaften (Dr. rer. nat.)

genehmigten Dissertation.

Vorsitzender: Univ.-Prof. Dr. M. Zacharias

Prüfer der Dissertation:

1. Univ.-Prof. Dr. A. Bausch
2. Univ.-Prof. Dr. M. Rief

Die Dissertation wurde am 03.09.2015 bei der Technischen Universität München eingereicht und durch die Fakultät für Physik am 24.09.2015 angenommen.

Abstract

In higher-order animals, including humans, muscles are involved in a multitude of body functions such as the heart beat, gut motility and locomotion. Only a thorough understanding of muscle development and functionality will enable us to treat and ultimately cure muscle diseases. A major aspect requiring clarification is the fundamental mechanism that causes the development of the highly ordered internal muscle structure. This work aims to extend our knowledge of tension and contractile activity in muscle formation by means of optical severing experiments on developing adult muscles in the model organism *Drosophila melanogaster*. Target properties are inferred from the response to a lesion that is created by a focused laser.

In a first step, an adequate nanodissection device is selected, improved to adapt to all requirements, and set up. It uses a laser with 350 ps pulses and a wavelength of 355 nm to create lesions by means of *laser-induced plasma formation*. Software controlled mirrors move the laser focus to user-defined positions in the field of view of simultaneously working bright field and spinning disc confocal microscopes. A performance analysis reveals the good quality of the setup: The variability of the laser intensity throughout the fields of view is sufficiently small and the precision of the cuts is as good as in comparable setups.

The second part of the thesis is dedicated to the investigations of tension and contractile activity in two functionally, structurally, and developmentally differing adult muscle groups of *Drosophila*: dorsal-longitudinal muscles (DLMs) and dorsal abdominal muscles.
Optical severing of DLM tendons was performed. A combination of qualitative analysis steps and a quantitative evaluation of the retraction velocity is established. It reveals a retraction of structures along severed tendons away from the target site, demonstrating the presence of tension during the developmental process of myotube compaction/tension elongation. This finding extends the period of time in DLMs for which tension has been confirmed [92].
In order to ultimately investigate myosin II for its contribution to tension formation in DLMs, the effect of the myosin II inhibitor (-)-blebbistatin on DLM development is tested. The application of this chemical required the development and testing of a new protocol. A visible phenotype with inhibited transportation mechanisms is ascribed to the blebbistatin solvent dimethyl sulfoxide (DMSO) and not to blebbistatin itself.
Microtubule bundles are a candidate for tension transduction and maintenance. Optical severing of microtubule bundles in DLMs is used to test for tension in these cyotskeletal structures. Due to difficult imaging conditions, cut edges were the only region of the severed bundles that could be analyzed. Their retraction velocity was estimated to be in the range of depolymerization. Hence, a final conclusion about tension in microtubules cannot be drawn.

Besides the findings on tension in DLMs, it is indispensable to investigate tension in

a second muscle type, the tubular abdominal muscles, which are considered to resemble skeletal muscles in vertebrates. The technique of nanodissection and a reliable method to qualitatively confirm tension and contractile activity in the relatively thick dorsal abdominal muscles is established. The response of dorsal abdominal muscles to optical severing reveals interesting aspects concerning tension and contractile activity. For early developmental time points, at 36 h and 40 h after *puparium* formation (APF), the analysis of retraction behavior of cut edges, structures along the muscles and muscle ends/attachments confirms passive tension. This demonstrates, in combination with its presence in DLMs, that tension is not unique to the specialized fibrillar muscle type (DLMs) but a universally occurring feature in developing muscles.

At later time points (46 h and 52 h APF), optical stimulation results in contractile movements (*induced contraction*). This potentially active process renders tension evaluation impossible. Nevertheless, a passive mechanism is also conceivable. Further investigations are necessary for distinguishing between the two options. The occurrence of inherent muscle contraction at relevant time points is analyzed. yet, the slight but increasing activity observed between 46 h and 51 h APF is not suitable to classify *induced contraction* as an active or a passive mechanism.

Further insights for discerning, whether induced contraction is active or passive, are expected from the investigation of calcium ion (Ca^{2+}) behavior. Ca^{2+} is analyzed with the help of the cytosolically expressed artificial reporter protein GCaMP6f, which fluoresces upon binding of calcium ions. The observed Ca^{2+} influx upon optical stimulation at 40 h and 46 h APF points towards two important conclusions. First, it strongly indicates that *induced contraction* is an active process. Second, the calcium machinery is present before the functional switch from non-contractility to contractility takes place.

The findings made in abdominal muscles are especially interesting in the context of structural changes, which were investigated by our collaboration partners Dr. Manuela Weitkunat and Dr. Frank Schnorrer from the Max Planck Institute of Biochemistry (Martinsried, Germany). We find that in dorsal abdominal muscles tension accompanies pre-myofibril formation and contractile activity precedes sarcomeric order. This suggests a causal chain, where immature myofibril formation relies on passive tension, while sarcomeric pattern formation is enhanced or even exclusively triggered by contractile activity.

Contents

List of Figures

List of Abbreviations

$< P_0 >$	mean laser output power
$< P_{\mathrm{BFP,+filter}} >$	mean laser power at objective BFP as measured with inserted neutral density filter
$< P_{\mathrm{BFP}} >$	mean laser power in front of objective BFP
$< P_{\mathrm{sample}} >$	mean laser power delivered to sample plane
λ	wavelength
θ	angle of deviation of laser beam off the opical axis
$\triangle$	variation in energy deposited in the sample
d_{bead}	bead diameter
E	energy
T_{NDD}	overall transmission of NDD
$T_{\mathrm{objective}}$	transmission of objective
$v_{\parallel}$	*parallel velocity*
v_{abs}	*absolute velocity*
AMP	adult muscle precursors
AOM	acousto-optical modulator
AOTF	acousto-opical tunable filter
APF	after *puparium* formation
ATP	adenosine triphosphate
BFP	back focal plane
ddH_2O	purified water
DLM	dorsal-longitudinal muscle
DMSO	dimethylsulfoxide
duf	dumbfounded, a *Drosophila* gene
FC	founder cell
FCM	fusion competent myoblast
FGF	fibroblast growth factor
fps	frames per second
GFP	green fluorescent protein
Gma	globular moesin actin binding domain
IFM	indirect flight muscle
IR	infrared
mhc	myosin heavy chain
NDD	nanodissection device
NMJ	neuromuscular junction
ROI	region of interest
SD	spinning disc
SR	sarcoplasmic reticulum
UV	ultra-violet

1. Introduction

All higher-order animals possess a plethora of muscles that have adapted to specific tasks. Not only do they drive locomotion, they also promote digestion, enable breathing and form the core of our bodies, the heart. A proper development and maintenance of muscle structure and functionality is crucial for health and survival.
Like all other tissues in a body muscles evolve from a single fertilized cell that develops into a multi-cellular organism. During muscle development, an abundance of developmental steps need to take place in the correct way in order to form functional myofibers. Cells have to proliferate, differentiate, fuse, attach to surrounding tissues, build their highly ordered ultra-structure consisting of sarcomeres, and maintain or adapt their established structures during the life span of the animal. It is of particular interest to understand muscle architecture, functionality and the underlying developmental processes in order to cure muscle injuries and diseases. Great efforts in this field of research over the past 50 years have led to a significant extension of our knowledge. This was facilitated by major progresses in genetics in combination with model organisms such as *Drosophila melanogaster*. Nowadays a large pool of genetic tools and hence genotypes provide a prolific background for studies. Due to the high conservation among species that was found for muscle composition and the underlying functional principles [62] results from *Drosophila* have helped to extend our understanding of muscle development.
The current picture of *Drosophila* adult muscles includes a solid knowledge of participating proteins. However, their function often remains elusive [84], and developmental steps are often not sufficiently investigated. To a great extent, models lack the mechanisms that drive the different structural and functional changes during muscle development. Tension as well as contractile activity have long been suggested by experimentalists as well as theoreticians to be important for myofibrillogenesis and sarcomerogenesis [20, 75, 94]. Only recently, *in vivo* experiments directly prove the existence of evolving tension and its major role in *Drosophila* muscle development [92].
However, in the framework of current understanding these investigations raise some questions, which inspired this thesis: Tension in *Drosophila* dorsal-longitudinal muscles (DLMs) was investigated until the early stages of attachment maturation almost three days before eclosion [92]. It is unclear, whether tension remains permanently after its initial evolution or if it is a transient factor. Moreover, the molecular contributors are still to be identified and confirmed. Observations made by Weitkunat et al. [92] were restricted to DLMs, which are structurally and functionally different from most other *Drosophila* muscles and also from vertebrate skeletal muscle [66]. Hence it is unclear whether tension is universally necessary for muscle formation or if it is unique to DLM (fibrillar muscle) development. Finally, the role of contractile activity as opposed to passive tension remains to be investigated in live *Drosophila* muscle development.
For this thesis two structurally and functionally differing adult muscle groups in *Drosophila* were chosen on which to investigate the aforementioned aspects, DLMs and dorsal abdominal muscles. The method of investigation was optical severing by means of *laser-induced*

plasma formation. Here, (visco-elastic) properties of the target material are inferred from the response of the target structure to a cut. In the following a short overview of the thesis is given:

- In order to be able to perform non-invasive tension measurements in *Drosophila melanogaster* via the analysis of target responses to optical severing [14, 92], a nanodissection device (NDD) including confocal fluorescence and bright field microscopes was built. Custom written control software was implemented. The NDD design as well as theoretical background information on the underlying physical principle of cutting by producing a *laser-induced plasma* are presented in chapter 2. After having set up the NDD its quality was tested in two model systems. Glass cuts revealed the physical dimensions of the smallest possible cuts as well as their homogeneity throughout the field of view. *In vitro* keratin networks were used to analyze different cutting regimes.

- Background information on *Drosophila* adult muscle development is given in chapter 3. It focuses on DLMs and dorsal abdominal muscles, the two muscle systems that were investigated in the course of this thesis.

- Chapter 4 is dedicated to the description of experiments and their results. In the first section optical severing was applied to DLM tendons in order to extend the knowledge on tension evolution and creation in this muscle-tendon system. Measurements were performed at a later developmental time point than previously investigated [92]. An appropriate analysis technique was established. Moreover, myosin and microtubules were tested as potential molecular candidates for tension support. In the case of myosin a protocol for chemical inhibition of the system via blebbistatin was tested. A potential tension on microtubule bundles was investigated with the technique of nanodissection.

- The second part of chapter 4 describes the results obtained in dorsal abdominal muscles. Optical severing at different developmental time points revealed tension and contractile movements. The survey of calcium ion fluxes during severing processes enabled the classification of contractile movements as active rather than passive. A comparison of the results on functionality with structural stages, which were investigated by our collaboration partners Manuela Weitkunat and Frank Schnorrer (Max Planck Institute of Biochemistry, Martinsried) is given.

- Finally chapter 5 provides a thorough discussion of the results, which yielded intriguing conclusions concerning cause and effect in the interplay of structure and functionality in developmental processes. The findings are an important step towards a better understanding of muscle development and functionality. Due to the complexity of the system the road to go is, however, still long. Therefore, this last chapter also includes an outlook on further interesting questions and experiments that will continue the work on the presented topics.

2. Nanodissection device

Optical severing, also referred to as laser micro- or nanosurgery and nanodissection, has been proven to be a versatile tool in examining biological samples [14, 15, 41, 44]. The technique of optical severing is a so-called non-invasive technique, because it allows to perform cuts inside otherwise inviolate living samples, from small cells up to whole organisms [14, 15, 41]. Different technical implementations were used to achieve precise optical severing of structures in different live organisms and in structures of different size. It is for example possible to cut single microtubules [15] or stress fibers [41] in animal cells, and *Drosophila* embryonic tissue mechanics were investigated by severing single cells [44].
Intending to investigate muscle development in *Drosophila melanogaster* (section 4) a nanodissection device was built. Besides the theoretical background of the technique this chapter describes the design of the setup and its performance.

2.1. Nanodissection: Theoretical background

The theoretical background of nanodissection has been extensively studied in the last decades. Nevertheless, major aspects are still in discussion. Here, an overview of the physical principles is given, focusing on the technical implementation that was used to build the setup described in this thesis.

Physical principles of laser-tissue interactions Laser-tissue interactions may be classified according to the underlying physical principle, that causes changes in the target. Following Niemz [49] these processes are *photo-chemical interactions*, *thermal interactions*, *photoablation*, *plasma-induced ablation*, and *photodisruption*.[1] These regimes were found to depend on laser but also on target properties. Laser-tissue interaction is mainly determined by the power density[2], i.e. the pulse duration and the energy density[3] of the pulse [49].
Photo-chemical interactions occur at very low power densities, typically with CW lasers and exposure times of seconds [49]. The term describes structural or chemical changes of molecules caused by light, as they occur e.g. during photosynthesis in plants [49]. *Photo-chemical interactions* do not directly destroy target material [49]. *Thermal interactions* depend on an increase of the temperature in the target [49]. This leads to typically non-specific effects, such as coagulation, vaporization, carbonization, and melting [49]. Although both regimes are used in medical applications [49], they are not suitable for nanodissection. Their time scales are too long and the effects too widespread.
Photoablation describes the direct dissociation of chemical bonds by absorption of photons with sufficient energy, typically around 3.5 eV. This happens with wavelengths in the ultraviolet (UV) range. It may be achieved with laser pulses in the range of approximately 10^7

[1] Nomenclature in literature varies. The terms that are introduced here and used in this thesis follow the suggestion of Niemz [49]. They were also used for example by Colombelli and coworkers [14, 15].
[2] Power per area, also called irradiance.
[3] Energy per area.

- 10^8 W/cm^2. [49]
When power densities are beyond a certain, material specific threshold, *laser-induced plasma formation* occurs [49, 51]. Due to its precision and applicability in otherwise transparent media [14, 49] this effect is usually used for nanodissection and will be explained in more detail in the following paragraph. *Laser-induced plasma formation*, however, causes secondary effects such as shock waves, cavitation bubbles and jet formation, the latter two only in soft tissues and liquids [49, 50]. The term *photodisruption* summarizes these side-effects. For precise cuts in the sub-micron regime confined laser-induced plasmas are most suitable, but, depending on the intended experiment, *photodisruption* is not necessarily a disadvantage.

Laser-induced plasma formation A plasma forms, when the electric field (in this case of the laser beam) exceeds the ionization energy of the target material and quasi-free electrons are created [49, 51]. This event is also referred to as *optical breakdown*, because the absorption coefficient for the laser radiation rises drastically in the plasma [51]. The absorption determines the amount of energy, that is deposited in the sample and enables optical severing of the target even when the material is otherwise transparent [49, 51]. Thus, if a sample is sufficiently transparent to the chosen wavelength, a target well below the surface of the sample may be severed without damaging the more superficial regions. The plasma energy density in turn holds responsible for the severity of the secondary effects: The more energy is absorbed, the more energy is available for *photodisruption* [15, 49, 51]. Here, not only the absorption is important but also the energy density, that has to be exceeded to produce a plasma (breakdown threshold). The threshold for *optical breakdown* was found to depend on laser pulse duration: A decrease from several tens of nanoseconds to femtoseconds reduces the threshold energy density of distilled water, which is often used as a model system to study optical breakdown, by a factor of 10^3 [87]. The corresponding power density, however, usually increases due to the short pulse durations. Other inorganic as well as biological materials show an equivalent behavior [48].
The origin of this behavior is considered to be found in the underlying processes of quasi-free electron generation and quenching. Generation of quasi-free electrons may occur by means of thermionic and multi-photon emission. Additionally, avalanche ionization, which relies on seed electrons, occurs. Losses are due to inelastic collisions and electron diffusion out of the focal volume. [48, 51]
Explanations for the energy density behavior of the breakdown threshold are based on numerical solutions of a rate equation that includes electron generation and quenching processes [48, 51]. However, different authors could reasonably reproduce experimental findings with different assumptions for electron generation. Niemz [48] only considers avalanche ionization on the basis of a thermally produced initial electron density. With this assumption, the solution of the rate equation already follows experimental observations. Noack and Vogel [51], however, include avalanche ionization as well as multi-photon ionization and thermionic emission (only when impurities are present). Due to the time-constraints of avalanche formation during short pulses they find multi-photon ionization an increasingly important process for the reduction of the energy density threshold for optical breakdown with decreasing pulse durations. With these assumptions, it is the interplay between multi-photon and avalanche ionization in combination with the available time for

quasi-free electron generation (pulse duration) that leads to a decreased breakdown energy threshold for shorter pulse durations. Moreover, they find that infrared but not visible wavelengths show a difference in the breakdown threshold for pure and impure material. Hence, further experiments and theoretical calculations in this field are necessary until the process is fully understood.

Selection of technical implementation The options among which to select an appropriate technique for nanodissection in *Drosophila* pupae are manifold: Laser wavelengths λ ranging from the ultra-violet (UV) to the infrared (IR) and pulse durations between femtoseconds and nanoseconds have been used to optically sever different types of materials, solids as well as liquids [15, 49, 51]. The technique of choice should be well established, reliable, and cost-efficient, and it should use readily available components.
Among all these possibilities for the implementation of a nanodissection device especially the setup by Colombelli and coworkers [14] has proofed to be useful at different length scales and in many different biological tissues. It was for instance used to cut the cell cortex in *C. elegans* zygotes [45], to disintegrate amnioserosa cells during dorsal closure in *Drosophila* embryos [74], to cut whole tendon cells in *Drosophila* pupae [92], and to delicately sever single microtubules in cells [15].
In the setup introduced in [14] a UV-A ($\lambda = 355\,\mathrm{nm}$) laser with half nanosecond pulses is focused to a diffraction limited volume. A short wavelength makes sense because it enables smaller focal volumes [14]. As it is the intention to work in biological samples, smaller wavelengths are not an option. The absorption of UV-B and UV-C light by proteins and DNA at wavelengths between $\lambda_{\mathrm{peak}} = 190\,\mathrm{nm}$ and $\lambda_{\mathrm{peak}} = 280\,\mathrm{nm}$ would lead to undesired damages. Moreover, UV-C and smaller wavelengths would require special optical elements, which are expensive, not readily available and therefore not practical.
The setup is capable of producing diffraction limited plasmas and has demonstrated to be as versed in precise cuts as other setups with shorter pulses [15]. With respect to the theoretical and experimental considerations presented in the previous paragraph, this is surprising. Shorter pulses were expected to produce less secondary effects. This may indeed hold true for single pulses because the required pulse energy is smaller for shorter pulses. In many experiments with shorter pulses, however, a much higher number of pulses and thus a higher total amount of energy was used [15]. The potentially higher total amount of deposited energy might account for the surprisingly comparable results and seem to be the critical factor for precise cuts. [15]
All in all, the capability to precisely sever tissue in *Drosophila* embryos and pupae and the relative simplicity as compared to systems with ultra-short laser pulses [29] suggest the use of the setup by Colombelli and coworkers.

2.2. Setup design

The custom built nanodissection device (NDD) is based on the construction concepts of similar devices by Colombelli *et al.* and Oswald [14, 52], where a dissection laser is coupled into a conventional inverted microscope. However, the newly constructed NDD was realized in a different way in order to improve the functional range, particularly with regard to the pending experiments. This section gives an overview of the system design and important engineering and design considerations. A detailed list of setup components and their rele-

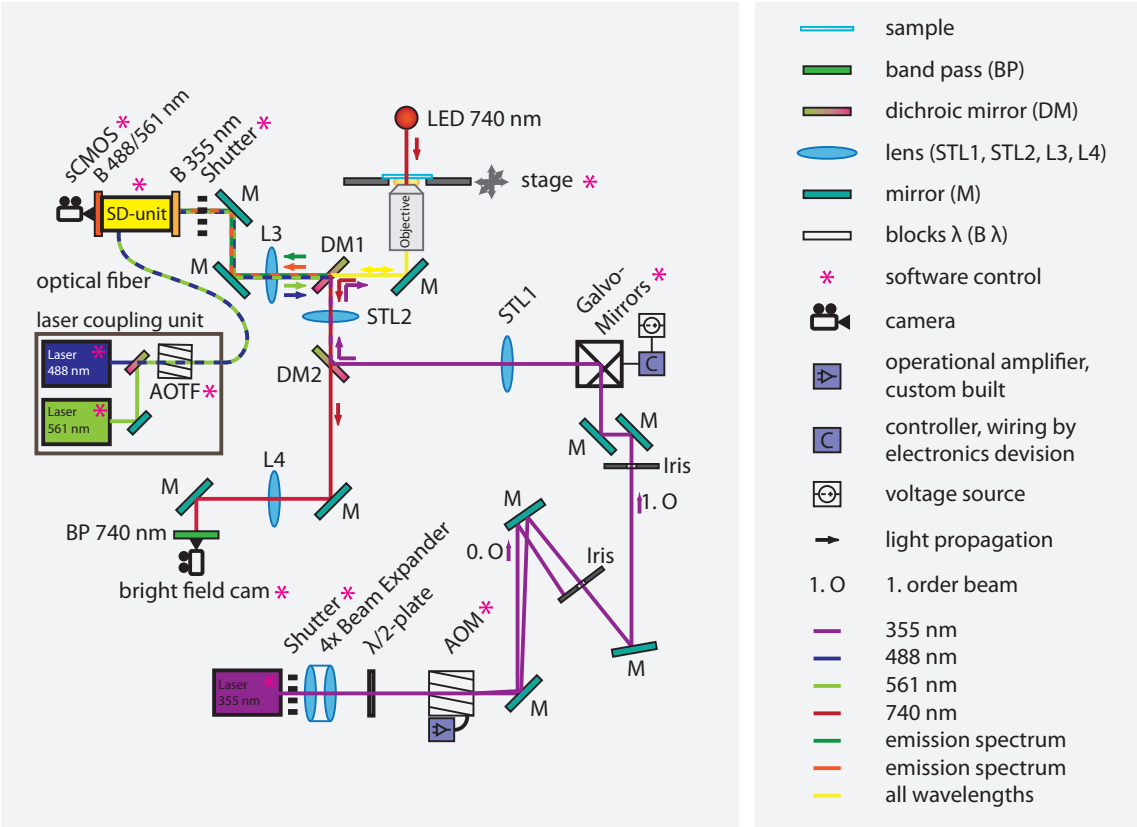

Figure 2.1.: Schematic of the custom built NDD.

vant specifications as well as software annotations can be found in section C.

As can be seen in fig. 2.1 the NDD consists of three functional parts: a confocal spinning disc unit for fluorescence microscopy, a bright field microscope and a passively Q-switched 355 nm Nd:YAG Laser, which is used for cutting. The sample is mounted on a motorized xy-stage with z-piezo, which may be controlled manually (joystick) or by software. The xy-plane is the imaging plane, the z-direction corresponds to the optical axis. Via a dichroic mirror (DM1) all three light paths couple into an exchangeable, vertically installed objective. DM1 was chosen to reflect all but those wavelengths used in the confocal path. Currently a 63x1.40 Oil λ blue and a 63x1.20 W objective (Leica Microsystems) are in use. However, due to the infinity correction of the objectives it is possible to use other infinity corrected objectives[4].
The cutting pathway starts with the 355 nm cutting laser. It emits non-collimated light pulses with repetition rates between 10 Hz and 1000 Hz, 350 ps puls length, 27 mW average power (1000 Hz) and 70 kW peak power. The mean pulse energy is 27.0 µJ at 1000 Hz repetition rate. It is collimated in a 4 x beam expander to a beam with a diameter of 2.5 mm.

[4]Objectives preferentially have an equally positioned back focal plane to ensure the homogeneity of delivered laser power throughout the xy-plane (see text below).

The beam diameter needs to be within a certain range, because its upper and lower limits are determined by the aperture and the damage threshold of the following acousto-optical modulator (AOM) . The AOM is used to regulate laser intensity. Polarization direction is optimized with a $\lambda/2$ plate in order to have a high yield in the acousto-optical modulator. The working principle of the AOM is based on Bragg diffraction [1]: A high frequency acoustic wave is used to create a refractive index pattern in a crystal, which then causes a diffraction pattern in the light - the laser beam splits into several maxima. Their intensities depend on the amplitude of the acoustic signal. Thus, the laser intensity in the sample can be accurately regulated in nanoseconds by using the calibrated first order beam of the AOM. To separate the first order beam, the beams travel a sufficient distance before a pin hole selects the first order beam and blocks all other orders. After passing a beam walk (two mirrors allowing for adjustments in all degrees of freedom) the light passes a pair of software controlled galvanometric mirrors. The two mirrors deviate the beam in two perpendicular axes, one mirror for movement in x-direction, and one for movement in y-direction. The working principle of these mirrors is based on magnetism. The mirrors are connected to magnetic circular springs which deform, and thus move the mirrors, according to the applied magnetic field. After being deflected by the galvanometric mirrors the laser beam passes the scanning telescope (lenses STL1 and STL2). The telescope is positioned in such a way that its back focal plane is in the center plane of the galvanometric mirrors. Its front focal plane coincides with the back focal plane of the objective. Thus, a deviation of a certain angle θ of the beam in the back focal plane of the telescope is translated into a tilting of the beam in the back focal plane of the objective. The objective translates this tilt into a displacement of the focal spot off the optical axis, i.e. a change of the focus position in the xy-plane. Aberration effects in telescope lenses were identified as the main source of focus intensity inhomogeneities throughout the field of view [52]. To minimize such aberration effects STL1 was chosen to be a telecentric f-theta lens. As opposed to standard lenses in these specialized scanning lenses the position of the focal volume depends on the incident angle θ, and the focal plane is also flat for deflected incident beams [76]. These characteristics make positioning much easier, especially for beams that are not deflected in the focal plane of the lens as in the case of the NDD. Additionally the telescope widens the beam to its final size. However, deflection outside the focal plane of STL1 still leads to slight but bearable variations in focus intensity. This is due to the fact that the point of beam tilting is slightly in front of or behind the back focal plane of the objective and therefore, depending on the tilting angle, different parts of the beam cross section enter the objective. Nevertheless, this drawback is preferred over additional imperfections resulting from two single mirror systems with an additional scanning telescope in between.
The confocal path contains a commercially available Nipkow-spinning disc (SD) unit. To this end two imaging lasers, 488 nm and 561 nm, are installed. Together with the corresponding dualband filter in the spinning disc unit this allows for imaging of fluorophores of two different λ-regimes, one in the range of green fluorescent protein (GFP) (excitation: $\lambda = 488\,\mathrm{nm}$) and one in the range of Cherry (excitation: $\lambda = 561\,\mathrm{nm}$). Laser coupling and intensity regulation is realized with an acousto-optical tunable filter (AOTF). It is based on the same principle as the AOM, but is capable of selecting and regulating several different wavelengths simultaneously. For imaging an Andor Neo sCMOS Camera was installed on the SD unit. Camera, spinning disc unit and laser coupling unit, including imaging lasers and AOTF, were purchased from Acal BFi Germany.
Except for the laser combining unit of the SD system, which is installed on a separate

table, all optical components are installed on an optical table on four isolators. The system includes a wheel construction, which allows for easy lifting (without turning) and moving of the whole table with all components installed.
The bright field microscope is realized with a 740 nm LED illuminating the sample from above. By choosing such a long wavelength, it is possible to do bright field and confocal imaging simultaneously without creating disturbing crosstalk between both imaging channels. The telescope of the bright field path consists of STL2 and L4, which are installed in such a way that a 63x magnification is achieved on the bright field CMOS camera.

A software called *TSE04_ GK.vi* was written in LabVIEW (National Instruments) to operate the electronic devices, namely the cutting laser, the AOM, the galvanometric mirrors, the SD unit, the imaging lasers and the AOTF, the safety shutters, and the motorized piezo-stage. The cameras are controlled via the respective enclosed software packages. The software *DC480 viewer* (Thorlabs) controls the bright field camera completely independently from other devices. The Neo sCMOS camera is controlled via the enclosed software *Solis* (Andor Technologies) enabling access to all camera features, e.g. live imaging and recording. Figure 2.2 shows a screenshot of the *TSE04_ GK* and *Solis* user interfaces. After starting *TSE04_ GK* the user sets all parameters concerning the SD unit and one imaging laser (disc rotation velocity, shutter position, wavelength, intensity). The second imaging laser is included in the software triggering but its intensity is manually controlled via an external power supply.[5] The cutting laser is initialized on user request. The sample can be positioned via the joystick or via *TSE04_ GK* while using the live mode of *Solis*. A *Solis* macro was written to save the currently displayed image in *Solis* to a BMP-file, which is then, upon manual actualization, shown in the *TSE04_ GK* image window. To perform a cut (with or without movie acquisition) the user specifies the target by drawing the required 3D lines and/or points in the still image and setting the cutting parameters. As it is a pulsed laser, a line will always be composed of several individually targeted points. Therefore, the user sets the laser intensity (AOM voltage), the distance between the points composing a line, and the number of pulses per point. If movie acquisition is desired, the acquisition parameters need to be set in *Solis* before movie acquisition is triggered externally with the start of the laser cutting procedure.
To this end, besides z-stacks in confocal mode, it is possible to perform line and point cuts in 3D, bright field imaging, and confocal imaging simultaneously, which was not possible with former setups proposed in [14, 52]. Now there is no blind time between cut and imaging start anymore. Previous setups [14, 52] based on conventional microscopes needed to move the sample in z-direction between cutting and imaging to correct for differences in focal planes of imaging and dissection wavelengths. This drawback was caused by chromatic abberrations. For two imaging modes of the NDD, it was overcome by almost completely separating imaging and cutting pathways. The cutting pathway shares only two optical components with the imaging pathway. First, this enabled optimization of all optical components for the respectively necessary wavelengths and not only for the visible wavelengths, as it is the case in conventional microscopes. This reduces disturbing effects. Second, the optical components were installed in such a way, that the focal plane of the cutting laser and the focal planes of two imaging pathways, bright field and confocal GFP imaging, co-

[5] Because of the limited number of 4 analog output channels of the PCIe card changing between the two imaging lasers and intensity control of one laser has to be done manually.

incide. The implemented improvements are especially important for the analysis of initial recoil behavior and for classifying the quality of the cut (see sections 2.1 and 2.3.4), the latter being crucial when precise cuts are desired.

2.3. Performance

Several experiments were performed in order to reveal the quality of the cuts produced with the nanodissection device (NDD). The most relevant parameters are the focus size, the percentage of laser power that is transmitted to the sample plane, the homogeneity of delivered laser power throughout the xy-plane, and the different cutting regimes. In the following subsections the performance of the NDD is presented.

2.3.1. Laser power delivered to sample plane

Although the mean laser output power $< P_0 >$ is known from the specification sheet of the laser, not all of this initial power reaches the sample. A lot of laser power is lost on the way through the many components in the optical path. Hence, the laser power, that is delivered to the sample plane ($< P_{\text{sample}} >$) needs to be evaluated. Due to the high numerical aperture of the objective and the geometrical constraints of the sensor a direct measurement of laser power after the objective was not possible. Therefore, $< P_{\text{sample}} >$ was calculated as that fraction of the mean laser power right before the back focal plane (BFP) of the objective ($< P_{\text{BFP}} >$) that is transmitted by the objective:

$$< P_{\text{sample}} >= T_{\text{objective}} \cdot < P_{\text{BFP}} >,$$

where $T_{\text{objective}}$ is the transmission of the objective according to its specifications.
The mean power in front of the objective was measured as described in section C.2. The measurement was performed with a neutral density filter inserted, that was necessary for laser power measurements but removed for all other experiments. The real mean power at this position ($< P_{\text{BFP}} >$) was then calculated from the measured value $< P_{\text{BFP,+filter}} >$ using the transmission value of the filter evaluated in section C.2:

$$< P_{\text{BFP}} >= \frac{< P_{\text{BFP,+filter}} >}{T_{\text{filter}}}.$$

$< P_{\text{BFP}} >$ was found to be $5.05 \pm 0.08\,\text{mW}$ which corresponds to an energy (E) of $5.05 \pm 0.08\,\mu\text{J/pulse}$. The transmission of $T_{\text{objective}}(355\,\text{nm}) = 40\,\%$ (specification according to technical support, no error available) applies for both the water and the oil objective used with the NDD. Hence, the energy delivered to the sample plane is $< E_{\text{sample}} >= 2.02 \pm 0.03\,\mu\text{J/pulse}$. Reversing this result, the overall transmission of the NDD may be specified as $T_{\text{NDD}} = 7.48 \pm 0.12\,\%$ for both objectives.

2.3.2. Focus size extracted from glass cuts

The size of the focal spot is an important parameter for precise cuts. It limits the minimal lesion size, that can be produced in a sample. Theoretically, the NDD is capable of focusing the cutting laser beam to a diffraction limited volume, where a plasma is generated [14]. A simple method presented by Colombelli *et al.* was used to investigate the size of the produced plasma [14]: The laser is focused into a conventional glass cover slip, where a plasma

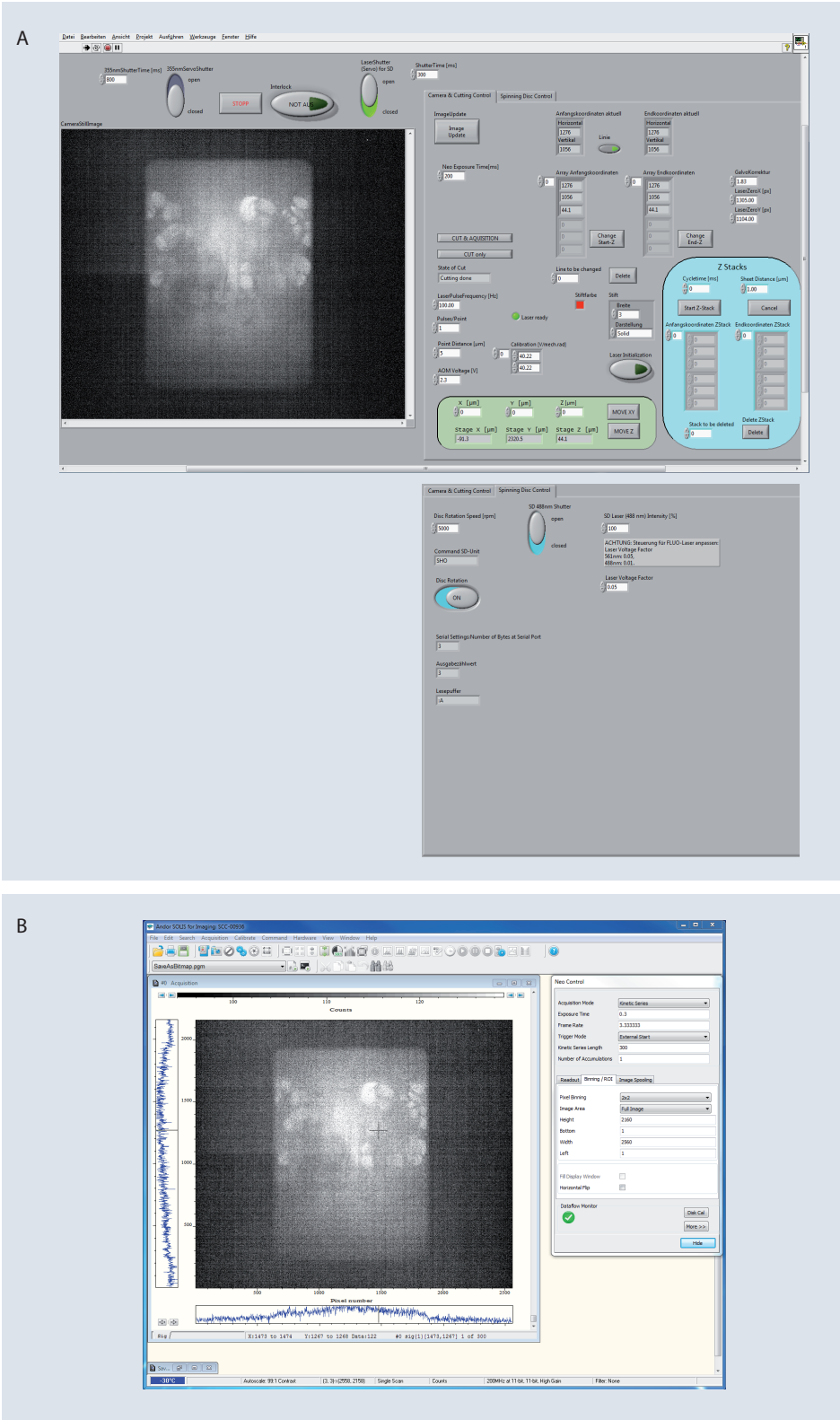

Figure 2.2.: Screenshots of software user interfaces. A| The custom written LabVIEW software *TSE04_GK*. B| The camera software *Solis* (Andor). For nanodissection both programs are used together.

is generated. The plasma changes the refractive index of the glass permanently. Thus, after such a glass cut the size of the plasma can be extracted from bright field z-stacks of the glass volume, where the refractive index has changed.
At low laser powers no noticeable effect was induced. With medium laser powers right above the plasma threshold ($< E_{\text{sample}} > \approx 0.51\,\mu\text{J/pulse}$) the setup was capable of producing confined cuts in glass. The size of the plasma increased with laser power and finally led to concomitant cracks around the focal spot. The smallest possible plasma size was evaluated from the smallest, yet visible glass cut at approximately $0.51\,\mu\text{J/pulse}$ (approx. 1.35 kW peak power).
The method of extracting the plasma size from bright field images of glass cuts requires a correct interpretation of the images. From theoretical and experimental observations the plasma volume is expected to be approximately ellipsoidal with the long axis parallel to the optical axis (z-axis) [14]. While the extraction of the diameter of a spherical or ellipsoidal object is relatively easy in the xy-plane, it is challenging for the z-direction. This is readily seen from a bead shown in fig. 2.3. The polystyrene bead (Bangs Laboratories, Inc.) with a known diameter of $1.0 \pm 0.1\,\mu\text{m}$ was embedded in a polyacrylamide gel to suppress disturbing Brownian motion [33] during bright field imaging (GSD system with 160x Oil objective; Leica microsystems). In the imaging planes (xy-planes) the bead appears as a clear pattern of concentric, alternating maxima (bright) and minima (dark) (see fig. 2.3 A^1-A^4). When approaching the bead in positive direction along the z-axis (the opposite direction as the imaging light), the pattern starts with a bright center with a first dark and a second bright ring around it (fig. 2.3 A^4). The pattern has a low contrast. With increasing z (fig. 2.3 $\text{A}^3 \rightarrow \text{A}^2 \rightarrow \text{A}^1$) the contrast increases while the diameters of the central maxima and its rings decrease to a minimum. Behind a certain z-level (switching level), the center gradually turns dark, but the size of the dark ring only increases further down the z-axis. The pattern along the z-axis is shown in an image of the xz-plane through the center of the bead (fig. 2.3 A^6). It was derived from the z-stack of xy-planes. Here, the decrease of the pattern diameter towards the switching zone is easily recognizable. It is, however, not at all clear, where in these pattern the bead actually sits and which structures determine the true size of the bead. This problem holds also true for plasma size analysis. However, as the pixel size in the image was calibrated (ex factory) and the bead had a defined diameter $d_{\text{bead}} = 1\,\mu\text{m}$, it is conceptually possible to identify those structures in the z-stack that reveal the real dimensions of the imaged bead. This knowledge will then be transferred to plasma analysis.
The real diameter d_{bead} of the bead was found in the diameter of the first minimum (ring) of xy-images close to the switching level: A line profile through the center of the bead (xy-plane) shows, that the profile minima are d_{bead} apart (fig. 2.3 A^5). As d_{bead} is represented by the minimal diameter of the first dark ring, the extraction of d_{bead} is very robust with respect to underestimations. For any z-level the extracted diameter will not be smaller than the real diameter.
There was no pronounced structure in the xz-plane that could be unambiguously identified to represent d_{bead} in z-direction. However, the xz-pattern shows a core region, where the central maximum is brightest (see fig. 2.3 A^6). The size of this bright core region is larger than d_{bead}, thus representing an upper boundary for it.

Figure 2.3 B^1-B^6 shows the region of a cover slip that had been subject to plasma formation (63x1.20 Water objective). The result was a change in the refractive index of a small

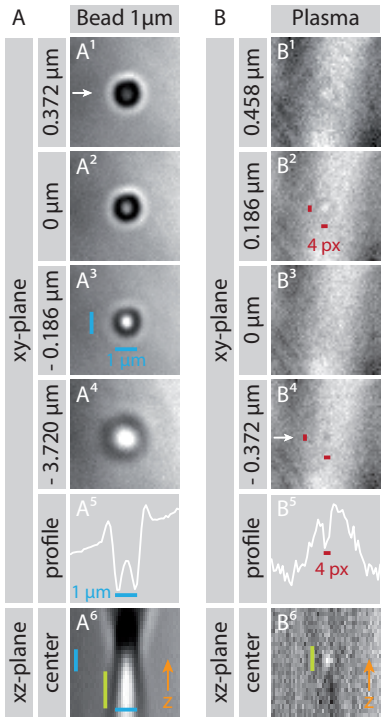

Figure 2.3.: Minimal plasma size of NDD. A^1-A^6| The pattern of a bead with known diameter was analyzed for reference. B^1-B^6| Analysis of the smallest, yet visible plasma size. A^1-A^4, B^1-B^4| Bright field images (xy-plane) at different z-levels before (A^4-A^3, B^4), at (A^2, B^3) and behind (A^1, B^2-B^1) the switching point. A^5, B^5| Profiles of horizontal lines in A^1 and B^4 indicated by white arrows. Orange arrows indicate z-axis (imaging light propagates in $-z$ direction, laser of NDD propagated in $+z$ direction). Green bars show extent of core region (highest intensity values). Blue bars indicate extent (1 µm) and position of bead. Red bars indicate extracted plasma size in xy (4 px) and xy-position of the plasma.

volume. The xy-extent of the glass cut was extracted by analysis of the representing structures, which were identified for the reference bead. Bright field z-stacks of the plasma region in the glass slide revealed an equivalently shaped but inversely colored pattern, presumably caused by a different ratio of refractive indexes of surrounding material and structure of interest (polyacrylamide gel and polystyren as opposed to normal glass and plasma-changed glass). Nevertheless, it was considered reasonable to extract an upper limit for the plasma size in the xy-plane from a plane with a dark center close to the switching point. This is justified by several aspects: The pattern had inverted colors but did not show different characteristics, the diameter of the first dark ring in the image only changed marginally in the switching zone, and the technique does not underestimate the diameter.
The line-profile reveals a xy-diameter $d_{xy} = 4\,\text{px}$ which corresponds to $d_{xy} = 0.39\,\mu\text{m}$. This suggests a diffraction limited precision of the NDD in xy-direction, because $d_{xy} \approx \lambda$.
The size of the bright part of the core region was extracted as an upper limit of the z-diameter of the presumably ellipsoidal plasma [14]. It was found to be $d_z = 6\,\text{px}$ or $d_z = 1.02\,\mu\text{m}$.

2.3.3. Variability of delivered laser intensity in the *xy*-plane

Positioning of the focal spot within the xy-plane of the specimen is achieved via the deflection of the laser beam off the optical axis by galvanometric mirrors. A drawback of this technique is, that tilting of the beam leads to slight truncations of the beam by the back focal plane aperture of the objective (see section 2.2). This leads to variations in the energy that is delivered into the sample. For a reliable performance throughout the xy-plane it is important to evaluate these deviations and to correct for them via live adjustment of the AOM if necessary.
Deviations in the delivered energy can readily be inferred from an evaluation of the plasma-threshold in conventional glass cover slips. For this purpose single laser pulses are focused into the glass. Below the plasma threshold no visible effect is achieved. At the threshold and above the refractive index in the plasma volume is changed, which can be seen in bright field mode. Thus, if the laser power needs to be changed between two xy-positions in order to stay at the plasma-threshold, the deposited energy must have changed.
The variations in deposited energy ($\triangle$) are small in the characterized area of 70 µm x 80 µm around the central (zero) beam position. In this area the plasma threshold energy in the sample plane varies by $\triangle_{70\times80} \leq 0.041\,\mu\text{J/pulse}$ ($\triangle_{70\times80} \leq 7.7\,\%$ of the highest threshold laser power, $\triangle_{70\times80} \leq 2.0\,\%$ of the maximum available laser power). In a 50 µm x 80 µm area slightly off the central x-axis the variation already decreases to $\triangle_{50\times80} \leq 0.014\,\mu\text{J/pulse}$ ($\triangle_{50\times80} \leq 2.8\,\%$ of the highest threshold laser power, $\triangle_{50\times80} \leq 0.7\,\%$ of the maximum available laser power) indicating a slight asymmetry. Further restriction to 30 µm x 20 µm improves the situation slightly to $\triangle_{50\times80} \leq 0.010\,\mu\text{J/pulse}$($\triangle_{30\times20} \leq 2.0\,\%$ of maximum laser power, $\triangle_{30\times20} \leq 0.5\,\%$ of the highest threshold laser power) in this area.
The goodness of the evaluated performance can only be classified after evaluation of the sensibility of cutting regimes to laser power in section 2.3.4.

2.3.4. Cutting regimes

The previous sections 2.3.2 and 2.3.3 have shown, that the NDD is capable of producing confined cuts in glass at a certain laser power. An increase in laser power led to bigger

lesions with cracks around the focal spot. This indicates that higher laser powers induced side effects. In order to assess the variability of delivered laser intensity (section 2.3.3) and to produce precise cuts in samples, information about different cutting regimes is essential. However, glass is a solid while biological samples are usually aqueous. As described earlier (section 2.1) side effects may differ for solids and liquids. Therefore, cutting regimes were tested in a biological, yet readily controllable sample: *in vitro* keratin networks. Keratin belongs to the cytoskeletal proteins and polymerizes into networks when assembly buffer is added. For visualization in the confocal microscope unit of the NDD Atto488-labeled keratin was used. Samples with 18 µM keratin networks were prepared as described in section B. The cutting laser of the NDD was focused through the 63x1.30 Oil λ-blue objective into central thin keratin bundles. The depth of the target in the network and the laser power were varied. All cuts were performed with single laser pulses. Time-lapse movies starting before the cut were taken at 20 fps (50 ms/frame). Additionally, the bright field channel was recorded with 9.9 fps in order to enhance the survey of bubble formation.

The effects of the laser pulses of different energy and in different sample depths are summarized in fig. 2.4. Three different regimes may be distinguished. Low laser pulse energies did not lead to any visible effect. Around a value of 0.9 µJ/pulse, however, precise cuts of keratin bundles were possible. A typical example is shown in fig. 2.5 A-C. The cut is usually accompanied by small movements of the cut bundle halves, indicating stress relaxation and facilitating the confirmation of a cut as opposed to bleaching without a cut. Slightly higher energies led to bubble formation and the affected volume increased drastically. In most cases, the large network lesions led to a relaxation of the network towards or away from the cut (fig. 2.5 D-G). The cutting regimes depended on the depth of the target in the sample; the deeper the target, the higher the required laser intensity for cuts or bubble formation. The experiments clearly show that with approximately 5 % - 10 % of the maximum available energy of 2.03 µJ/pulse in the sample plane ($\cong$ 0.1-0.2 µJ/pulse) the range for precise cuts in *in vitro* keratin networks is narrow. Although biological samples differ in their composition, it is very likely that the range for precise cuts is equally narrow in other sample types.

2.3.5. Summary and outlook

The size of the produced plasma as inferred from glass cuts was found to be $d_{xy} \approx 0.39$ µm in the xy-plane and $d_z \approx 1.02$ µm along the optical axis, which outperforms previously published specifications from similar setups (section 2.3.2). The plasma was sufficiently narrow to precisely cut small bundles of *in vitro* keratin networks (section 2.3.4). The window for such clean cuts in keratin networks was found to have a width of approx. 5 % - 10 % of the maximum available laser intensity ($\cong$ 0.1-0.2 µJ/pulse in the sample plane). When laser power was higher, side effects like cracks in glass and bubbles in *in vitro* keratin networks occurred. Other biological samples are expected to show a similar behavior. The threshold behavior confirms the statement of Colombelli *et al.* that the setup works in the regime of plasma-induced ablation[6] (clean cuts), while the side effects (cracks and bubbles) have to be classified as photo-disruption[7] [14]. The variability $\triangle$ of the laser intensity in the xy-plane was inferred from plasma threshold measurements (section 2.3.3). With respect to

[6] See section 2.1 for an explanation of this type of optical ablation.
[7] See footnote 6.

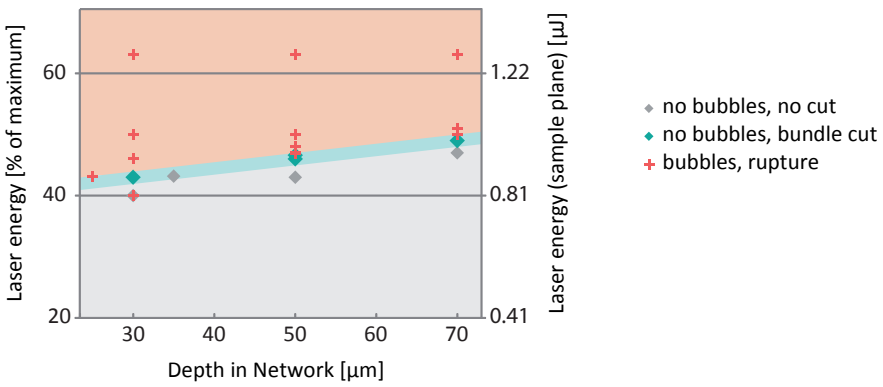

Figure 2.4.: Phase diagram of cutting regimes in *in vitro* keratin networks of 18 µM. Background colors indicate approximate cutting regimes as inferred from individual experiments (symbols): bubble formation leading to rupture (orange, crosses), precise cuts of bundles without bubble formation (green, diamonds), and no effect (gray, diamonds). For precise cuts the range for the mean laser pulse energy is narrow and depends on the depth of the cut in the sample.

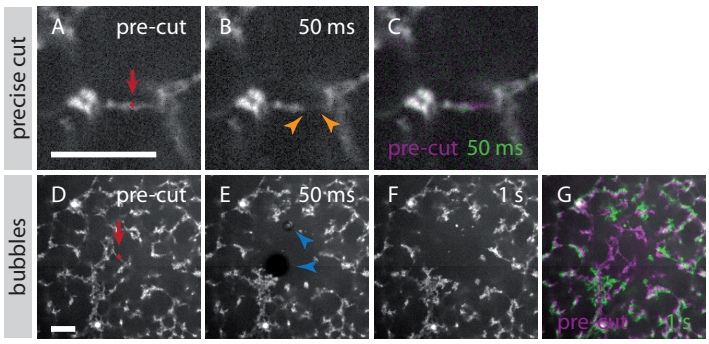

Figure 2.5.: Confocal images from time-lapse movies of optical dissection in Atto488-labeled keratin networks of 18 µM. A-C| Precise cut of keratin bundle. A| Before cut. Red arrow points at target site (red cross). B| 50 ms after cut. Orange arrow heads indicate cut bundle tips. C| Overlay of (A), magenta, and (B), green. Still structures appear white. The cut bundle slightly relaxed downwards. D-G| Cut with bubble formation. D| Before cut. Red arrow points at target site (red cross). E| 50 ms after cut bubbles are present (blue arrow heads). F| 1 s after cut bubbles have disappeared. G| Overlay of (D) and (F) reveals the size of the lesion and a relaxation process of the network away from the cut. Scale bars 10 µm.

the maximum available laser power it was found to be $\triangle_{50\times80} \leq 0.7\%$ and $\triangle_{30\times20} \leq 0.5\%$ in areas of 50 µm x 80 µm and 30 µm x 20 µm, respectively. The range for clean cuts in *in vitro* keratin networks is an order of magnitude larger than the measured variability $\triangle_{50\times80}$. Therefore, the variability of the laser intensity in the xy-plane was considered not to be the essential factor for clean cuts. A correction via software is not necessary as long as cuts are restricted to the central area of the xy-plane. All in all, the NDD has proven to produce lesions of best possible precision and sufficient homogeneity throughout the xy-plane. However, if future experiments require cuts in larger areas, a correction procedure should be implemented in the LabVIEW software, that controls the setup. Further improvements of the setup include an expansion of cutting patterns, an optional focus correction for imaging with the 561 nm laser, and the automation of imaging laser control.

3. Introduction to the *Drosophila* adult myotendinous system

Across species muscles are classified according to their function in the body, their internal structure, and their underlying functional principles. Human, and vertebrate muscles in general, are usually classified as skeletal (motion), cardiac (heart) and smooth (visceral and gut) muscles. From their structural appearance, striated and non-striated muscles are distinguished. Skeletal and cardiac muscles are striated muscles, whereas smooth muscles are non-striated because of a differing substructure. For *Drosophila*, a representative of flying insects, a comparable, yet differing classification applies. Non-striated muscle has not been found and some of its flight muscles show properties, that are unique to insects [37]. Therefore, *Drosophila* muscles are usually classified as somatic muscles, heart muscle, and visceral muscles. Except for some flight muscles most somatic muscles are comparable to vertebrate skeletal muscles. The heart muscle is a simplified cardiac system. Visceral muscles are, although structurally different, the functional counterparts of smooth muscles in vertebrates.[35]
This chapter presents structure and functionality of somatic and thus striated muscles. Although necessarily focusing on *Drosophila* muscles, it presents many fundamental principals, that are stunningly well conserved among all kinds of species [55, 77, 85]. Starting with the overall muscle pattern of *Drosophila*, the chapter works its way down to the molecular level of structure and functionality.

3.1. The adult muscle pattern

The major *Drosophila* adult somatic muscle system comprises over 150 different muscles and muscle groups in head, thorax, abdomen, and legs [47, 30], as shown in fig. 3.1 B.
The head contains small specialized muscles, which are necessary e.g. for feeding and bristle movement [31].
Wings and legs enable the fly for locomotion. Apart from the muscles in the leg the main muscles for locomotion are situated in the thorax: The jump muscle and the flight muscles [93]. According to their function flight muscles are classified into direct flight muscles (DFMs) and indirect flight muscles (IFMs). The direct attachment of the small DFMs to the wings enables control of wing orientation during flight. In contrast, IFMs, which provide the power for flight, connect to the exoskeleton. Thus, during flight IFMs move the wings indirectly by deforming the thorax. IFMs are further classified as dorso-longitudinal muscles (DLMs, muscle depressors) and dorsal-ventral muscles (DVMs, muscle elevators), which work as antagonists. [23]
Abdominal muscles show a repeated pattern in each segment (A2-A7), with slight variations in the first segment and, due to genitalia and analia, stronger variations in the terminal segments A8 and A9 [47, 18]. Abdominal muscles are assigned to three major groups, dorsal (17-22 fibers per segment), lateral (about 20 fibers per segment), and ventral (5-8 fibers

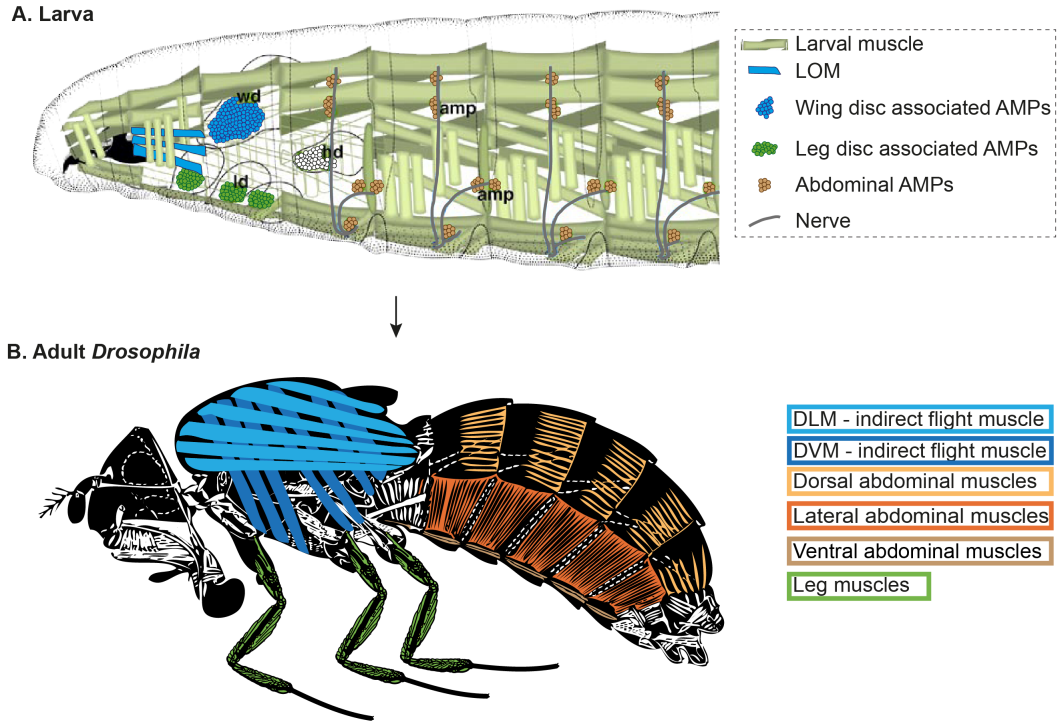

Figure 3.1.: Illustration of important parts of the *Drosophila* adult muscle pattern in thorax (blue), legs (green), and abdomen (orange) (B) and its larval origins (A) (same color code). Drawings show one hemisegment. DLMs and their precursor cells are depicted in light blue, dorsal abdominal muscles of segments A2 - A6 (counting from anterior to posterior) are shown in light orange. For clarity several small muscles, direct flight muscles and the jump muscle are omitted from the scheme. Anterior left, dorsal up. Images from [91], therein adapted from [30] (A) and [47] (B).

per segment) [47, 18]. The adult fly uses these muscles for posture maintenance, mating and ovipositioning [23].

3.2. Muscle architecture and functionality

3.2.1. Muscle architecture

Drosophila adult somatic muscles are, like their vertebrate equivalents, built from large, syncytial cells, called muscle fibers [77]. The number of muscle fibers per muscle varies among different species. Human skeletal muscle often comprises hundreds of fibers [77], whereas *Drosophila* abdominal muscles contain only one fiber per muscle. Each muscle fiber contains abundant myofibrils - highly ordered, elongated structures which are built from stacks of sarcomeres (see fig. 3.2 A, B, D). A sarcomere is the smallest contractile unit of a muscle and presents a precise pattern of actin, myosin and additional proteins, as can be seen from fig. 3.2 F. Many of these proteins are highly conserved among different species. Nevertheless, differences are observed in homologes of different species. The number of isoforms, the structure, and the actual, often diverse, tasks may vary [12, 58].

Moreover, different muscle types of one species may contain muscle specific proteins or differing isoforms of certain proteins. [84]
Two sets of thin filaments are attached in the so called Z-discs, which constitute opposing boundaries of the sarcomere, and are oriented towards the middle. Thin filaments comprise mainly actin filaments, that are decorated with the calcium sensitive troponin/tropomyosin-complex (Tn/Tm). Thin filaments overlap partially with in parallel arranged thick filaments, which are primarily built from myosin II (in *Drosophila*: myosin heavy chain, mhc) and are crosslinked in the middle of the sarcomere (M-line). Movement of thin (actin) and thick (myosin) filaments relative to each other enables contraction of the sarcomeres and thus the muscle, as described by the sliding theory (see section 3.2.2). [64, 84]
The arrangement of myofibrils and other cellular components in the myofiber depend on the muscle type. In *Drosophila* two muscle types are distinguished: The majority of somatic muscles are tubular, whereas IFMs are an exception, because they are fibrillar muscles. Both types are easily distinguishable from their morphology, which is presented in fig. 3.2. In fibrillar muscles myofibers are aligned parallel to each other but are not laterally connected. Thus, sarcomeres of adjacent myofibrils are shifted relative to each other and myofibrils dissociate easily. Nuclei are non-specifically located between myofibrils. *Drosophila* flight muscles have a high volume occupied by mitochondria, which are situated in close proximity of the fibrils [86]. Moreover, tracheal invasions throughout the fibers provide the required oxygen [53]. The size of the specialized muscle endoplasmatic reticulum, which is also called sarcoplasmic reticulum (SR) and serves as an intracellular calcium ion (Ca^{2+}) storage, is small [57, 37, 55, 58]. [64]
Tubular muscles, e.g. leg and abdominal muscles, accordingly have less mitochondria [86] and tracheal branches [53], and a larger SR [58]. Nuclei localize in the hollows of the tubularly arranged myofibrils, which are laterally connected. Sarcomeres of adjacent myofibrils are held in register and are not shifted relative to each other. [64]
Muscle control requires its connection to the nervous system, which is realized in neuromuscular junctions (NMJs). In dorsal and ventral abdominal muscle groups differing numbers of axon branches originate from a single nerve entry point and innervate each muscle fiber. In DLMs a multiterminal innervation was found. [32]
In both muscle types so called T-tubules, invaginations of the plasma membrane, penetrate the muscle fiber [53]. The plasma membrane as well as the membrane of the sarcoplasmic reticulum contain a rich diversity of ion channels and receptors [12]. These structures are involved in the triggering process of a muscle contraction (excitation-contraction coupling) [12, 13, 55].

3.2.2. Muscle functionality

Sliding filament theory & swinging cross-bridge model The sliding filament theory was independently developed in 1954 by A. Huxley & R. Niedergerke and H. Huxley & J. Hanson. It is nowadays considered to explain the working principle of muscles in general, independently of species or muscle type [55]: The contraction of serially arranged sarcomeres of myofibrils add up to a macroscopic contraction of the muscle. Sarcomere contraction is enabled by partially overlapping thin (actin) and thick (myosin) filaments which slide relative to each other during contraction and relaxation of the muscle.
On the molecular level the sliding filament theory is explained by the swinging cross-bridge model [36], which has been verified and refined extensively since its first underpinned pub-

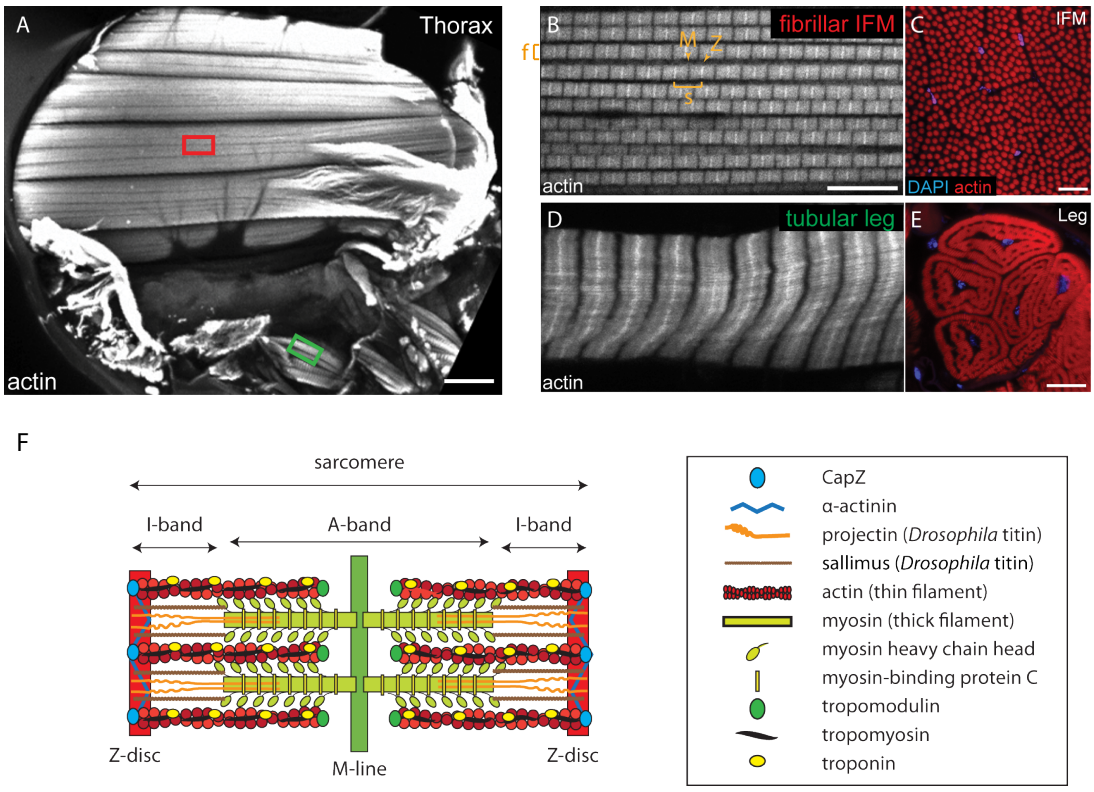

Figure 3.2.: Muscle structure of fibrillar and tubular muscles in *Drosophila* visualized by phalloidin stained actin. A| Muscles of one hemi-thorax. Boxes indicate areas in IFM (red) and leg muscle (green) shown in (B) and (D). B-C| Myofibrils of fibrillar IFMs. In the sagittal cut (B), individual fibrils (indicated with orange f) with sarcomeres (orange s) and their M-lines (orange M) and Z-discs (orange Z) are well recognizable. The cross-section (C) shows DAPI stained nuclei (blue) localized between myofibers. D-E| Tubular leg muscle with sarcomeres in laterally connected myofibrils revealed by a sagittal cut (D) and nuclei (blue) in hollows of the tube-like arranged myofibrils (E). F| Scheme of important components of a sarcomere. Images (A-E) and scheme (F) from two figures in [64]; all orange symbols/letters in (B) were added by author.

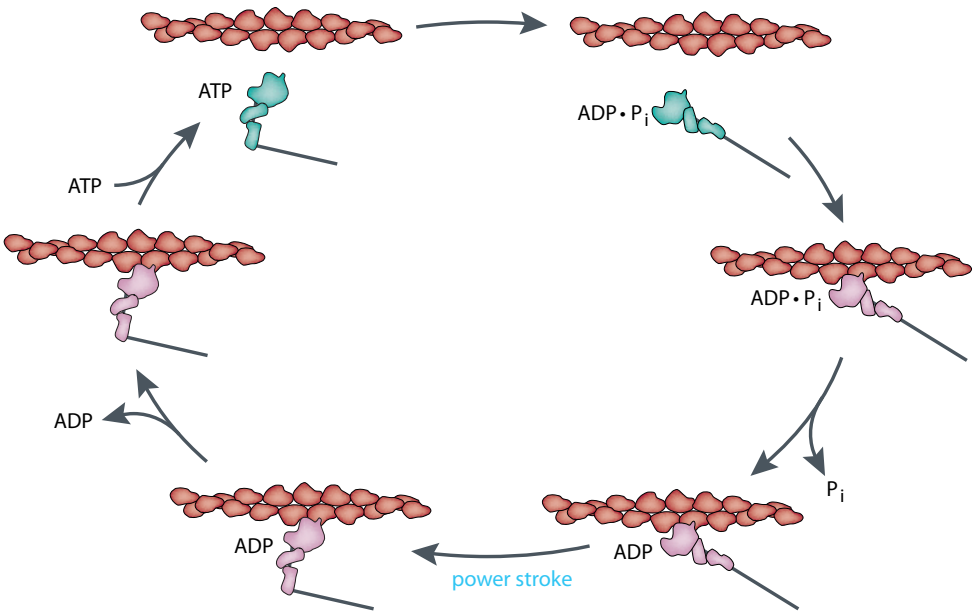

Figure 3.3.: The swinging cross-bridge model according to Spudich. Myosin II consists of a actin-binding head domain (bound state: rose, unbound state: mint green) that acts as an ATPase, and a tail domain (black line), which is tethered to the thick filament (not shown). The conformational change of the actin-bound myosin II molecule (cross-bridge) results in a power stroke (swing), that drives the movement of actin (red) relative to the thick filament. Repeated cycles of power strokes and returning to the pre-power stroke position as well as the binding and unbinding processes in between are driven by hydrolysis of ATP to ADP and a phosphate rest (P_i). From [78]; blue annotations added by author.

lication in 1969. Figure 3.3 illustrates this fundamental process. Repeated conformational changes of myosin in combination with binding and unbinding to actin (swinging cross-bridge) result in movement of actin and myosin relative to each other. This cycle is powered by hydrolysis of adenosine triphosphate (ATP) in myosin II, which is known to be an ATPase [78].

Contraction initiation In their functional principle tubular muscles, which set the majority of *Drosophila* muscles and resemble vertebrate skeletal muscle in structure and function, differ from fibrillar muscles [9, 77, 81, 85, 89].
Tubular muscles rely on individual signals from the nervous system for each and every contraction [85]. This type of excitation-contraction coupling is also called synchronous [85]. The signal of the nervous system, an action potential, travels along the axon, that innervates the required muscle. Arrival of the action potential at the neuromuscular junction (NMJ) of the axon branch induces release of neurotransmitters into the extracellular matrix between the axon and the muscle plasma membrane. Recognition of the neurotransmitters by muscle receptors initiates a depolarization of the muscle plasma membrane. This triggers an action potential in the muscle which travels along the muscle and down the T-tubules. Upon reception of the action potential voltage-gated ion channels in the membrane

of the T-tubules trigger the opening of Ca^{2+} channels in the membrane of the sarcoplasmic reticulum (SR), e.g. the ryanodine receptor Ryr (homologe to vertebrate isoforms) [12], to release Ca^{2+} from the SR into the cytoplasm, which contains the sarcomeres. Triggering of ion channels in the SR may occur via a direct connection to the voltage-gated ion-channels in the T-tubules or via an intercalated influx of calcium from the ECM that opens ion-gated SR channels [12]. Binding of calcium ions to the Troponin/Tropomyosin complex of thin filaments enables cross-bridge formation, which is inhibited at non-excitation concentrations of Ca^{2+}: The muscle contracts. After each Ca^{2+} release into the cytoplasm its concentration is regulated back to the non-excitation level. To achieve this, ATP driven Ca^{2+} pumps (e.g. Ca-P60A, a *Drosophila* homologe of vertebrate sarco-endoplasmic reticulum Ca^{2+}-ATPase [12]) transport the ions against a high gradient back into the SR. [55, 85]
Fibrillar muscles (indirect flight muscles) use a different mechanism for muscle contraction. *Drosophila* uses very high wing beat frequencies of approximately 200 Hz for flight [28]. However, the corresponding motor neurons fire at a much lower rate of only around 5 Hz [28]. Similar observations were made for indirect flight muscles of other insects [56, 85].
Instead of using the synchronous excitation-contraction coupling used in tubular muscles, IFMs are based on an asynchronous mechanism in combination with stretch-activation. Neuronal signals also result in an increased Ca^{2+} concentration in the cytoplasm. The higher Ca^{2+} level is thought to transfer muscle fibers to a stretch-activatable state and to control power output. [28, 89]
The mechanism of stretch-activation is considered to explain asynchronous flight muscles in insects [24, 38, 85, 89]. However, it is still not completely understood [24]. The fundamental muscle property that is called stretch activation, is a delay of force generation upon muscle fiber stretching. It results in increased force generation during the subsequent contraction. Complementary, a delayed force decrease upon shortening is called shortening deactivation [38, 24]. When the delay times match the frequency of the oscillating system (IFMs, the thorax, and the wings), the system generates the force necessary for flight, because force generated during shortening is higher than during lengthening [38, 85]. These properties are actually observable in all muscle types, but are especially pronounced in IFMs [24].

3.3. Adult muscle development in *Drosophila*

Drosophila development starts with a fertilized egg. The embryo develops into a larva which pupates after a few days of growth. After metamorphosis the adult fly hatches. In the course of its development to the adult animal *Drosophila* forms two sets of muscles. The first set is created during embryonic development. The development of the second set, the adult muscles, occurs during metamorphosis and is presented in the following.

3.3.1. Development of adult myotube-tendon systems in *Drosophila*

Adult muscles form in the pupa, when most of the larval cells, including most larval muscles, are histolyzed and adult muscles are formed [18].

3.3.1.1. Origin of adult muscles

Adult muscles develop from a group of special cells called adult muscle precursors (AMPs). These cells develop from the embryonic mesoderm. In the abdomen an asymmetric division of embryonic muscle progenitors creates sibling pairs, with one sibling being an embryonic cell and the other one an adult AMP. Thoracic AMP selection is believed to occur alike. [5, 18, 61, 64].
Specialized gene expression (*twist* expression) selects the AMPs to outlast the embryonic and larval stages. Instead of forming larval muscles like their embryonic equivalents AMPs proliferate and segregate to defined regions of the embryo. Abdominal AMPs are associated to nerves and form a precise pattern in each abdominal segment. This pattern already reflects the separation of the future adult abdominal muscle pattern into dorsal, lateral and ventral abdominal muscles. Thoracic AMPs accumulate in wing and leg discs, close to their future attachment sites, which show *stripe* expression [59]. The position of AMPs in the larva and their fates are shown in fig. 3.1. [5, 18, 61, 64]

3.3.1.2. Myotube formation and tendon attachment

After the selection of AMPs in the embryo, these cells develop into muscles during the pupal stage. Two fundamental principles of adult muscle formation are known. Most adult muscles, including abdominal muscles, form *de novo*, whereas dorsal-longitudinal muscles (DLMs) use larval muscles as templates for a regenerative muscle formation. [18, 25, 81]

***De novo* muscle formation in the abdomen** Figure 3.4 gives a schematic overview of *de novo* muscle development in dorsal abdominal muscles. The process is believed to also apply for other other muscles (except for DLMs). After the onset of *puparium* formation (0 h APF), the number of AMPs increases. Around 20 h APF (at 27 °C) AMPs migrate along nerve branches and fibroblast growth factor (FGF) signaling[1] (expression of dumbfounded (duf)) singles out founder cells (FCs). Each FC determines one muscle. The other AMPs become fusion competent myoblasts (FCMs). After this selection process, myotubes form by fusion of FCMs to founder cells, which elongate in anterior/posterior direction. [5, 18, 21, 22, 93]
Myotubes express β3-tubulin, elongate further and finally reach their target, the epidermal attachment sites. Attachment maturation happens first at the posterior end. This is suggested by numerous extended filopodial structures at the muscle ends, which develop into a straight end upon attachment maturation [5]. As inferred from the smoothness of the muscle ends attachment formation is considered completed at around 48 h APF [93]. Finally, the internal structure - myofibrils comprising a pattern of sarcomeres - is established (approximately until 70 h APF) [93].

Muscle formation on larval templates Regenerative muscle formation is unique to DLMs [91]. Figure 3.5 shows a schematic overview as well as confocal images of different developmental stages of DLMs. In contrast to muscle specification through FCs as in *de novo*

[1] Signaling via FGFs and their receptors is involved in many fundamental cell processes such as survival, proliferation, migration, and differentiation [82].

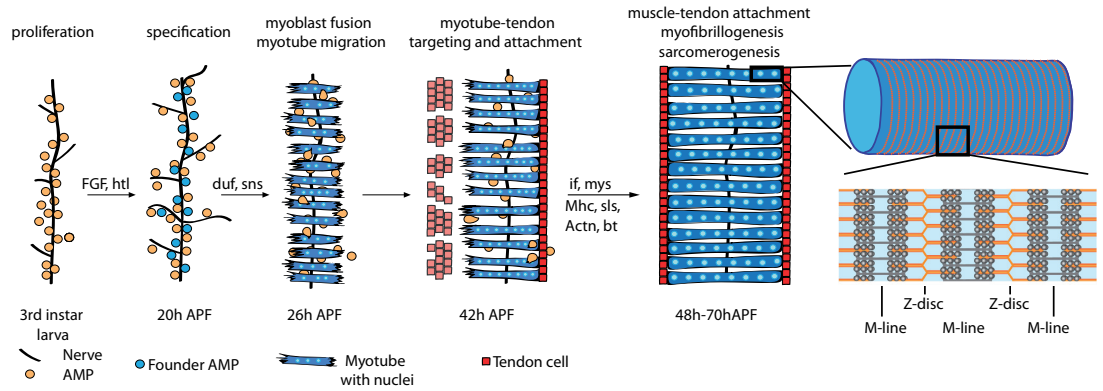

Figure 3.4.: Schematic overview of dorsal abdominal muscle development in *Drosophila melanogaster*. Abdominal muscles form *de novo* from a pool of adult muscle precursors (AMPs). Founder myoblasts are selected, all other AMPs become fusion competent and fuse to founder AMPs. Myotubes migrate to tendon cells and form stable attachments. Myofibrils and sarcomeres form. Annotations at arrows list a selection of important signals and building components for the respective developmental steps. Time applies for rearing at 27 °C. Scheme from [93].

muscle formation (presented above), three larval oblique muscles (LOM 1-3), which are excluded from histolysis, are remodelled and serve as templates for myoblast fusion [25]. However, template muscles also express duf and fusion of FCMs occurs [21], indicating parallels between the two muscle formation types. Templates split thus doubling their number [25]. Attachment to the corresponding tendon cells may be divided into three steps [92]: During migration myotube ends move towards tendon cells and form dynamic filopodia. At around 16 h APF attachment initiation occurs and myotube and tendon filopodia intercalate. Finally, attachments maturate and become stable and smooth. This is accompanied by integrin recruitment. Moreover, muscles compact and become short, while tendons elongate and become very long and thin. Notably, this is not an active muscle contraction, as it occurs in the mature muscle. After compaction the muscle elongates again and tendons shorten until the myotubes span the thorax. Concomitantly myofibrils form and develop their sarcomeric structure as will be explained in the following subsection 3.3.2. [92]

3.3.2. Development of muscle substructures: myofibrillogenesis and sarcomerogenesis

Despite a growing knowledge about proteins of the sarcomere the mechanisms leading to the formation of these highly ordered structures are still poorly understood and controversially discussed. Several models and model extensions, which emphasize different aspects of myofibrilo- and sarcomerogenesis, were reviewed and summarized in different publications [62, 17, 60, 92] and are presented in the following paragraphs. Importantly, these models differ to certain degrees but are not mutually exclusive. The models were derived from findings in several different species and muscle types. This is considered justified by the fact, that sarcomere structure is highly conserved, which in turn implies a conservation of myofibril assembly [75]. However, variations among different species or muscle types may not categorically be excluded.

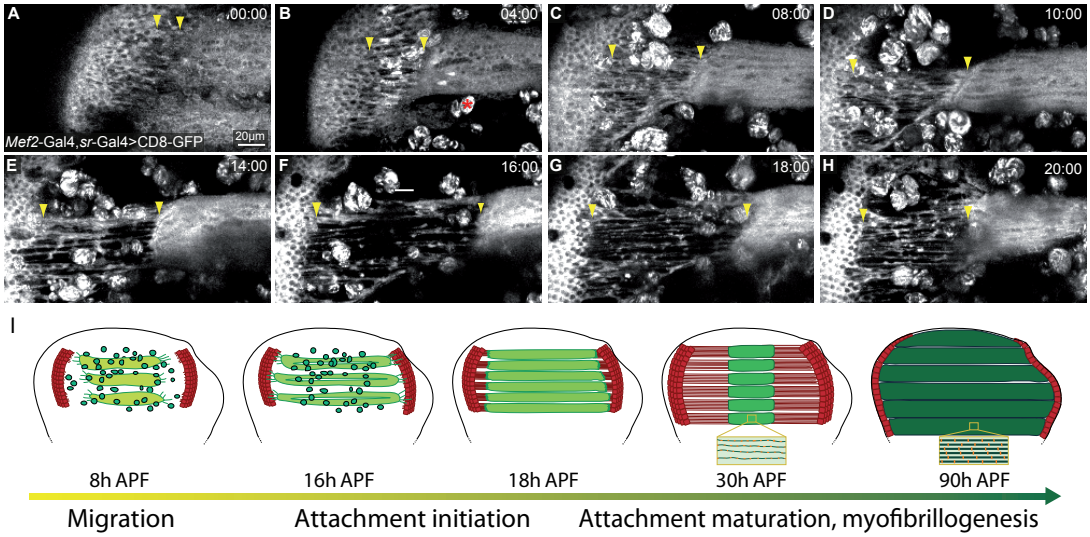

Figure 3.5.: DLM tendon development in *Drosophila*. A-H| Images from a 2-photon microscope movie of a [Mef2-Gal4, sr-Gal4 >UAS-CD8-GFP] pupa in a microscope heating chamber (27 °C). Time indicates movie time (hh:mm) and refers to start of movie during attachment initiation at approximately 16 h APF. Yellow arrowheads indicate tendon extensions, which span the gap between the tendon bodies to their left and the muscles to their right. Red asterisk marks one of several hemocites. A-B| Attachment initiation, contact. Myotubes split. C-F| Myotubes compact (shorten) while tendon extensions become very long and thin. G-H| Tendons shorten, while myotubes elongate. Images (A-H) from [91]. I| Schematic overview of DLM/tendon development. Myoblasts and DLMs are drawn in green, tendons in red. Zooms show structures of myofibrills at approx. 30 h and 90 h APF. Image (I) from [92].

The two-state model The core of this model was initially proposed by Holtzer *et al.* [34], but Rui *et al.* extended it significantly [60]. It suggests a switch from an unordered state to an ordered state. Importantly, different functional complexes such as integrin complexes, thick filaments and thin filaments, which are already pre-ordered into I-Z-I complexes[2], are independently built during the chaotic phase. Subsequently, these building blocks directly assemble into sarcomeres. Here, integrins are considered to play an important role as anchor points for I-Z-I complexes as well as transducers of tension. [60]

The extended premyofibril model Sanger *et al.* developed the so-called premyofibril model [62] which proposes a stepwise development of different structural stages: Myofibril assembly starts with the presence of premyofibrils at the edges of muscle cells. They are thought to comprise minisarcomeres. These minisarcomeres are bounded by α-actinin containing z-bodies (precursors of the Z-Band) and are composed of muscle actin, actin-binding proteins, and non-muscle myosin II. The premyofibrils develop into nascent myofibrils by addition of titin and muscle myosin II. Additionally, z-bodies align. Finally, mature myofibrils develop through a linearization of z-bodies, a loss of nonmuscle myosin II and incorporation of myosin-binding proteins into aligned A-bands. However, the mechanisms that drives the alignment of the structures in nascent myofibrils remains elusive. [62]
The premyofibril model was extended by Sparrow and Schöck. They proposed a mechanism for the assembly of premyofibrils. Integrin adhesion sites in the sarcolemma (plasma membrane) polymerize actin filaments that become crosslinked by α-actinin. The integrin complexes mature and develop into Z-bodies. The giant molecule titin (also known as sallimus or D-titin in *Drosophila*) is suspected to serve as a template for myosin incorporation and thus the interdigitation of thick and thin filaments. In the course of differentiation myofibrils are displaced from the outer regions of the muscle to the interior. However, the suggestion of a successive filling of the myotube with myofibrils from the outer to the inner regions is contradicted by findings in Drosophila DLMs, where myofibrils were observed simultaneously throughout the muscle [92]. Importantly, in the premyofibril modell contractility and tension are proposed to have a major influence on sarcomerogenesis, as will be described in more detail in the paragraph below. [75]

Tension and contractile activity in myofibrillogenesis Tension has been proven to play a fundamental role in many kinds of processes, from the cellular to the developmental level: Cell culture experiments demonstrated the force-dependent maturation of integrin adhesion sites [4], cells in the germband of *Drosophila* embryos were suggested to divide in a directed manner due to force signals [19], the cortex of *C. elegans* zygotes is under tension [45], and during dorsal closure, a process in *Drosophila* embryogenesis that is often used as a model for wound healing, the participating cells are under tension [74]. These examples demonstrate that tension is a fundamental mechanism to regulate developmental processes in the cell as well as in whole tissues.
Tension and additionally contractile activity have also been suggested to participate in myofibrillogenesis, independently of the favored model [60, 75]. Experiments in muscle cell cultures of different types revealed that contractile activity regulates myofibrillar and sarcomeric order [20, 72, 75]. The disassembly of myofibrils in cultured adult feline myocites,

[2] I-Z-I complexes: A complex of antiparallel thin filaments that are connected in a precursor of the Z-disc and thus resemble the structure of I- and Z-bands in the mature sarcomere.

which follows isolation and *ex vivo* culturing, was rescued by chemically initiating beating via the application of β-adrinergic agonists [72]. In neonatal skeletal rat myotubes, which start to spontaneously twitch after a few days in culture, chemical blocking of contractions with TTX, an inhibitor of voltage-gated Na^+ channels, resulted in reduced *de novo* assembly or disassembly of existing sarcomeric structures [20], respectively. Vice-versa, application of electrical stimuli that induced contraction caused increased assembly of sarcomeric structures [20]. Notably, it seems to be the contractile activity rather than passive tension, that causes sarcomere assembly [20]. Passive mechanical stretching resulted in an alignment of myotubes but did not have the same effects as reported for contractile activity [20].
Tension and contractile activity have also been confirmed *in vivo*. Zebrafish embryos showed a dependence of sarcomere and myofibril length on contractile activity, while fiber number, cell movement, and sarcomere formation itself did not [7]. Only recently tension has been directly investigated *in vivo* and has been shown to be essential for proper myofibrillogenesis in *Drosophila* DLMs [92]: A continuous increase of tension was observed between 13 h (myotube migration) and 22 h APF (early attachment maturation). Moreover, simultaneous myofibril assembly throughout the muscles occurred only with active Mhc motor activity, which is considered to participate in tension formation [92]. Inhomogeneous or absent force fields, created by knock downs or through optical severing of tendons, resulted in improper myofibrillogenesis [92].
These examples show, that tension and contractility play an important role during myofibrillogenesis. However, additional interpretations concerning the mode of action of muscle activity may not be dismissed. Contractile activity is known to be triggered via calcium signalling [7, 20, 55, 27]. Hence, other signalling pathways than force transduction might also be involved [7].
For the transduction of forces involved in tension and contractile activity integrins are considered to play a major role [27, 60, 75, 92]. They are suggested to not only provide anchor points for I-Z-I complexes but also to be required for tension maintenance that allows for the arrangement of thin and thick filaments [60]. Moreover, they are involved in the formation and maintenance of stable attachments between muscles and tendon cells via the extracellular matrix, which was found to be crucial for myofibrillogenesis in DLMs [92].

3.4. Summary and aim of thesis

During the recent years great progress has been made in the field of muscle architecture and functionality. Besides a growing number of genes, that have been identified and analyzed for their function in muscle development, our picture of muscle structure has been refined, also concerning differences between different muscle types and different species. However, despite several proposed models of myofibrillogenesis our understanding of the processes that drive the transition of a myotube from a disordered to an ordered state is still poor.
Tension and contractile activity are promising fundamental mechanisms that are currently expected to contribute to structure formation. Tension in *Drosophila* DLMs was investigated until the early stages of attachment maturation almost three days before eclosion [92]. It is unclear, whether tension remains permanently after its initial evolution or if it is a transient factor. Moreover, the molecular contributors are still to be identified and con-

firmed. Observations made by Weitkunat *et al.* [92] were restricted to dorsal-longitudinal flight muscles (DLMs), which are structurally and functionally different from most other *Drosophila* muscles and also from vertebrate skeletal muscle [66]. Hence, it is unclear whether tension is universally necessary for muscle formation or if it is unique to DLM (fibrillar muscle) development. Finally, the role of contractile activity as opposed to passive tension remains to be investigated in live *Drosophila* muscle development.
It is therefore indispensable to gain further insights into these mechanisms in order to extend our understanding of muscle development. Open questions and interesting aspects that were addressed in the course of this thesis are:

- How does tension change during dorsal-longitudinal flight muscle development?
- Which molecules contribute to tension formation in DLMs and tendons?
- Is tension a universal cue in muscle development or unique to DLMs and thus fibrillar muscles?
- The role of contractile activity as opposed to passive tension.
- Which structural stages coincide with which functional stages?
- Cause and effect in the interplay of structure and functionality in developmental processes.

4. Experiments and results

This chapter covers the experiments which were performed in order to address the open questions that were summarized in section 3.4. Experiments were carried out in two structurally and functionally different types of *Drosophila* muscles, dorsal abdominal muscles and dorsal-longitudinal (indirect) flight muscles (DLMs). DLMs were chosen because Weitkunat *et al.* showed that tension plays an essential role in the development of the DLM myotendinous system [92]. However, many open questions remained, inspiring further investigations:
The nanodissection technique was used to extend the knowledge of tension in DLMs (section 4.1). Specifically, experiments were performed on DLM tendons and microtubules in order to investigate their role in tension formation. The myosin II inhibitor blebbistatin was used on DLMs in order to shed light on the contribution of myosin to tension formation.
For several reasons a second set of muscles, the dorsal abdominal muscles, was chosen for experiments. First, abdominal muscles are different from DLMs regarding structure, working principle, and development (see chapter 3). Hence, it will be possible to compare findings from fibrillar DLMs with another type of muscles, the tubular abdominal muscles. Second, knowledge of this group of muscles is poor and further investigations of structure and functionality are necessary for a better understanding. Finally, dorsal abdominal muscles are close to the surface of the pupa throughout the time APF of interest, thus facilitating experimental procedures. Section 4.2 shows the response of abdominal muscles to nanodissection, including attachment (section 4.2.2) and Ca^{2+} (section 4.2.3) behavior. Their structure is elucidated in section 4.2.4, before a summary closes the chapter.

4.1. Nanodissection in the myotendinous system of dorsal-longitudinal muscles

Recently, Weitkunat *et al.* have shown that tension plays an important role during DLM development [92]. Optical severing experiments revealed that visco-elastic tissue properties of these indirect flight muscles and/or their surroundings change over time [92]. However, the latest investigated time point was during early attachment maturation at 22 h APF. Hence it is unclear, whether tension is present at later time points. To clarify this, the nanodissection device (NDD) was used to perform optical severing experiments on tendons of DLMs during muscle compaction at 30 h APF. Moreover, what remains to be determined is the nature and the location of the structures that carry the load, and more specifically which sub-cellular components contribute to tension formation. Tension may be created in muscles, tendons, the surrounding tissue, or a combination of the three. Therefore, microtubules in muscles and myosin II were investigated for the nature of their role, if any, in the visco-elastic behavior of the DLM myotendinous system.

4.1.1. Optical severing of DLM tendons

4.1.1.1. Experimental procedures & analysis

Experimental procedure Living pupae of [UAS-Gma-GFP x sr-GAL4/TM6(Tb) (♂ x ☿ & ☿ x ♂)][1] (actin labeled in tendons only) were aged to 30 h APF at 27 °C and prepared for imaging and optical severing as described in section A.3. Images were acquired at the high rate of 12.5 fps (80 ms/frame), starting approximately 1 s before cutting takes place. All cuts were performed with the same cutting settings. The laser was set to an average energy of 0.76±0.01 µJ/pulse (37,6 % of maximum), which corresponds to a peak power of 2.04±0.04 kW. As DLM tendons at 30 h APF are very long and thin due to the compaction process of the muscles (fig. 4.1 A), it was sufficient to perform optical severing with point cuts (10 pulses/point, 1000 Hz) to achieve complete and clean rupture of the target tendon. This is advantageous because the z-level doesn't have to be changed during the cut and the rupture of the target happens fast. Both aspects improve data quality as compared to longer and thicker cuts, which already experience partial relaxation during the ongoing cutting process.

Qualitative analysis Optical severing of DLM tendons aims at the verification of tension in this myotendinous system. For a qualitative confirmation of tension a qualitative analysis of the tendon response is sufficient. Several regions of the severed tendons were observed in order to unambiguously verify tension. The most prominent indicator for tension release is the retraction of the cut edges (referred to as tendon tips) away from the cut. However, this observation is not sufficient because other mechanisms than tension, specifically depolymerization at the cut edges and active contraction, could also cause a retraction of the cut edges away from the cut. Therefore, retraction movement was also evaluated for prominent structures along the tendons. Depolymerization can be excluded, when both regions (tendon tips and structures along the tendon) show a retraction movement. The observation of tendon ends (not cut edges) is not of interest because due to geometrical reasons they are often out of focus or surrounded by structures of other tendons, which impedes a proper identification of the relevant structures. Active contraction of the tendons is excluded because such a behavior has not been found to play a role for tendons.

Quantitative analysis In order to compare results of tendon severing at 30 h APF to previous results by Weitkunat *et al.* [92], it is necessary to extract values of that observable that was established in their publication [92]: the mean value of all individual recoil velocities of ruptured tendons in several equally aged pupae. From each cut they extracted single recoil velocities of individual tendons with a PIV algorithm[2]. The individual recoil velocity was defined as the mean velocity of several templates in two specified areas, which were located on opposite sides of the cut and contained one target tendon half each [92].

[1] A detailed description of all genotypes is given in appendix A.1.

[2] Particle Image Velocimetry. Working principle: The analysis aims to compare pairs of images to extract the movement of structures. To do so the first image is divided into squares called templates. For each template the algorithm searches the most likely new position in the second image by using the cross correlation technique. Comparison of template positions in both images reveals a vector field of movement from the first to the second image.

In order to extract the mean recoil velocity as defined by Weitkunat *et al.* the same MATLAB (MathWorks) based PIV analysis as performed in [92] was used, but results were not reliable. PIV algorithms only work, if structures are distinguishable on the scale of the template size. However, it is problematic, when there are only structures that resemble each other or themselves on this scale, which is the case for tendons at 30 h APF. At this time point, the structure is composed of self-resembling white, long and thin lines on a black background (see fig. 4.1). In order to improve the reliability of the algorithm, it was restricted to analyze manually selected, confined areas around the tendons. However, this did not improve the results sufficiently. Also a second PIV approach, based on stepwise refinement of templates (PIVlab 1.32 [80]), did not produce reliable results. Hence, extraction of the recoil velocity as defined in [92] was not possible.
Instead, a second, semi-automatic analysis approach was tested in order to extract tip velocities of the cut edges of severed tendons. Here, the experimentally obtained gray scale movies were manually converted to binary movies. Frayed structures and noise were manually smoothed (both in Fiji/ImageJ). Afterwords, a MATLAB algorithm [90] was used to find the skeleton of the target tendon in each frame and custom written code was used to extract and compare tip velocities. However, the results were not satisfactory, as revealed by comparison to manual evaluation of random samples. Binarization of the gray scale image and skeletonization of the tendon structure were not reliable enough. This becomes plausible when considering the relatively small movements of the tendon tips together with the following aspects: To binarize a gray scale image, a threshold has to be used, such that only structures with gray values above this threshold remain in the binarized picture. However, even slight z-drifts of the thin loose tendons lead to a significant decrease in their intensity value. Thus, structures, which are too far out of focus, do not appear in the binary image. This creates a false tendon tip position. Although this is a general problem in movies of a single confocal z-slice, it becomes more pronounced when an image is binarized. A second reason is the occurrence of position jumps due to changes in tip shape. Skeletons in pointed tips start closer to the edge than skeletons in broad tips.

As neither the automated nor the semi-automated approach worked properly, tip velocities of severed tendons were extracted manually. Two quantities were distinguished, *absolute velocity* (v_{abs}) and *parallel velocity* ($v_{||}$). v_{abs} describes the norm of the tip velocity calculated from its movement in the xy-plane from one frame to another, divided by the corresponding time. $v_{||}$ is the tip velocity component along the long tendon axis. The velocity component vertical to the long tendon axis is not taken into account. Instead of taking the norm, information about the direction of the movement is preserved. A positive value refers to a movement away from the cut, whereas a negative value indicates a movement towards the cutting site.
Tip velocities of 27 tendon halves from 15 optical severing experiments were manually measured. To do so, a prominent structural feature at the tendon tip was tracked in as many frames as possible. During the initial part of the movies tracking was usually possible in all frames. Later on, however, the movement was so small that tracking in consecutive frames was not possible anymore. Instead, the movement over several frames had to be taken into account in order to get one data point (assigned to the first of the averaged frames). Each tendon tip velocity was independently evaluated three times (three evaluation rounds). In cases where results of the three independent evaluation rounds of one and the same tendon tip differed to much, the according tip was removed from analysis (3/27 cases).

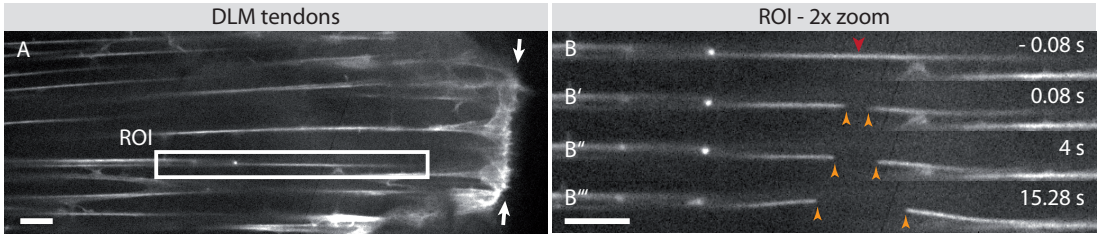

Figure 4.1.: DLM tendon tip relaxation after optical severing in [UAS-Gma-GFP x sr-GAL4/TM6(Tb)] at 30 h APF , i.e. during attachment maturation and muscle compaction (NDD SD confocal images). A| Part of the DLM tendon field region. Arrows indicate line of attachment to posteriorly located muscle (not labeled). Tendons are well elongated and very thin. The box indicates the region of interest (ROI) shown as 2x zoom in (B). B| Zooms show time points (B-B"') from a movie of an optically severed tendon. Red arrowhead indicates position of cut. Cut tendon tips (orange arrowheads) retract and tendon halves bend upon cutting. Time indications refer to frame of cut (0 s). Scale bars 10 µm, anterior left, dorsal up.

4.1.1.2. Results: Response of DLM tendons to optical severing

Qualitative response A typical example of an optically severed tendon is shown in fig. 4.1. The edges of optically cut tendons (tendon tips) moved away from the cut. The direction of movement was mainly parallel to the long axis of the tendon, but bending and a superimposed fluctuating movement of the tip were also observed. The movement of tendon tips in combination with the overall movement of the cut tendon pieces (structures along the tendon) verifies that for DLM tendons at 30 h indeed predominantly a relaxation process was observed.

Quantification of the retraction process Results of manual data evaluation of the mean *absolute* and mean *parallel velocity* of DLM tendon tips at 30 h APF are shown in fig. 4.2 A and B, respectively. Analysis of the data revealed several interesting aspects. The initial mean values of *absolute* and *parallel velocity* (earliest data point) were $v_{\text{abs}}(0) = 173 \pm 125\,\mu\text{m/min}$ and $v_{||}(0) = 138 \pm 112\,\mu\text{m/min}$ (errors are standard deviation). Starting from these values, mean velocities decreased over time. The values of $v_{\text{abs}}(0)$ and $v_{||}(0)$ differed only by approximately 20 %, which confirmed the qualitative observation that cut tendon tips mainly moved along the long axis of the tendon. Consistently, the velocity decreases with time after the cut. These observations demonstrate that tension is also present in the myotendinous system of DLMs at 30 h APF. However, standard deviations are large. This reflects the diversity in responses of individual tendon tips.

4.1.2. Optical severing of microtubules in DLMs

Experimental procedures Although it has been shown by Weitkunat *et al.* and work in this thesis (see section 4.1.1) that tension is important for correct development of the

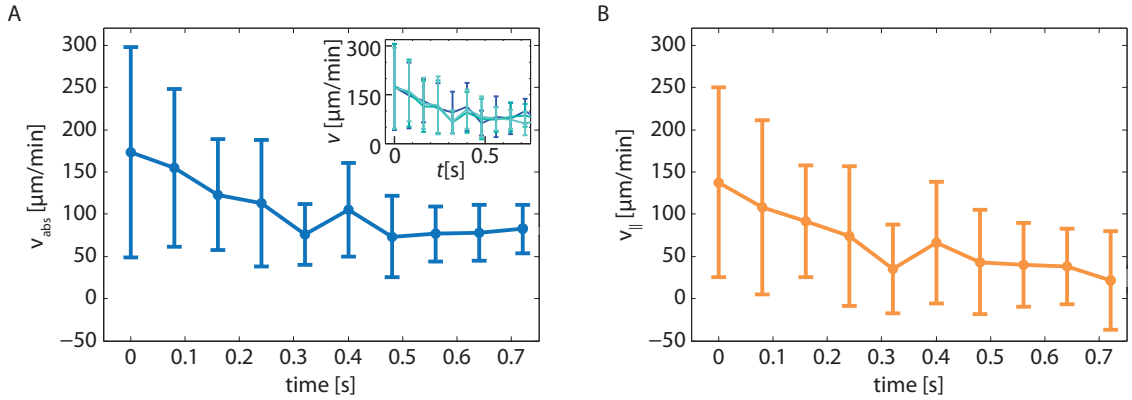

Figure 4.2.: DLM tendon tip velocities after optical severing at 30 h APF calculated from the manually evaluated movement of 24 individual tendon tips. Values are mean velocities of all tendon tips. Error bars are the standard deviation of individual tip velocities. A| v_{abs}, mean of all rounds. Inset: Mean $v_{\text{abs}}(0)$ of all tendon tips in three evaluation rounds (indicated by different colors) reveal the reliability of manual tracking. B| $v_{||}$, mean of all evaluation rounds. For a definition of v_{abs} as opposed to $v_{||}$ see text.

myotendinous system of the DLMs, it is not yet clear, which molecules in which cells contribute to tension formation or carry the load. The cytoskeleton is a likely candidate for stability maintenance. Nevertheless, it is not clear, which of the cytoskeletal key players, specifically actin, microtubules and intermediate filaments, do contribute. It may well be that only part of the cytoskeleton maintains stability, while other structures exist in parallel without being exposed to stress.
In order to investigate the role of muscle microtubules, progeny of [Mef2-GAL4] crossed to [UAS-α-tubulin-GFP] was used. An alternative approach with homozygous [β-tubulin 60D-GFP] was not successful because of its low contrast in spinning disc confocal images. Pupae were aged to 18 h or 24 h APF at 27 °C, prepared for live imaging and optical severing on the NDD as described in section A.3, and imaged during the subsequent hour. Two developmental time points were selected because tension in the DLM-tendon system was shown to evolve over time [92]. This behavior is expected to be reflected in the response of those cytoskeletal structures that transduce tension (here: microtubules). Movies were taken at frame rates of 6.25 fps (160 ms/frame) or 3.33 fps (300 ms/frame), depending on the brightness of the sample. The movies started approximately 2 s before optical severing. Single laser pulses in the range of 0.81 µJ/pulse to 0.93 µJ/pulse (2.17 kW to 2.50 kW peak power, 40 % to 46 % of maximum power) were used to precisely sever microtubule bundles.

Qualitative analysis Figure 4.3 shows a typical result. Optical severing caused small lesions, which led to a slow retraction of cut edges away from the cut. This can be seen in

image sequences as well as in a kymograph[3]. Here, the cut edges appear as curved lines, which indicate a retraction away from the cut. The high density of microtubule bundles in the muscles impeded the evaluation of prominent structures along the severed bundle. Moreover, it was unclear, whether a lesion caused a partial or a complete rupture of the target bundle. The direction of movement was mainly along the long axis of the bundles. Apart from the intended cut of the microtubule bundle, target muscles did not show any visible integrity defects.

Quantitative analysis Image analysis was done manually. Analysis of the bundle response was restricted to the bundle tips because due to the high density of microtubule bundles, structures along the microtubule bundles could not be observed. In total, six cuts in six different pupae were manually analyzed. Movement of each trackable microtubule bundle half (2 anterior and 6 posterior halves) was estimated by comparing the position of the cut edge in different frames. Time steps between two analyzed frames, which showed ongoing movement of the edges, varied depending on how much cut edges moved: The more they moved, the shorter the time periods. Time periods ranged from 0.6 s to 5.6 s.
The results of the quantitative analysis are presented fig. 4.4. Absolute velocities were found to have values between 5 µm/min and 64 µm/min. These retraction velocities are in the range of microtubule depolymerization, which is reported to occur at velocities of 10-50 µm/min [10, 69, 88]. This indicates that depolymerization is the driving mechanism behind the movement of cut microtubule halves. As the high density of microtubule bundles in the muscles impede an observation of prominent structures along the severed bundle, the contribution of an elastic response (relaxation) can neither be excluded nor verified. Hence, it is not possible to assign the observed retraction velocities exclusively to one of the possible causes: tension, depolymerization, active transport, or a combination of the three.

4.1.3. Inhibition of myosin II with blebbistatin

Myosin II is an obvious candidate for tension creation. It is a motor protein and capable of producing force, as can be directly seen for instance in motility assays [63]. Moreover, myosin heavy chain (mhc) is present in *Drosophila* sarcomeres and hence involved in muscle contraction, thus showing its capability to create tension. In addition, theoretical calculations proposed myosin in its function as a motor protein to be essential for the formation of sarcomeric patterns in acto-myosin networks [94]. Therefore it is necessary to investigate the role of myosin II in order to understand tension formation and its contribution to development in DLMs.

[3]Here, a kymograph is a space-time-plot that is used to explore the movement of a structure of interest in a certain direction. To do so it shows the temporal evolution of a line (along the direction of interest) across the structure of interest (usually in the course of a movie with frames that are equally distributed in time). A line in the kymograph that is not parallel to the time-axis represents a moving object, while a line that is parallel to the time axis represents a still structure. Example: A white dot (2 px × 2 px) moves from the left side straight to the right side of an otherwise black 20 px × 20 px image within ten frames of a movie. In order to show the movement of the dot the kymograph of a horizontal line through the dot spanning the whole image is required. The kymograph will be 20 px wide to represent space (along the line) and 10 px high to represent time (1 px for each frame). The movement of the dot along the drawn line is translated into a diagonal white line in the kymograph.

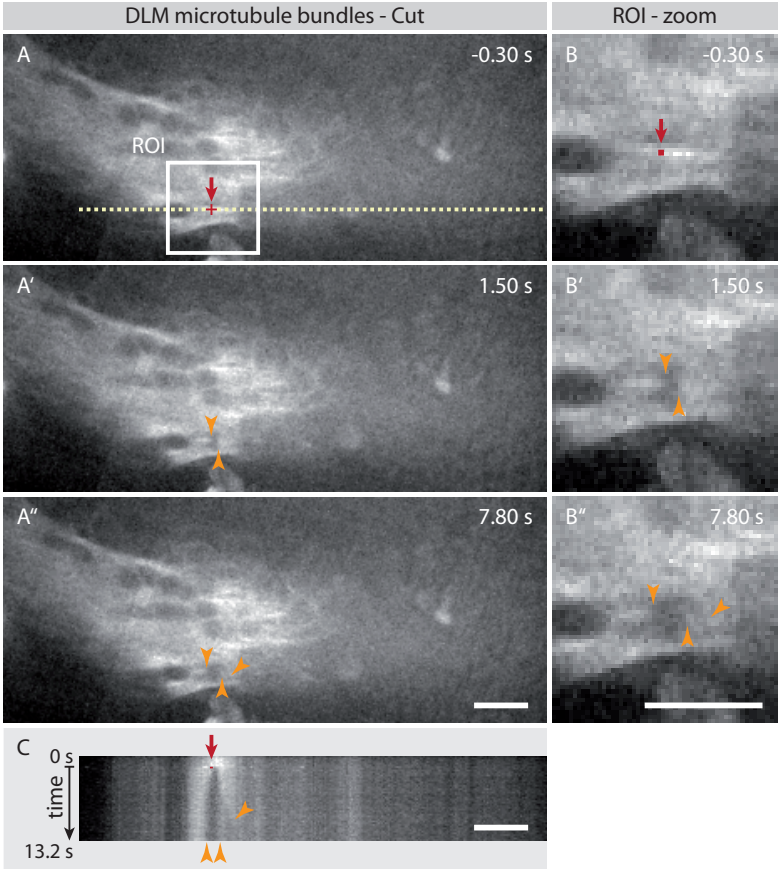

Figure 4.3.: Retraction of microtubule bundles in DLMs after optical severing. Microtubules in DLMs were genetically labeled via α-tubulin-GFP and imaged with the NDD confocal unit. Scale bars 10 µm. Anterior left, dorsal up. A-A"| Image sequence from a movie of microtubule severing in a DLM (18 h APF). B-B"| Magnification of ROI indicated by white box in (A). C| Kymograph of dashed yellow line in (A). Red arrows point towards target site (red dot or cross). Orange arrow heads indicate retracting cut edges.

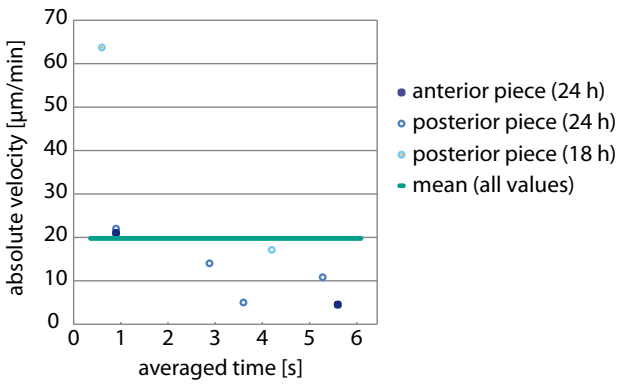

Figure 4.4.: Manually evaluated *absolute retraction velocities* of microtubule bundles in DLMs after optical severing. Abscissa shows averaged period of time for respective velocity evaluation (see text for details).

One way to investigate, whether myosin II contributes to tension formation, is to change myosin activity and test for changes in tension as compared to muscles with normal myosin II activity. Unfortunately, the omnipresence of myosin II leads to early lethality of mhc knock down flies, thus impeding easy genetic access to mhc function. Therefore, an alternative approach to influence myosin II functionality was developed and tested. It is based on the application of the chemical (-)-blebbistatin, which is known to inhibit class II myosin activity in certain vertebrate and *Drosophila* cells [42, 79, 16].

4.1.3.1. Experimental procedure: a new protocol for the application of inhibitory agents

Characteristics of blebbistatin Application of blebbistatin to biological samples requires the consideration of several specific aspects.
The capability of blebbistatin to inhibit myosin II activity is essential for the experiment. This capability is destroyed by blue light [40]. As a consequence blebbistatin needs to be protected from artificial and natural light. Therefore, all preparation work involving this chemical was performed in a dark room with red light.
Blebbistatin is barely soluble in water but has to be dissolved in a suitable solvent [70]. This solution may then be added to water. Here, blebbistatin was dissolved in dimethylsulfoxide (DMSO) because blebbistatin/DMSO-solutions have been shown to work properly on actomyosin networks [67]. The solutions applied to pupae thus also contained DMSO. DMSO is, although widely used for freezing cells, toxic to cells when applied for too long. This implies that DMSO (and consequently blebbistatin) concentration should be kept as small as possible. Care needs to be taken to ensure that observed effects are due to blebbistatin and not to DMSO. DMSO was not replaced by a different solvent, because alternative solvents such as methanol are also toxic.

DMSO is hygroscopic [71]. If blebbistatin in DMSO without any water was added to pupae, this led to a dipping of the pupae bodies, indicating that water had been extracted. This did not happen, when water had been added to the solution. Consequently, blebbistatin/DMSO solutions were not added to glycerol and mounted conventionally. Instead, agents were diluted in ddH_2O to reduce the hygroscopic effect as much as possible. Due to evaporation a constant presence of aqueous agent solution was not guaranteed with conventional mounting technique (glycerol replaced by agent solution). Therefore, a new protocol for the application of aqueous solutions was developed and tested.

Mounting technique for the application of inhibitory agents Properly aged pupae are prepared for chemical application by removing the appropriate part of the shell, which is covering the region of interest (ROI) in the pupa. This is done in the same way as for conventional imaging (see section A.3). The subsequent procedure of mounting and chemical application is illustrated in fig. 4.5. The pupa is mounted on the same type of custom made object holders with a furrow for the pupa that was also used for conventional mounting. Silicone grease separates a part of the furrow from the surrounding (fig. 4.5 A). The pupa is positioned right at the edge of the holder in such a way, that the antennae of the pupa shell loom over the edge of the holder. A small portion of silicone grease is used to hold the pupa in position during subsequent application of chemicals (fig. 4.5 B). The silicone grease creates a small chamber around the pupae when a cover slip is added on top (fig. 4.5 C). Before positioning the cover slip, the desired volume of chemical solution is applied. Here, a volume of 2 µl was used; one half was applied directly onto the pupa, the other half onto the cover slip. The cover slip is positioned right over the ROI, thus fusing both drops. The pupa is then completely covered by the applied solution, except for the antennae, which guarantees oxygen supply. The large amount of solution in combination with a minimized evaporation (reduced surface due to the silicone grease) helps to ensure that the applied solution constantly covers the ROI.

General application protocol Pupae were aged to 18 h APF at 27 °C as described in section A.3. After mounting (new mounting technique described above), samples were placed in humidity chambers. These chambers were boxes, which contained wet tissue to further reduce evaporation of the chemical solution. Additionally, the boxes were wrapped in two layers of aluminum foil to reduce evaporation and to protect the samples from light. Due to the light sensitivity of blebbistatin all preparation work involving this chemical was performed in a dark room with red light. Humidity chambers with samples (protected against light) were placed in the temperature chamber for incubation at 27 °C. After incubation pupae were removed from the incubation sample holder and mounted for imaging on a new sample holder in the conventional way (see section A.3).

Control of mounting technique: ddH_2O The newly developed chemical application procedure described above was tested by fluorescent imaging of living pupae of [♀ y, w, UAS-CD8-GFP; y, w, UAS-CD8-GFP x ♂ y, w, UAS-CD8-GFP; Mef2-GAL4, sr-GAL4/TM3(Ser)]: $n = 7$ pupae were mounted in 2 µl of ddH_2O according to the new mounting protocol and general application protocol. After an incubation time of 4 h DLMs and their tendons were imaged and examined for visually noticeable defects.

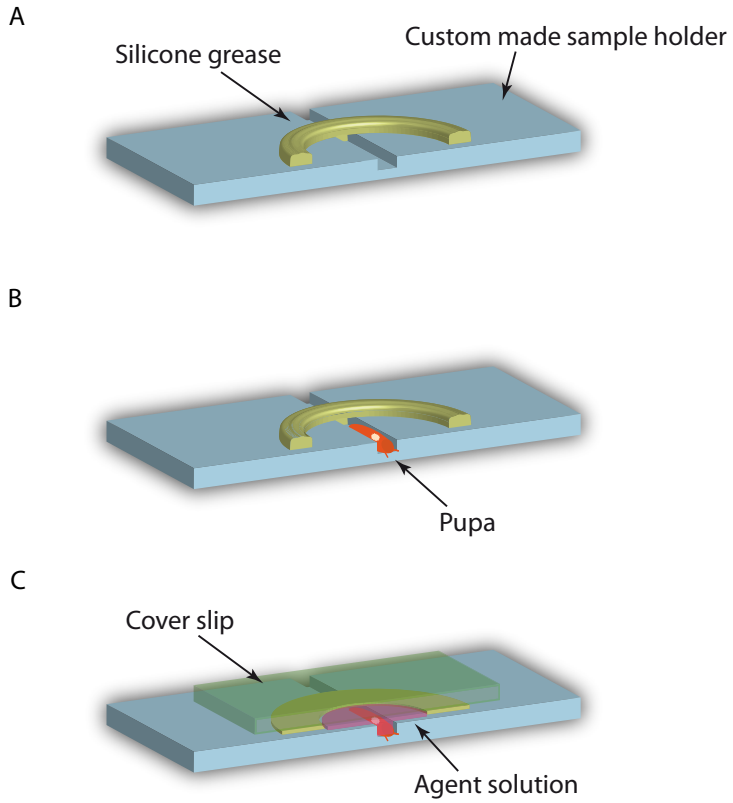

Figure 4.5.: Mounting technique for the application of aqueous agent solutions to pupae. A| Silicone grease separates a chamber for the pupa in the xy-plane of a conventional custom made sample holder. B| Pupa (orange) is placed in furrow with antennae looming over the edge. The opening in the shell, the ROI (beige), is facing upwards. C| Agent solution is added and a glass cover slip is pressed onto the vacuum grease until it is right above the pupa.

Blebbistatin (in DMSO) and DMSO experiments With respect to future optical severing experiments in the blebbistatin inhibited system, it is desirable to find out in advance, which blebbistatin concentrations do have an effect in DLMs. Ideally, a blebbistatin effect would be visually noticeable, e.g. in reduced muscle compaction or structural differences as compared to normal development. This would drastically improve the reliability of optical severing data because it would ensure that optical severing is indeed performed in inhibited systems only.
(-)- Blebbistatin (Sigma-Aldrich) in DMSO (5 mg/ml) and ddH_2O was applied to pupae at 18 h APF in two different concentrations, 0.9 mM or 0.5 mM, in order to find the minimally necessary concentration for defect induction. Two different incubation times were tested:

- 4 h of incubation directly followed by imaging at approximately 22:10 h - 23:00 h APF (4 h incubation → exchange agent with glycerol → $\text{imaging}_{22\,\text{h}}$)

- 1/2 h incubation time with directly following imaging (at approximately 19 h APF) and a second round of imaging at approximately 22 h APF; pupae were at 27 °C in between imaging (1/2 h incubation → exchange agent with glycerol → $\text{imaging}_{19\,\text{h}}$ → 27 °C → $\text{imaging}_{22\,\text{h}}$)

For control experiments pupae were incubated in solutions of DMSO in ddH_2O. The incubation protocol was identical to experiments with blebbistatin, except that white light was used at all times. Concentrations of DMSO solutions were equal to DMSO concentrations in experiments with blebbistatin. Table 4.1 gives an overview of agents, concentrations and incubation times.
All experiments with 4 h incubation time were performed with pupae of [♀ y,w, UAS-CD8-GFP; y,w, UAS-CD8-GFP x ♂ y,w, UAS-CD8-GFP; Mef2-GAL4, sr-GAL4/TM3(Ser)] and were fluorescently imaged with 488 nm. Experiments with 1/2 h incubation time were performed in pupae of [UAS-palmitoylated-Cherry; Mef2-GAL4, sr-GAL4/TM3], which were illuminated for fluorescence microscopy with 561 nm. This switch in genotypes for the second protocol was necessary because the second protocol included two imaging phases. The first imaging phase would have destroyed the blebbistatin, if 488 nm illumination had been used.

4.1.3.2. Results

A summary of the results is given in table 4.1.

Control of Mounting Technique All pupae in control experiments with ddH_2O showed normal DLM and tendon morphology at the time of imaging at approximately 22 h to 23 h APF, thus verifying that the newly developed protocol does not visibly influence the development of DLMs or their tendons until 23 h APF. This is well seen from a comparison of typical pupa of a ddH_2O control experiment with a conventionally mounted pupa of the same age as shown in fig. 4.6. In both cases, tendons are well elongated and thin, indicating proper muscle compaction. Additionally, movement of GFP-accumulations (small dots) was observed, which demonstrates a functional transport machinery.

4 h incubation → exchange agent with glycerol → imaging$_{22\,h}$				
Experiment #	$c_{Blebbistatin}$	c_{DMSO}	c_{ddH_2O}	defects/total
Control	0	0	55.4 M	0/7
C	0.9 mM	0.74 M	52.5 M	2/3
D	0	0.74 M	52.5 M	3/5
E	0.5 mM	0.45 M	53.6 M	2/7
F	0	0.45 M	53.6 M	2/4

1/2 h incubation → exchange agent with glycerol → imaging$_{19\,h}$ → 27 °C → imaging$_{22\,h}$				
Experiment #	$c_{Blebbistatin}$	c_{DMSO}	c_{ddH_2O}	defects/total
G (imaging$_{19\,h}$)	0.5 mM	0.45 M	53.6 M	1/5
G (imaging$_{22\,h}$)	$\leq$ 0.5 mM	$\leq$ 0.45 M	$\leq$ 53.6 M	1/5

Table 4.1.: Concentrations (c) of agents (blebbistatin, DMSO, and ddH_2O), incubation times, time points of imaging, summary of protocol in blebbistatin experiments, and results (number of pupae with defect/total number of pupae in this experiment).

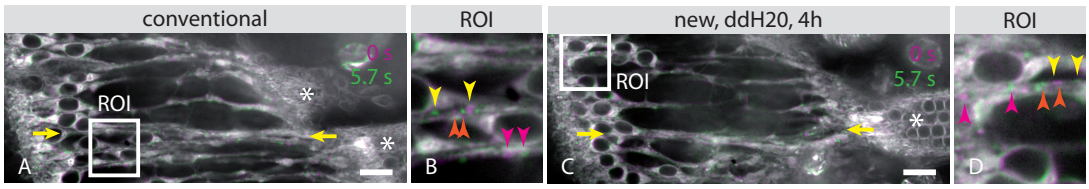

Figure 4.6.: Details of the myotendinous system of DLMs (asterisks) in pupae of [♀ y,w, UAS-CD8-GFP; y,w, UAS-CD8-GFP x ♂ y,w, UAS-CD8-GFP; Mef2-GAL4, sr-GAL4/TM3(Ser)] as observed with SD confocal fluorescence microscopy. Images are overlays of two time points (1: magenta, 2: green, still structures appear white) separated by $\Delta t = 5.7$ s. A| Pupa during muscle compaction conventionally mounted in glycerol at 22 h APF. C| Pupa mounted in ddH_2O at 18 h APF according to new protocol and imaged after re-mounting at 22 h APF. Tendons are well elongated in both cases (ends of examples marked with yellow arrows). B,D| Zooms of boxes in A (B), and C (D). Arrow heads of the same color point at the same GFP accumulation (bright small dots) at the two time points that were overlayed. GFP accumulations move rapidly along tendons. No white (=non-moving) dots are visible. Scale bars 10µm. Anterior left, dorsal up.

Blebbistatin and DMSO Pupae which had been incubated in 0.9 mM ($n = 3$ pupae) or 0.5 mM ($n = 7$ pupae) blebbistatin solutions (in DMSO and ddH_2O) for 4 h showed defects in 2/3 and 2/7 cases, respectively. Typical examples for defect DLM/tendon structures are given in fig. 4.7 C (0.9 mM blebbistatin) and E (0.5 mM blebbistatin). The defect manifests in too short tendons and in the arrest of normally fast moving aggregates of GFP. This is easily seen, when images of defects are compared to images of control experiments (fig. 4.7 A-B). The low percentage of 28 % of defects at 0.5 mM blebbistatin indicates, that this concentration is at the lower end of defect inducing concentrations.
However, the incubation of pupae in equivalent DMSO concentrations resulted in similar percentages of defect DLM/tendon systems: 3/5 pupae and 2/4 pupae respectively. Defects were similar to those observed with blebbistatin/DMSO/ddH_2O (see fig. 4.7 D and F). These findings suggest that DMSO may account for all defects independently of blebbistatin.
Therefore, the second incubation protocol (1/2 h incubation → exchange agent with glycerol → $\text{imaging}_{19\,\text{h}}$ → 27 °C → $\text{imaging}_{22\,\text{h}}$) with less incubation time was tested. With the shorter incubation time DMSO was expected to cause less defects, thus enabling the observation of a potentially weaker phenotype of blebbistatin. However, 1/2 h incubation time in 0.5 mM blebbistatin in DMSO/ddH_2O resulted in a low rate of similar defects (1/5 pupae, imaging right after incubation). The defect persisted until the second round of imaging. All other pupae did not show a defect, neither during the first nor during the second imaging.

Summary & conclusion Both blebbistatin in DMSO and water as well as DMSO in water caused visible defects in the myotendious system of DLMs, which manifested in improper muscle compaction/tendon elongation and inhibition of the transport machinery in tendon cells. These results indicate that DMSO is sufficient to induce the observed defects in DMSO/ddH_2O as well as in blebbistatin/DMSO/ddH_2O experiments. In tested concentrations blebbistatin did not have visually noticeable additional effects. DMSO is not known for a myosin II specific effect. Hence, DMSO is not suitable for optical severing experiments with the aim to reveal the contribution of myosin to tension formation. However, the fact that DMSO did have an effect on the myotendinous system of DLMs is a promising hint, that agents may in principle be applied with the newly developed protocol and that agents, at least small ones like DMSO, can indeed reach DLMs within 1/2 h, although longer incubation times (4 h) probably increase the efficacy.

4.2. Dorsal abdominal muscles

Recently, Weitkunat *et al.* have shown, that tension is built up during the development of the myotendinous system of DLMs [92]. It is involved in cytoskeletal restructuring and thus essential for myofibrillogenesis in DLMs [92]. These results have been complemented by work in this thesis (see section 4.1). So far, investigations have been restricted to the specialized DLMs. Hence, it is unclear, whether tension build up is a unique feature in DLM (or indirect flight muscle) development, or if tension plays a general role during *in vivo* muscle development. Moreover, contractile activity (as opposed to passive tension) was proposed to play a major role in sarcomerogenesis [20]. However, this hypothesis was

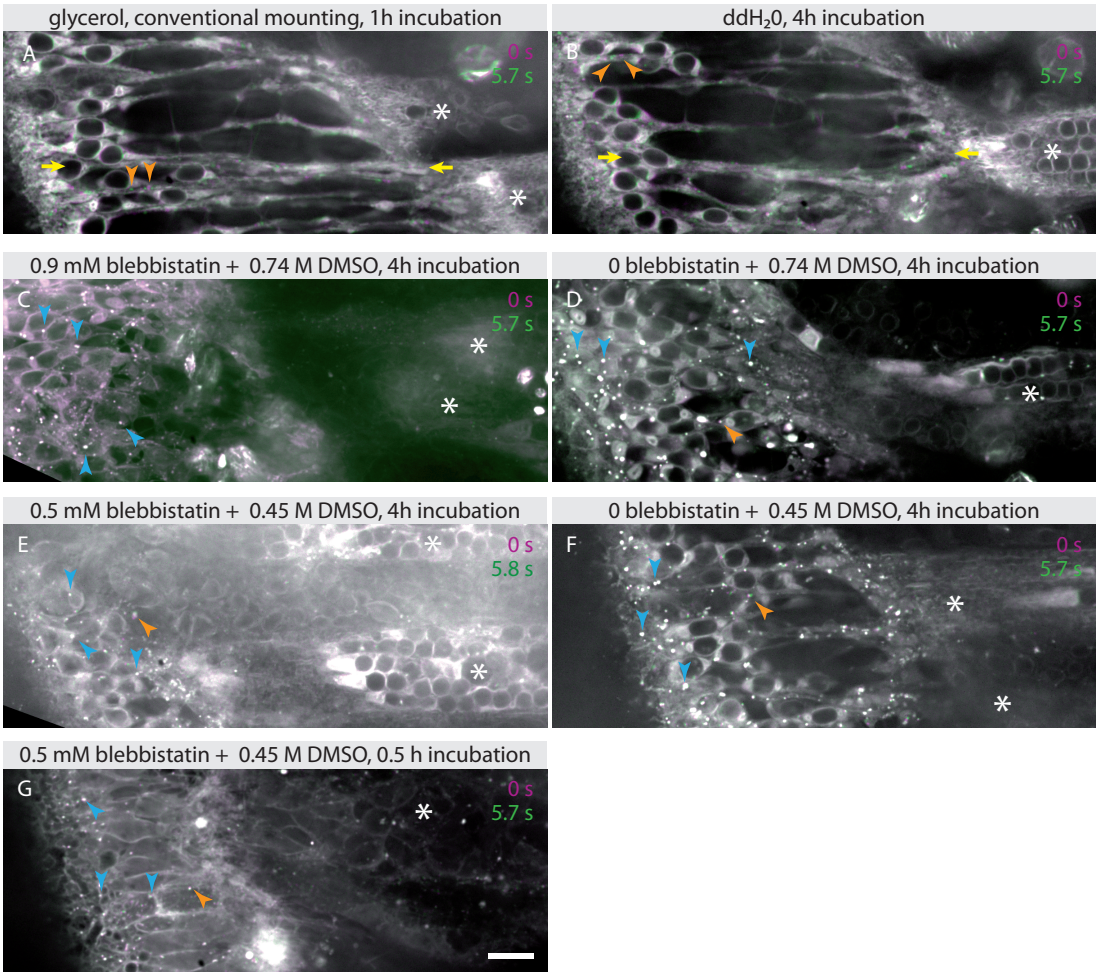

Figure 4.7.: Details of the myotendinous system of DLMs (asterisks) in pupae of [☿ y,w, UAS-CD8-GFP; y,w, UAS-CD8-GFP x ♂ y,w, UAS-CD8-GFP; Mef2-GAL4, sr-GAL4/TM3(Ser)] (A-F) and [UAS-palmitoylated-Cherry x Mef2-GAL4, sr-GAL4/TM3] (G). Scale bar 10 µm. Images are overlays of two time points (t_1: magenta, t_2: green; still structures appear white) separated by Δt =5.7 s or 5.8 s. A-B| Pupa during muscle compaction conventionally mounted in glycerol at 22 h APF (A) or mounted in ddH_2O according to new protocol at 18 h APF and imaged after 4 h of incubation (B). Tendons are well elongated (ends of example marked with yellow arrows). GFP-accumulations (bright small dots) move rapidly and thus appear in magenta and green, not white (one example each marked with orange arrow heads). C-G| Pupae at 23 h APF, which had been treated with 0.9 mM (C) and 0.5 mM (E) blebbistatin (in DMSO and ddH_2O) or the equivalent concentration of DMSO (D, F) according to the new protocol at 18 h APF. Incubation time was 4 h (C-F) or 1/2 h (G). Tendons are too short and the majority of GFP-accumulations do not move as seen from white dots (blue arrow heads mark several examples). Only few GFP-dots move, but very slowly and undirected (orange arrow heads).

inferred from experiments in cell cultures and a direct verification *in vivo* remains to be given.
To address these problems, optical severing experiments were performed in dorsal abdominal muscles, which are structurally and functionally different from DLMs (see section 3). By cutting the muscles a potential tension would show through a relaxation movement of the cut structures. Active contractility was assessed via optical stimulation. Calcium ion fluxes and additional information on inherent contractile activity of dorsal abdominal muscles were analyzed to gain a better understanding of developmental steps. With regard to further interpretations in chapter 5, the formation of internal muscle structures, which was investigated by our collaboration partners, is shown. Results presented in this chapter are currently prepared for publication in a scientific journal.

4.2.1. Tension and contractile activity in dorsal abdominal muscles

4.2.1.1. Experimental and analysis procedures

Experimental procedures Pupae were aged at 27 °C and prepared for imaging and nanodissection as described in section A.3. Four different time points were investigated: 36 h, 40 h, 46 h, and 52 h APF. Experiments were carried out in five different genotypes: [Mef2-GAL4, UAS-GFP-Gma], [♂ Mef2-GAL4, UAS-GFP-Gma x ☿ UAS-Cad-GFP], [♂ Mef2-GAL4 x ☿ UAS-GCaMP6f], [♂ Mef2-GAL4, UAS-Cherry-Gma x ☿ UAS-GCaMP6f], and [♂ Mef2-GAL4, UAS-CD8-Cherry x ☿ UAS-GCaMP6f] [4]. Optical severing was performed on each pupa, while it was being imaged on the NDD in confocal mode. The field of view contained the target muscle as well as several neighboring dorsal abdominal muscles of the same abdominal segment (and hemi-segment). Different grades of severing were achieved by using different laser intensities and different numbers of laser shots, starting from one shot with one laser pulse for small injuries up to several shots in two different z-levels for complete muscle cuts. Laser power and repetition rate needed to be adjusted to the age of the pupa, the size of the target muscle and its depth below the surface: These features vary for different individuals and time points, and the window for settings that result in clean cuts without disturbing bubble formation is narrow (see section 2.3).

Qualitative analysis of muscle responses In order to classify the response of muscles to optical severing and to identify positive tension (the muscle is stretched, as opposed to negative tension, when the muscle is compressed) and contractile activity, all movies were manually screened considering two aspects. First, the severity of the injury is registered. Instant complete rupture, sequential complete rupture, partial rupture (micro-lesions), and very small, barely noticeable injuries (nano-lesions) are distinguished. Second, the movement in three regions of interest (ROIs), specifically cut edges, muscle ends/attachment sites, and muscle outline/structures along the muscle, was observed. For all three ROIs the presence of movement and its direction, towards or away from the cut, were evaluated. This will enable the verification or falsification of tension. A movement of structures in a ROI away from the cut is a necessary prerequisite for the release of positive tension. However, it is not sufficient to unambiguously verify passive tension because other processes such as active contraction and depolymerization could also account for a movement after cutting

[4] A detailed description of all genotypes is given in appendix A.1.

(see below). Additionally, structures along the muscle and muscle outlines were checked for undulations. A movement of attachment sites towards each other and of structures along the muscle towards each other, in combination with undulations, is a clear indicator for a contractile process. Importantly, a distinction of passive relaxation or contraction upon negative tension (when the muscle had resisted a compression before cutting) and active (motor-driven) contraction is also not trivial and will be discussed in chapter 5. For now, the term contraction can only reflect the behavior of the muscle but not its underlying cause. In order to prevent confusion, such muscle responses will be referred to as *induced contraction* because they were caused by non-muscle inherent optical stimuli. According to the above-mentioned observations, seven different classes of responses were defined:

- Class I: Instant complete rupture. All ROIs move away from the target site. Evaluation of *induced contraction* is impossible.
- Class II: Sequential and thus delayed complete rupture. During the time preceding rupture completion neither undulations nor a movement of ROIs towards the target site occur: no *induced contraction*.
- Class III: Partial rupture (micro-lesion). Movement is observed at cut edges, in structures along the muscle and for attachment sites. Neither undulations nor a movement of ROIs towards the target site occur: no *induced contraction*.
- Class III": Partial rupture (micro-lesion). Movement is observed at cut edges and for structures along the muscle. Attachment site movement cannot be verified. Neither undulations nor a movement of ROIs towards the target site occur: no *induced contraction*.
- Class III': Partial rupture (micro-lesion). Movement is observed at cut edges but in no other ROI. Neither undulations nor a movement of ROIs towards the target site occur: no *induced contraction*.
- Class IV: Sequential complete rupture. During the time preceding rupture completion, undulations and a movement of ROIs towards the target site occur: *induced contraction*.
- Class V: Partial rupture (micro-lesion). Undulations and a movement of ROIs towards the target site occur: *induced contraction*.
- Class VI: Nano-lesion. Undulations and a movement of ROIs towards the target site occur: *induced contraction*.

Non responding muscles were not further analyzed, as it is not possible to decide why a muscle did not respond. It may have been due to an undervalued stimulation or due to an inability of the muscle to respond to any stimulus.

For the qualitative evaluation of relaxation upon positive tension and *induced contraction* the following argumentation applies:

- *Induced contraction*: Classes IV/V/VI contain muscle responses that show *induced contraction*, while classes II/III/III"/III' represent muscle responses without *induced contraction*. In class I *induced contraction* cannot be evaluated due to the instant complete rupture.

- Tension: Classes I/II/III are suitable for tension verification. Depolymerization, which could alternatively cause movement of cut edges can be excluded due to movement in at least two different ROIs. Overall contractile activity did not occur. In classes I/II/III attachment site movement is an unambiguous indicator of tension release. Active transport or a partial contractile process of single cut structures as the origin of movement in partially cut muscles may not be excluded for classes III"/III' and depolymerization may be excluded for class III" but not for class III'. However, the retraction of cut edges in partially cut muscles of classes III"/III' might also be caused by tension release. Therefore, classes III"/III' are indistinct with respect to tension confirmation. Hence, the observation of response types of classes I/II/III indicates tension release. Classes IV/V/VI do not contribute to tension evaluation because the presence of a potentially active contractile movement (*induced contraction*) renders a qualitative evaluation of an underlying passive tension impossible.

Bubble formation during abdominal muscle severing As described earlier (see section 2.3.4) inadvertent bubble formation may occur in the vicinity of the laser focus as a side effect of optical severing. Bubbles influence the movement of the surrounding material as can be directly observed at hemocytes, which bounce back and forth as long as bubbles are present. After the last bubble had disappeared, observed hemocytes stopped to move. Hence, a quantitative analysis of deformation velocities will always reflect bubble kinetics instead of the usually desired kinetics of the severed structures, especially at early times after severing. Thus, in cases, where a quantitative analysis of retraction velocities is required, bubble formation will render an experiment useless. However, for a qualtitative analysis of abdominal muscle severing, the situation is different. Although a quantitative analysis of retraction velocities is not possible when bubbles are present, bubbles do not seem to influence the overall qualitative response of the severed structures. This is supported by several observations. First, grouping muscle responses upon optical severing according to the classes defined in the previous paragraph, experiments in equally aged pupae still end up in the same class, independent of bubble formation. Second, muscle retraction outlasts bubble lifetime and in some experiments with ongoing bubble formation cut ends started to retract with a superimposed waggling movement, which stopped upon disappearance of bubbles, suggesting that bubbles influence other structures mainly during their lifetime. Third, the main direction of movement upon optical severing is always along the long muscle axis independent of bubble presence. This suggests that the observed movement is muscle inherent and not due to bubble formation.
In some cases of abdominal muscle severing bubble formation may even be considered an advantage: With approximately 10 µm in diameter abdominal muscles are extremely thick targets for optical severing and it is often very difficult to decide whether a cut was complete or not. This, however, may be an important aspect for experiments, e.g. when a disconnection of the muscle halves is required. However, in some cases big partial lesions and complete ruptures are hard to distinguish, e.g. when hemocytes obscure the muscle or when the muscle changes its z-level. Here, bubble formation may help to ensure complete rupture.
All in all, experiments in dorsal abdominal muscles with bubble formation may not be used for quantitative velocity analysis, but are helpful for qualitative conclusions and were therefore included in qualitative analysis.

4.2.1.2. Tension in early dorsal abdominal muscles at 36 h & 40 h APF

In this subsection responses of dorsal abdominal muscles in 36 h and 40 h old pupae to optical severing will be shown. The first two paragraphs present the morphology of muscle responses upon complete rupture and micro-lesions, respectively. A third paragraph gives a detailed quantitative classification of all experiments. In the two final paragraphs conclusions concerning tension and *induced contraction* are presented.

Complete rupture An overwhelming majority of dorsal abdominal muscles that received an optically created complete cut at 36 h or 40 h APF showed a clear response. It was characterized by a movement of cut edges, structures along the muscle, and attachments (ROIs) away from the cut.
Representative examples of completely cut abdominal muscles at 36 h and 40 h APF are shown in fig. 4.8. The retraction of the cut edges becomes already clear in image sequences (figs. 4.8 A-C and F-H), whereas the movement of the other ROIs is best revealed by kymographs[5] (figs. 4.8 D and J). In the kymographs, cut edges as well as attachment sites and prominent structures along the muscles are represented by curved lines, demonstrating a movement of these ROIs away from the cut. Importantly, the responses were quite heterogeneous, independently of time points: The amount of ROI movements varied among individual experiments. Moreover, some muscles showed an (almost) instant completion of rupture (class I), such as the one shown in fig. 4.8 F-J, while others ripped slowly apart (fig. 4.8 A-E, class II).

Micro-lesions When a partial lesion (micro-lesion) was created at 36 h and 40 h APF, movements resembling those upon complete rupture at 36 h or 40 h were observed, but in an alleviated manner. As can be seen in fig. 4.9, cut edges and prominent structures along the muscle clearly still moved apart. This becomes clear from an image sequence of the relaxation process upon optical severing as well as from the corresponding kymograph, which shows curved lines for the ROIs. The strength of the movement varied depending on the severity of muscle injury. Smaller lesions usually induced less movement. This holds also true for movements of muscle ends (attachment sites). However, as this ROI was showing the smallest movements upon complete ruptures, it is not surprising that attachment site movement could only unambiguously be identified for rather large partial lesions. The differences are easily seen, when comparing ROI movement in the examples in fig. 4.9. The larger lesion, which was chosen from the pool of cuts at 36 h, resulted in movement of all ROIs including attachment sites. The smaller lesion, which was selected among the cuts at 40 h, caused smaller movements, especially of the attachments. Hence, in the case of micro-lesions attachment site movement is only a valuable ROI for bigger lesions. In some cases, cut edges were the only ROI showing movement.

Nano-lesions With laser intensities below those that caused micro-lesions neither a lesion nor a muscle response were detected (see fig. 4.12 A-E). As already stated earlier, such cases were not further analyzed because a missing response could occur due to undervalued stimulation. Therefore, the number of unsuccessful severing attempts does not provide information on response behavior.

[5] For a short explanation of kymographs see footnote 3 of the current chapter.

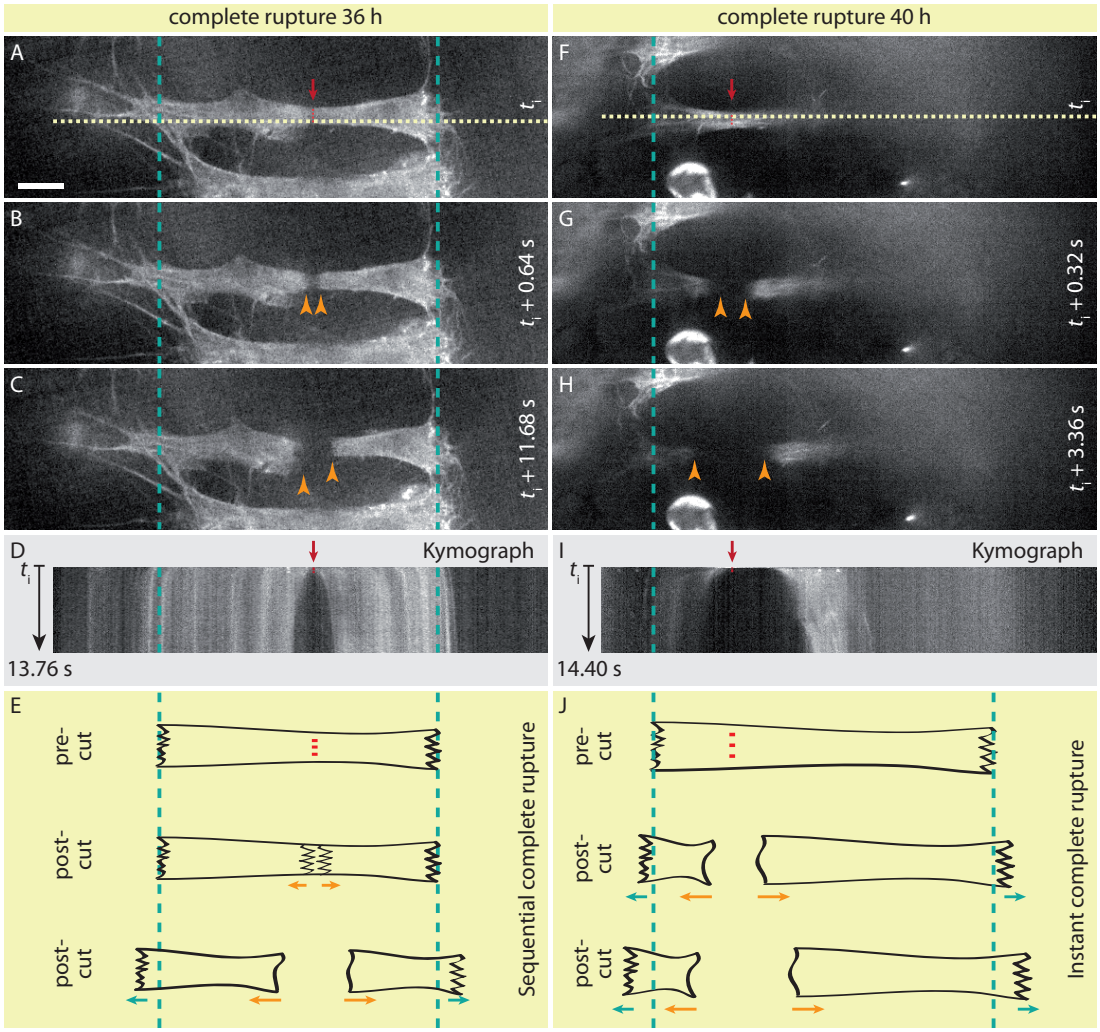

Figure 4.8.: Tension release in abdominal muscles at 36 h (A-E) and 40 h (F-J) APF upon complete rupture. A-C, F-H| Still images taken from SD confocal movies of dorsal abdominal muscles in [Mef2-GAL4, UAS-GFP-Gma] pupae (indirectly GFP-labeled actin), showing optical severing responses of class I (instant complete rupture, A-E) and class II (sequential complete rupture, F-J). D, I| Kymographs of dashed horizontal lines in A and F. Orange arrowheads indicate position of moving cut edges, dashed blue-green lines are guides to the eye indicating the initial position of muscle ends/attachment sites. Red arrows point at positions of severing (red dots). Scale bar 10 µm, anterior left, dorsal up. E,J| Scheme of the processes occurring in A-C (E) and F-H (J). Orange and blue-green arrows indicate movement of cut edges and attachment sites, respectively. The cut at 36 h led to a partial rupture of the muscle which continued to open up, resulting in a sequential complete rupture. Internal structures as well as attachment sites moved apart. The cut that was chosen from the pool of 40 h cuts induced an almost instantaneous complete rupture. Both rupture types occurred at both time points.

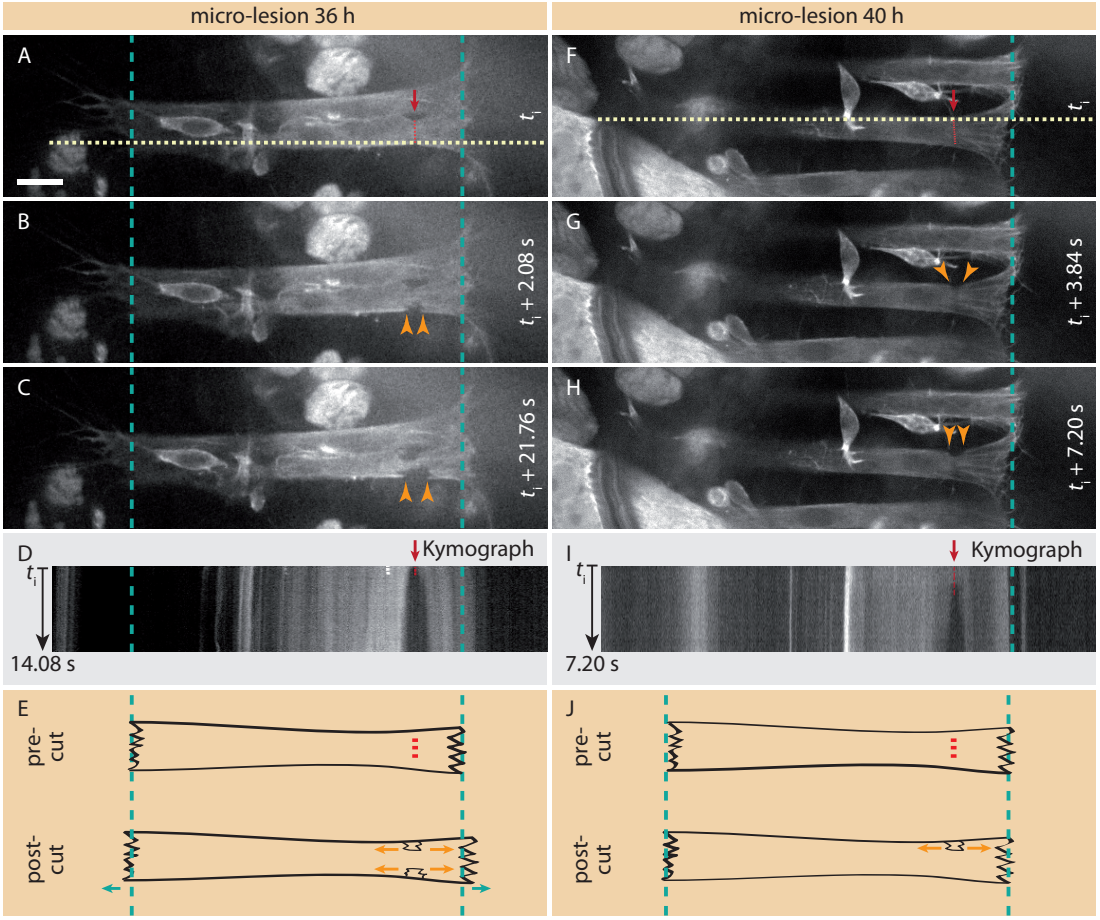

Figure 4.9.: Tension release in abdominal muscles at 36 h (A-E) and 40 h (F-J) APF upon micro-lesions. A-C, F-H| Still images taken from movies of dorsal abdominal muscles in [Mef2-GAL4, UAS-GFP-Gma] pupae (indirectly GFP-labeled actin), showing responses of class III: tension release upon partial ruptures of differing severity. The 36 h old muscle received a bigger lesion than the 40 h old muscle. D, I| Kymographs of dashed horizontal lines in A and F. Orange arrowheads indicate position of moving cut edges. Dashed blue-green lines are guides to the eye, indicating the initial position of muscle ends/attachment structures. Red arrows point at positions of severing. Scale bar 10 µm, anterior left, dorsal up. E,J| Scheme of the processes occurring in A-C (E) and F-H (J). Orange and blue-green arrows indicate movement of cut edges and attachment sites, respectively. The cut induced a partial rupture which opened up over time and led to small movements of internal structures and eventually attachments, but muscle integrity stayed intact. The amount of movement depended on the severity of the cut.

Quantitative classification of muscle responses The categorization of muscle responses upon optical severing of abdominal muscles at 36 h and 40 h APF into the classes defined in section 4.2.1.1 revealed the following result:
At 36 h APF $n = 33$ pupae were classified, with comparable numbers of complete ruptures ($n = 17$) and partial ruptures ($n = 16$). All responses were assigned to classes I (33.3 %), II (18.2 %), III (36.4 %), III" (9.1 %), and III' (3 %); other classes were not observed. 85 % of cuts at 36 h were first shots in the respective pupae (primary cuts), the remaining 15 % were the first noticeable injury in the respective pupa or the first attempt in the respective muscle. No difference in the qualitative behavior of primary and non-primary cuts was observed. Bubble formation was only an issue for complete cuts. In classes I/II only three pupae are unambiguously bubble free. In all other cases of classes I/II bubbles were seen ($n = 6$, 35 % of classes I/II) or not seen but suspected due to typical movement of surrounding structures ($n = 8$, 47 % of classes I/II). In classes III/III"/III' bubble formation was observed only once and not suspected for any other case.
At 40 h APF a total number of $n = 23$ cases was investigated, with $n = 9$ complete ruptures and $n = 12$ partial ruptures. 91 % of all cuts belonged to classes I (17.4 %), II (21.7 %), III (21.7 %), III" (8.7 %), and III' (21.7 %). Responses of type IV/V were observed for a negligible number of two cases (9 %). Eight of nine complete cuts involved bubble formation, whereas all partial cuts were bubble free. Again, with 87 % most of the cuts were primary cuts in the respective pupae and no difference to non-primary cuts was observed.

Tension As already explained in section 4.2.1.1 classes I/II/III indicate tension release, while for classes III"/III' tension is suspected but not unambiguously shown. For classes IV/V/VI tension release was considered to be completely unclear. Figure 4.10 A shows a synopsis of muscle responses at 36 h and 40 h APF and groups them according to their relevance for tension verification.
At 36 h APF 88 % of all cuts were assigned to classes I/II/III, clearly verifying tension release. In the remaining 12 % of classes III"/III' tension could neither be verified nor falsified.
At 40 h APF 61 % of all cases tension was verified due to their classification as type I/II/III. In the remaining cases, which belonged to classes III"/III' (22 %) or IV/V (9 %), tension could neither be verified nor falsified.
In summary, passive tension was verified for dorsal abdominal muscles in 36 h and 40 h old pupae.

Induced contraction The occurrence of *induced contraction* in dorsal abdominal muscles upon optical severing at 36 h or 40 h APF is shown in fig. 4.10 B. Here, response classes were grouped according to their relevance for contractile movement. As explained in section 4.2.1.1 classes IV/V/VI verify contraction, classes II/III/III"/III' falsify contraction and class I is unclear.
At 36 h APF, 67 % of all muscle responses did not show *induced contraction* (classes II/III/III"/III') and no muscle showed a response of type IV/V/VI. The remaining cases were unclear (class I).
At 40 h APF the situation is comparable. 74 % of muscle responses did not show *induced contraction*. 17 % were unclear (class I). 9 % did show *induced contraction*. However, this number is negligible within the heterogeneity of biological samples.

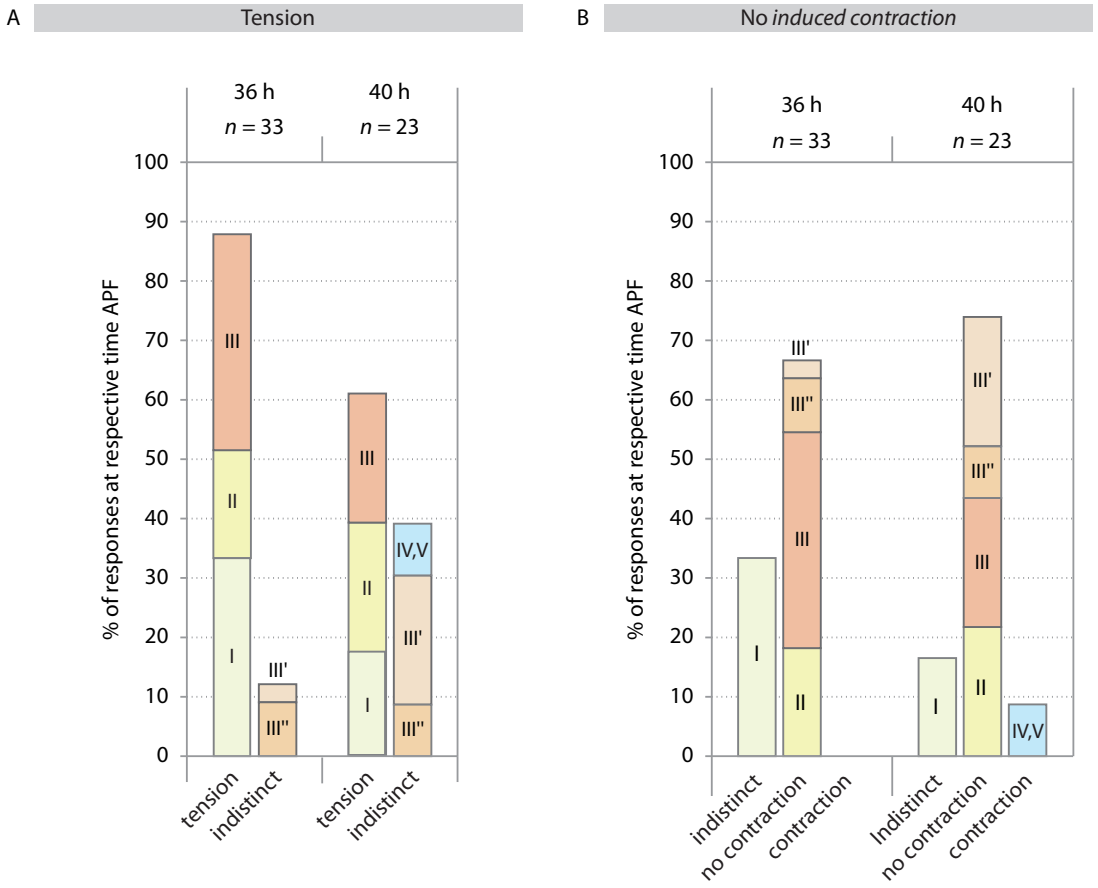

Figure 4.10.: Abdominal muscle response to optical severing at 36 h and 40 h: tension release & no *induced contraction*. Cuts were assigned to response classes I (dark yellow: instant tension release upon complete rupture), II (pale yellow: delayed tension release upon complete rupture, no *induced contraction*), III (dark orange: tension release upon partial rupture, no *induced contraction*), III''/III' (pale orange: partial rupture, no *induced contraction*, tension release possible but unclear), IV (*induced contraction* upon complete rupture, tension release unclear), and V (*induced contraction* upon partial rupture, tension release unclear). Detailed definitions of all response classes are given in section 4.2.1.1. Bars indicate percentage of responses, normalized on the total number n of responses at the respective time point. A| Classes I, II and III verify tension release for both time points. B|The majority of cases belongs to classes without *induced contraction*.

The findings demonstrate clearly that dorsal abdominal muscles at 36 h and 40 h APF do not show *induced contraction* upon optical severing, neither with sequential complete rupture (class II) nor with partial rupture (classes III/III"/III').

4.2.1.3. *Induced contraction* in dorsal abdominal muscles at 46 h & 52 h APF

In the current subsection responses of dorsal abdominal muscles in 46 h and 52 h old pupae to optical severing will be shown. The first paragraph present the morphology of muscle responses upon complete rupture and micro-lesions, while the second paragraph describes the morphology of muscle responses on nano-lesions. The third paragraph gives a detailed quantitative classification of all experiments. In the two following paragraphs conclusions concerning contractile movement and tension are presented, before the last paragraph summarizes observations on the behavior of target muscle neighbors.

Complete rupture & micro-lesions The response of abdominal muscles at later developmental time points (46 h and 52 h APF) upon optically induced complete rupture was different from that at earlier developmental time points. At 46 h and 52 h APF, mainly *induced contraction* was observed, independently of lesion size. Examples of induced contraction with complete or partial rupture at 46 h are presented in fig 4.11. (To avoid redundancy, images of *induced contraction* at 52 h are not shown.) Attachment sites moved towards each other and the muscle outline as well as internal structures undulated and contracted. In some cases of partial rupture a reverse movement of the muscle back into its initial muscle position (or close to it) was observed within seconds to minutes, while others remained in the contracted state throughout the observation period. A partial or complete disruption of a contracting muscle may lead to a movement of the ROIs away from the lesion, depending on the grade of contraction and the severity of the injury. Notably, such movements were sometimes impeded by a contraction process of a neighboring muscle, which held the target muscle in a contracted state. The interplay of the diverse movements during *induced contraction* are best seen from kymographs (figs. 4.11 D and I). As already mentioned, it is not clear, whether it is a passive or an active contraction. The discussion of this aspect will be postponed to chapter 5 when more results on this topic will have been presented.

Nano-lesions So far, obvious destruction of cytoskeletal structures had been used to create *induced contraction*. However, very small lesions (nano-lesions), which produce a barely or not noticeable destruction in the labeled actin structures, also led to *induced contraction* (class VI). A typical example is shown in fig. 4.12 F-J. Again, a movement of muscle ends towards each other with concomitant undulations of muscle structures was observed. Such a behavior was never observed at early time points: At 36 h or 40 h APF comparable cutting settings either created very small lesions with subsequent movement of ROIs away from the cut (as presented in the previous section), or they created no lesion and hence no movement or other noticeable response was observed (see fig. 4.12 A-E).

Quantitative classification of muscle responses The classification of muscle responses upon optical severing of abdominal muscles at 46 h and 52 h APF into the classes defined in section 4.2.1.1 revealed the following result:

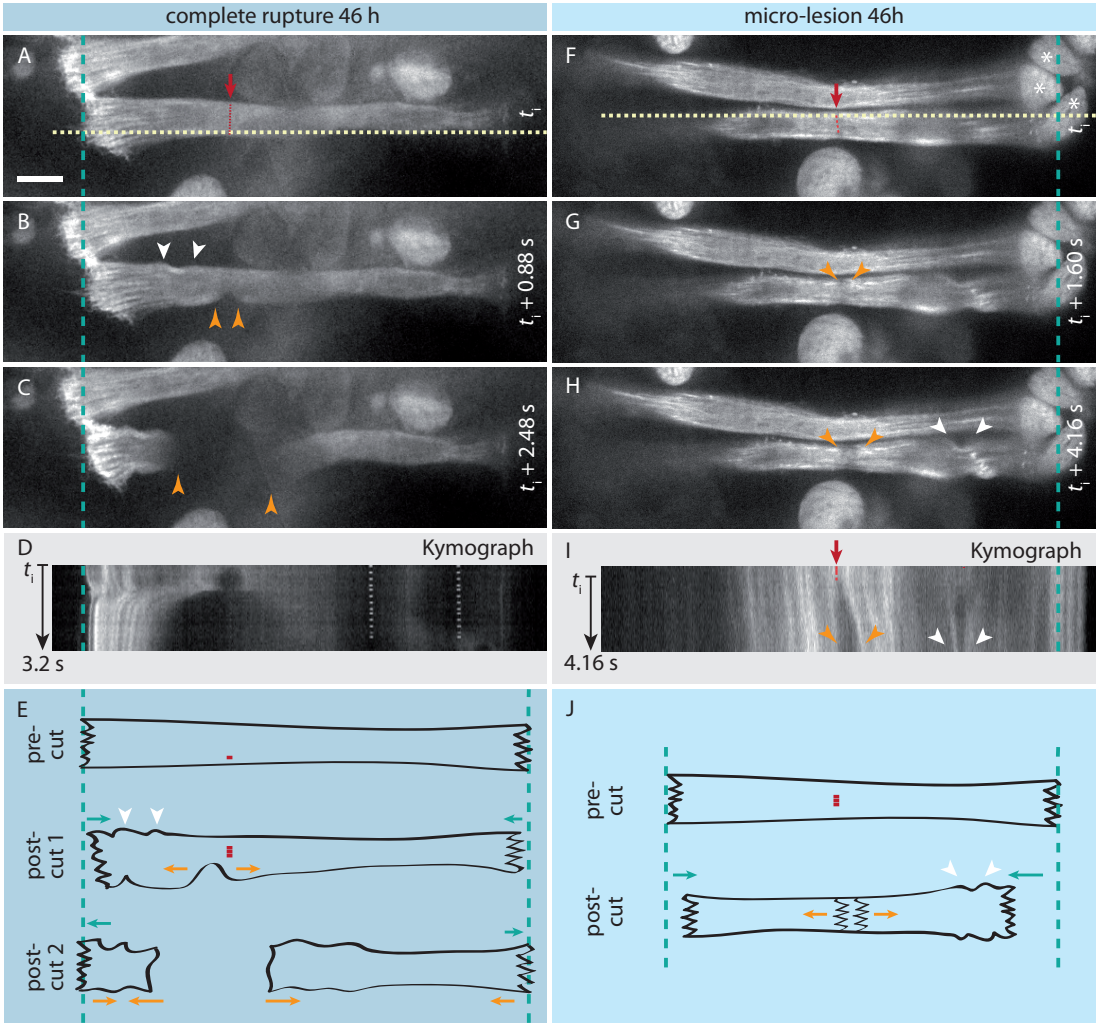

Figure 4.11.: *Induced contraction* in abdominal muscles at 46 h APF upon complete rupture (A-E) and partial rupture (F-J). A-C, F-H| Still images taken from SD confocal movies of dorsal abdominal muscles in [Mef2-GAL4, UAS-GFP-Gma] pupae. In (F-I) hemocytes (white asterisks in F) obscure the posterior muscle end. D, I| Kymographs of dashed yellow lines in A (D) and F (I). Orange arrowheads indicate movement of cut edges, dashed blue-green lines are guides to the eye, indicating the initial position of muscle ends (attachment structures). Red arrow points at position of severing (red dotted lines). E,J| Scheme of the processes occurring in A-C (E) and F-H (J). Orange and blue-green arrows indicate movement of cut edges and attachment sites, respectively. Scale bar 10 µm, anterior left, dorsal up.

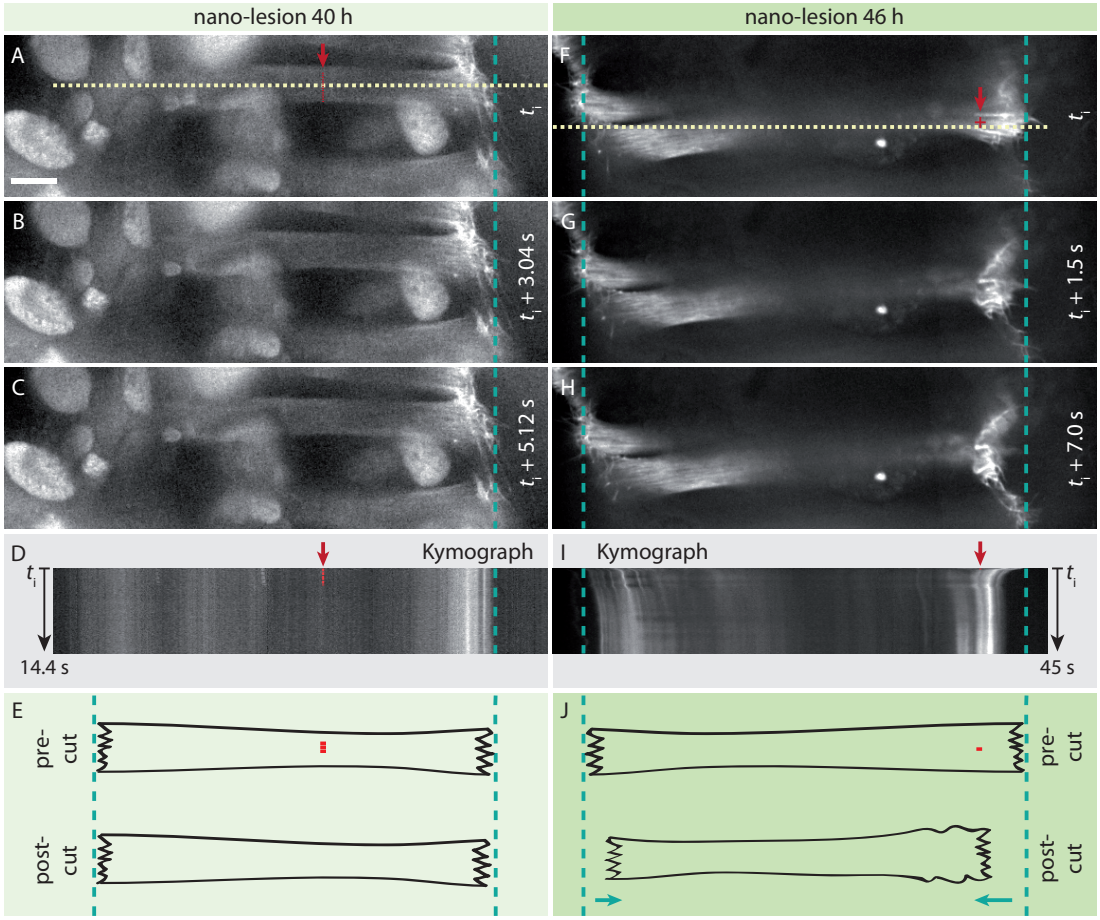

Figure 4.12.: Abdominal muscle response upon nano-lesions at 40 h (A-E) and 46 h APF (F-J). A-C, F-H| Still images taken from SD confocal movies of dorsal abdominal muscles in [Mef2-GAL4, UAS-GFP-Gma] pupae. D, I| Kymographs of dashed yellow lines in A (D) and F (J). Dashed blue-green lines are guides to the eye, indicating the initial position of muscle ends (attachment structures). Red arrows point at positions of severing (red dots or cross). E,J| Scheme of the processes occurring in A-C (E) and F-H (J). Orange and blue-green arrows indicate movement of cut edges and attachment sites, respectively. Scale bar 10 µm, anterior left, dorsal up. Nano-lesions did not produce a noticeable rupture of visible structures and led to *induced contraction* in muscles at 46 h APF but not at 40 h APF.

At 46 h APF $n = 47$ pupae were categorized. 96 % of all responses were assigned to classes IV/V (55 % *induced contraction* upon complete rupture and micro-lesions) and VI (41 % *induced contraction* upon nano-lesions). The remaining two cases were assigned to classes II and III' (2 % each). 57 % of all cuts were primary cuts. No difference to non-primary cuts was observed. Bubbles only appeared in experiments assigned to classes IV/V. Eight pupae experienced bubble formation (31 % of classes IV/V), nine cases were suspected (35 % of classes IV/V), and another nine cuts were considered bubble free (35 % of classes IV/V). In the cases of type II and III' bubbles were suspected.
At 52 h APF $n = 7$ pupae were categorized. Four cuts were assigned to classes IV/V and three cuts to class VI. All but one cut were first shots in the respective pupae. All cuts except nano-lesions led to bubble formation.

Induced contraction *Induced contraction* in dorsal abdominal muscles upon optical severing at 46 h or 52 h APF is also shown in fig. 4.13 B. Grouping response classes according to their relevance for *induced contraction* (classes IV/V/VI verify contraction, classes II/III/III"/III' falsify contraction and class I is unclear) clearly shows, that *induced contraction* was observed for 96 % and 100 % of all cases at 46 h and 52 h APF, respectively. Hence, *induced contraction* is the dominant response type at these later developmental time points.

Tension As already explained, classes I/II/III indicate tension release, for classes III"/ III' tension is suspected but not clearly shown, and for classes IV/V/VI tension release was considered to be completely unclear. The vast majority of responses to optical severing at 46 h and 52 h was categorized as classes IV/V/VI (see fig. 4.13 A). Hence, tension can neither be verified nor falsified because evaluation of passive tension is impossible for these time points.

Contractions in neighbor muscles Optical severing and imaging of target muscles (referred to as target) included imaging of other dorsal abdominal muscles of the same segment (referred to as neighbors). All visible neighbors of target muscles were analyzed for a contractile response.
At 46 h and 52 h a considerable percentage of *induced contraction* in target muscles was accompanied by contraction of at least one neighbor. At early developmental time points, 36 h and 40 h APF, no neighbor showed contractile movement. The detailed result is shown in fig. 4.14 A-B. In 47 % of all $n = 45$ cases with *induced contraction* in 46 h old targets an autonomous contractile movement of at least one neighbor was observed. An equal number of cases did not show contractile movement of neighbors. The remaining cases were unclear. At 52 h APF, neighbor contractile movement was confirmed for 86 % of $n = 7$ targets with *induced contraction*. At both time points the majority of neighbor contractile movements were seen with targets showing responses of classes IV/V (micro-lesions or complete rupture), indicating that the severity of the disturbance influences neighbor responses. A correlation of neighbor contractile movement with bubble formation points into the same direction (see fig. 4.14 C-D). At 46 h APF 62 % of neighbor contractile movements occurred along with bubbles (29 %) or suspected bubbles (33 %, inferred from typical movement of tissue). At 52 h APF 67 % of neighbor contractions occurred along with bubbles.

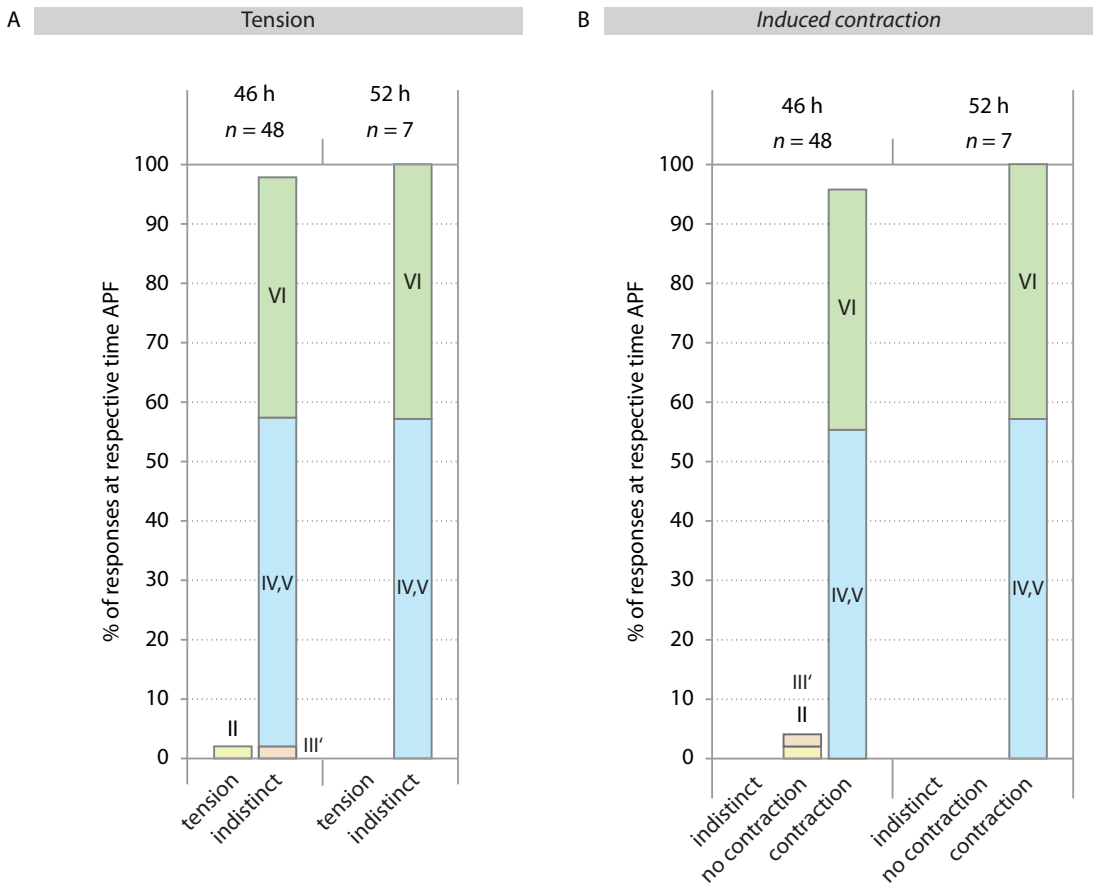

Figure 4.13.: Abdominal muscle response to optical severing at 46 h and 52 h APF: *induced contraction*. Cuts were assigned to response classes I (dark yellow: instant tension release upon complete rupture), II (pale yellow: delayed tension release upon complete rupture, no *induced contraction*), III (dark orange: tension release upon partial rupture, no *induced contraction*), III"/III' (pale orange: partial rupture, no *induced contraction*, tension release possible but unclear), IV (*induced contraction* upon complete rupture, tension release unclear), and V (*induced contraction* upon partial rupture, tension release unclear). Detailed definitions of all response classes are given in section 4.2.1.1. Bars indicate percentage of responses, normalized on the total number n of responses at the respective time point. At 46 h and 52 h classes IV/V/VI dominate and thus demonstrate *induced contraction* (B), while tension is neither verified nor falsified (A).

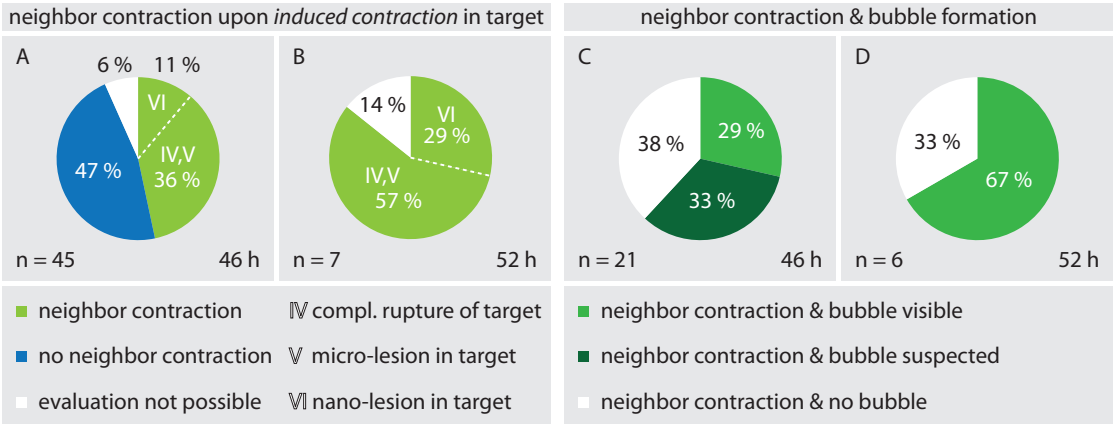

Figure 4.14.: Contractions in neighboring dorsal abdominal muscles upon optical severing in target muscles at 46 h (A, C) and 52 h APF (B, D). A-B| Percentage of target muscles showing *induced contraction* that were accompanied by autonomous contraction of a neighboring muscle. The majority of neighbor contractions occurred with micro-lesions/complete rupture. The full circle (100 %) corresponds to all cases of *induced contraction* in target muscles at the respective time point. C-D| Bubble formation accompanying neighbor contractions. The full circle (100 %) corresponds to all neighbor contractions at the respective time point.

4.2.2. Attachment site behavior

Attachment site behavior is investigated for four reasons. First, as mentioned previously, the distinction between a passive mechanism and an active (motor induced) contraction behind the process of *induced contraction* is not trivial (see chapter 5 for a thorough discussion). Hence, additional information is required to be able to draw conclusions about the underlying mechanisms of *induced contraction*. Here, the investigation of spontaneous contraction behavior at relevant time points (46 h APF and later) becomes interesting. It will reveal, whether active contraction is a naturally occurring and thus probable process behind *induced contraction* at the investigated time points. Second, a non-negligible number of *induced contractions* was found to be accompanied by neighbor contractions. Spontaneous neighbor contraction independent of *induced contraction* in the target muscle is a possible cause for these observation. This possibility is easily tested by evaluating the occurrence of auto-twitching. Third, spontaneous contraction is an indicator for stable attachment sites: From a developmental point of view muscle contractions that precede attachment site formation would not make sense because muscle contractions would disrupt evolving attachments. Finally, direct observation of epidermal cells adjacent to muscle ends will directly reveal, whether attachment sites are stable.

4.2.2.1. Inherent behavior without stimulation: auto-twitching

Experimental procedure and analysis 25 living [Mef2-GAL4, UAS-GFP-Gma] pupae, aged to 46 h, 48 h, or 50 h APF at 27 °C, were prepared for experiments on the NDD as described in section A.3. For each experiment a new pupa was used. In each pupa dorsal abdominal muscles were observed for a continuous period of approximately 19 min. Longer observation periods were not possible because movies had to be recorded at the high rate of 6.25 fps (160 ms/frame) in order to ensure that even short twitches were resolved. The field of view in the NDD was approximately 120 µm x 170 µm and showed around five to eight muscles at a time. Muscles were, depending on position and orientation of the pupae, usually partially visible. Due to developmental rearrangements and movement in the pupa, the z-level had to be adjusted occasionally during recording in order to keep relevant muscles in focus.
To extract the average contraction behavior of muscles at the respective developmental time point, every muscle was analyzed for its number of auto-twitches (spontaneous muscle contraction without any external stimulation) during the observation period. The number of visible muscles in a pupa was evaluated as the mean value of the maximum and minimal number of visible muscles in that pupa during the observation period, respectively.

Auto-twitching: results In total 230 min (n=12 pupae), 96 min (n=6), and 134 min (n=7) of abdominal muscle development at 46 h, 48 h, and 50 h APF, respectively, were analyzed. All observed auto-twitches consisted of a contraction phase followed by a relaxation back into the original position. The results of the quantitative analysis on the occurrence of auto-twitches is presented in fig. 4.15. At the earliest investigated time point of 46 h APF auto-twitching occurred rarely (0.045 ± 0.007 twitches per muscle during observation time $\pm$ standard error) and in a small fraction of pupae (17 %). The developmental stage of 48 h did not show a significant difference. At 50 h APF the fraction of pupae showing auto-twitching had increased to 71 %, which is a significant (two-tailed Fisher's exact test) difference to 46 h APF. This observation was also reflected in the number of 0.84 ± 0.17 auto-twitches per muscle during the observation period.
These results show three important aspects. First, the small number of auto-twitching pupae/muscles at 46 h and 48 h indicates, that spontaneous contraction can occur as early as 46 h APF. However, it is a rare event. This observation is neither a strong argument for nor against an active process behind *induced contraction*. Second, the low number of muscle contractions even at 50 h APF renders the occurrence of spontaneous neighbor contraction during the short observation time in experiments on induced contraction very unlikely. Third, the increased number of auto-twitches at 50 h APF suggests that attachment sites are strongly connected before 50 h APF.

4.2.2.2. Posterior attachments during *induced contraction*

Experimental procedures [Mef2-GAL4, UAS-GFP-Gma x UAS-Cad-GFP] pupae were aged to 46 h APF at 27°C and prepared for live imaging as described in section A.3. In these pupae, muscles are visible due to an indirect GFP-labeling of actin. Additionally, cadherins have a GFP-label, which results in fluorescent apical cell outlines in the epidermal layer around the muscles. However, due to geometrical constrictions, it was not possible to image muscle attachments together with those epidermal cells outlines that were closest

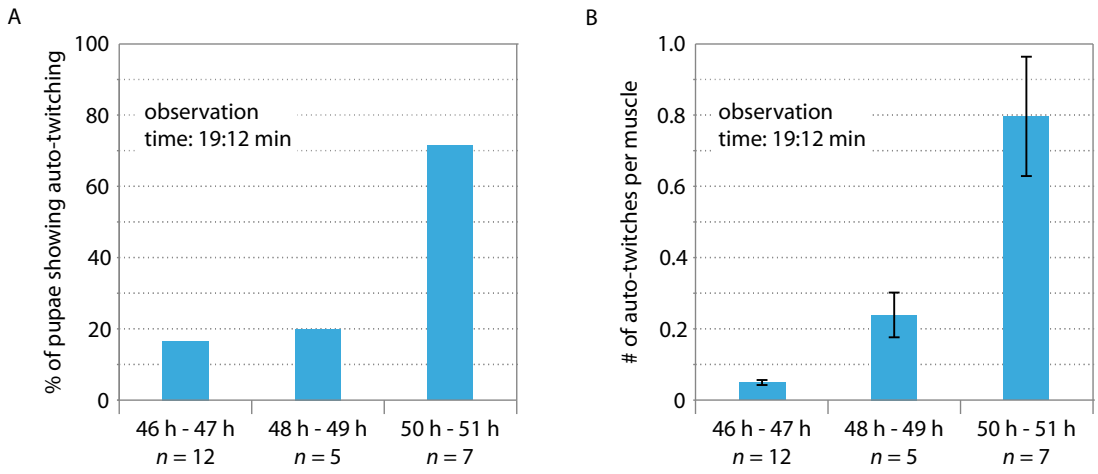

Figure 4.15.: Auto-twitching in abdominal muscles at three different ages APF: 46 h (n=12 pupae), 48 h (n=5 pupae), and 50 h (n=7 pupae). A| Bars indicate the fraction of pupae at the respective time APF, that showed auto-twitching during an observation period of 19:12 min per pupae. B| Bars indicate the number of auto-twitches per muscle during the observation period of 19:12 min.

to the attachment. Instead, the behavior of posterior attachment sites of muscles showing *induced contraction* upon single pulse laser shots were observed together with epidermal cell outlines at some distance.

Results Figure 4.16 gives an overview of the results. Pictures (A-C) are an image sequence of a muscle end showing a typical *induced contraction* response, which manifests in undulations and an anteriorward movement of the observed posterior muscle end. This movement is easily seen from the sequence as well as from a kymograph along the main direction of movement (fig. 4.16 D). Here, the muscle end is represented by a curved line, which verifies movement. Due to the low intensity of epidermis cell outlines, their movement is best seen from the kymograph. The lines, which represent cell outlines (orange markers), clearly show a curvature, which qualitatively resembles that of the attachment line (blue-green markers), demonstrating an anteriorward movement. The movement of observed cells was often less pronounced than the movement of muscle ends. This can be explained by assuming a simple passive elastic answer. The observed cell outlines are a certain distance away from the muscle end and are therefore expected to move less than the muscle end itself.
In most cases (9 of 12 muscles in 11 pupae, 75 %) *induced contraction* was accompanied by a movement of the surrounding epidermal cell outlines (fig. 4.16 E). Only one muscle did not show a detectable movement of epidermal cells. In the remaining two cases, observation was obscured and a movement could neither unambiguously be verified nor excluded. Eight muscles (including the one without movement) were stimulated with the first attempt in the respective pupae (primary shot), three muscles were the first reaction in this pupa but needed two stimulation attempts, and one muscle was the second muscle in the pupa to be stimulated. No significant difference in behavior was seen for these groups.
In summary, 75 % of induced contractions in pupae with labeled cell outlines resulted in

a concomitant movement of adjacent epidermal cells. This demonstrated that attachment sites are strong enough to withstand *induced contraction*.

4.2.3. Ca^{2+} flux

Muscle activity in operating abdominal muscles requires influx of Ca^{2+} from the sarcoplasmic reticulum into the cytosol (see section 3.2.2). Hence, important information about the underlying processes of *induced contraction* will be gained by observing Ca^{2+} flux in abdominal muscles that are subject to *induced contraction*. Ca^{2+} activity upon stimulation of *induced contraction* would be a strong indicator for an active mechanism behind *induced contraction*. Furthermore, data on functional stages in general will be collected by investigating the presence of the Ca^{2+} machinery with respect to functional and structural stages.

4.2.3.1. Visualization of Ca^{2+} in Abdominal Muscles

For observation of Ca^{2+} behavior during *induced contraction* sample properties have to fulfill several requirements: First, a fluorescent calcium reporter with suitable spectra needs to be expressed in muscles only. Second, the reporter needs to be bright enough for observation with the SD unit of the NDD. Third, fast kinetics are favorable, as this enables visualization of rapid changes in calcium concentration. Fourth, for experimental practicability the non-stimulated muscles need to be bright enough to find and aim at them. Nevertheless, resting signal and stimulated signal need to be distinguishable.
Among the various molecules, which are known as fluorescent calcium reporters [2], the protein GCaMP6f was chosen, because its kinetics are among the fastest [2] and its fluorescence spectra are compatible to the NDD. GCaMP6f was engineered by Chen *et al.* from several well known building blocks. Circularly permuted green fluorescent protein, calmodulin with its calcium binding unit, and M13 peptide were used to create the protein. Due to calcium-dependent conformational changes it only fluoresces when calcium is bound. [11]
Four different genotypes were tested in order to find a suitable phenotype. [☿ y,w; ; Mef2-GAL4 x ♂ UAS-GCaMP6f] pupae were found to show a sufficiently high fluorescence upon calcium influx during spontaneous muscle contractions at 72 h APF. However, the intensity of abdominal muscles at rest (resting intenity) was not detectable. Although the level of resting fluorescence is slightly higher at the time point of interest at 46 h APF, it is time consuming and barely possible to find and aim at abdominal muscles. Thus alternative approaches were tested. They require a second label, either a second color in abdominal muscles or a second structure with a GFP label, but with a comparable brightness in order to not outshine the calcium signal. [☿ UAS-GCaMP6f x ♂ Mef2-GAL4, UAS-rhea-GFP] was tested as a possibility for pupae with a second, equally bright GFP signal. However, as the rhea-encoded GFP signal in muscle attachment integrins was not detectable, this cross was unsuitable for the intended experiment. The third and fourth tested crosses were [☿ UAS-GCaMP6f x ♂ Mef2-GAL4, UAS-Cherry-Gma] and [☿ UAS-GCaMP6f x ♂ Mef2-GAL4, UAS-CD8-Cherry]. Here, a sufficient amount of a second, red fluorophore (cherry) is expressed in muscles at the required time point and excitation is regulated with the 561 nm laser. This has the advantage, that it is completely independent of GFP excitation and cherry intensity was regulated individually as required. However, in both cases cherry is also present in larval muscle remnants and, as an undesired side effect, in hemocytes, which

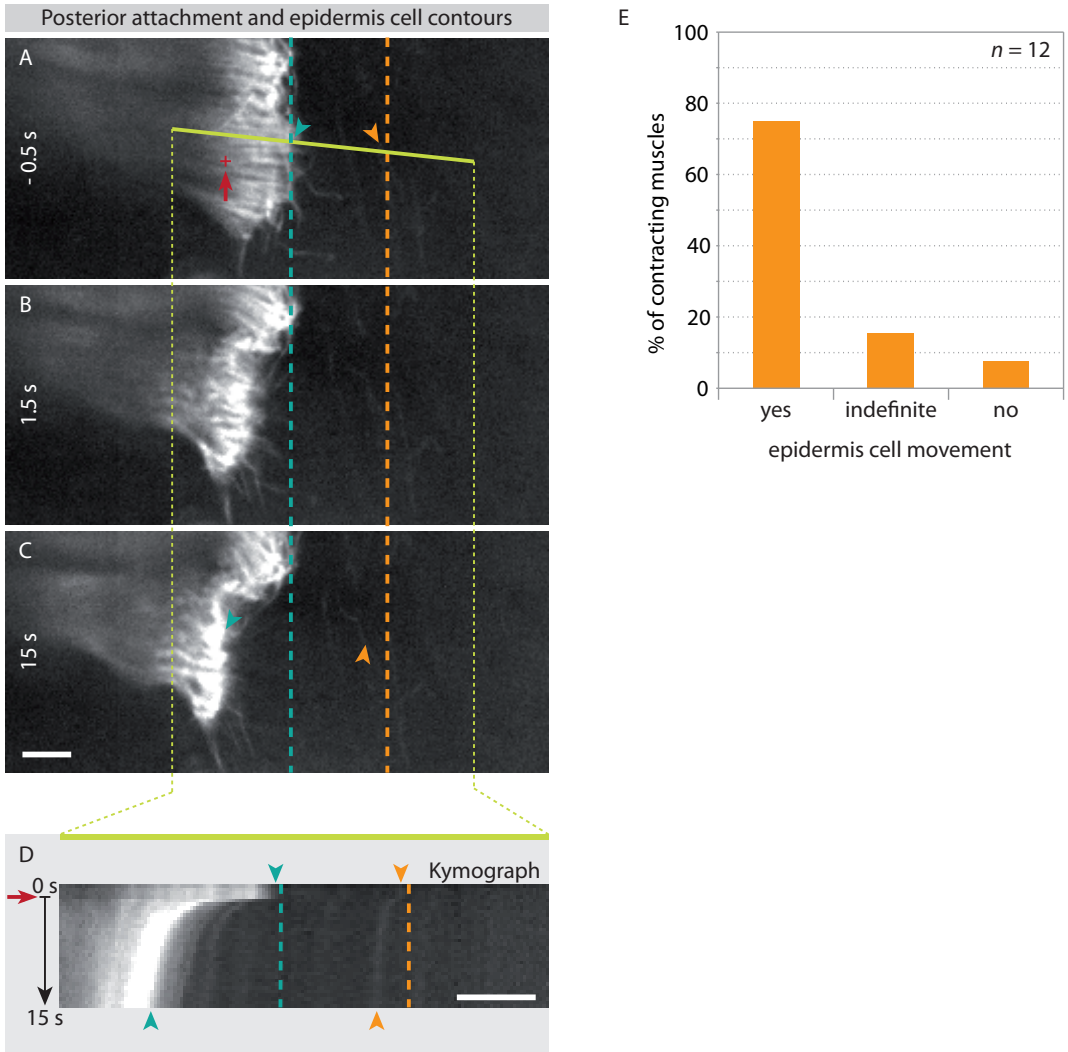

Figure 4.16.: A-C| SD confocal image sequence of a posterior epidermal cells around a posterior [Mef2-GAL4, UAS-GFP-Gma x UAS-Cad-GFP] dorsal abdominal muscle end, which was stimulated for *induced contraction* with a one pulse shot. Red arrow points at position of stimulation (red cross). Green line in (A) is presented as a kymograph (D). D| Kymograph. Red arrow indicates time of cut. *Induced contraction* of the muscle and concurrent movement of epidermal cell outlines are clearly visible from curved lines in the kymograph. Blue-green dashed lines are guides to the eye, indicating the initial position of the attachment, and arrowheads point at attachment (blue-green) and epidermal cell outline (orange) (A-D). Scale bars represent 5 µm. E| Bar diagram showing the percentage of *induced contractions* that were accompanied by epidermal cell movement (75 %), those where epidermal cell movement was very small (movement questionable, 17 %), and those where no movement was observed (no movement, 8 %).

are much brighter than the muscles. As the intensity of the calcium signal is very weak (approximately a value of 15 to 20 on a 8 bit scale of 256 values and a background value of around 10) already a low cherry intensity in the muscles impedes observation of the calcium signal. Therefore, in experiments with emphasis on the exact behavior of Ca^{2+} the cherry signal was only used to find and aim at the muscles, but it was switched off during optical severing. As [Mef2-GAL4, UAS-CD8-Cherry] contains a balancer, it is more convenient to use progeny of [☿ UAS-GCaMP6f x ♂ Mef2-GAL4, UAS-Cherry-Gma]. The latter one produces the correct phenotype in all progeny, whereas the cross with the balancer produces the correct phenotype only in half of the progeny. Therefore most experiments were carried out in progeny of [☿ UAS-GCaMP6f x ♂ Mef2-GAL4, UAS-Cherry-Gma], although [☿ UAS-GCaMP6f x ♂ Mef2-GAL4, UAS-CD8-Cherry] would have been suitable from an imaging perspective.

4.2.3.2. Ca^{2+} flux in target muscles

Experimental procedure In order to clarify the role of calcium ions during *induced contraction*, pupae were aged to 40 h or 46 h APF and prepared for optical severing as described in section A.3. Living pupae were optically stimulated and imaged on the NDD. Movies were taken at a frame rate of 3.33 fps (300 ms/frame). Abdominal muscles of [☿ Mef2-GAL4 x ♂ UAS-GCaMP6f] (10 stimulations at 46 h), [☿ UAS-GCaMP6f x ♂ Mef2-GAL4, UAS-Cherry-Gma] (19 stimulations at 40 h, 20 stimulations at 46 h), and [☿ UAS-GCaMP6f x ♂ Mef2-GAL4, UAS-CD8-Cherry] (3 stimulations at 46 h) were stimulated with laser settings in the range of those, which had successfully induced lesions in former experiments (1 laser pulse at 1 point, cutting laser intensity according to muscle properties between 40 % and 52 % (40 h APF) or 40 % and 64 % (46 h APF) of maximum). Different laser intensities for optical stimulation were chosen to span the phase space of signal types.

Heterogeneous signals at 40 h and 46 h APF Optical stimulation of abdominal muscles reliably led to a clear GCaMP6f fluorescence signal in abdominal muscles at both time points, 40 h and 46 h APF. This clearly indicates a calcium influx into the muscle cytosol at both developmental time points, 40 h as well as 46 h APF.
Figure 4.17 A-C and fig. 4.18 A-C each show three examples of typical signal evolution upon stimulation at 40 h and 46 h, respectively. The examples reflect the heterogeneity of the induced signals, which vary in spread, duration, and intensity. Variations range from small, localized and short signals (figs. 4.17 A and 4.18 A) to bright, extended and longer lasting signals (figs. 4.17 B and 4.18 B), the latter being split in some cases (figs. 4.17 C and 4.18 C). In most cases (40 h: 63 %, 46 h: 78 %), the signal was transient: an increase of signal intensity was followed by an intensity decrease. Apart from the superimposed *induced contraction* at 46 h, signals in 40 h and 46 h old pupae were not distinguishable from their morphology.

To illustrate the intensity evolution of the three signal types, the evolution of the respective mean intensities during the first seconds after stimulation is shown in figs. 4.17 D and 4.18 D. The intensity evolution of the image areas shown in (A-C) was evaluated for all relevant frames (Fiji macro) and normalized on the mean intensity of available pre-cut frames, which was set to zero. The values were corrected for background bleaching. The resulting curves reflect the qualitative observation of three different signal types with dif-

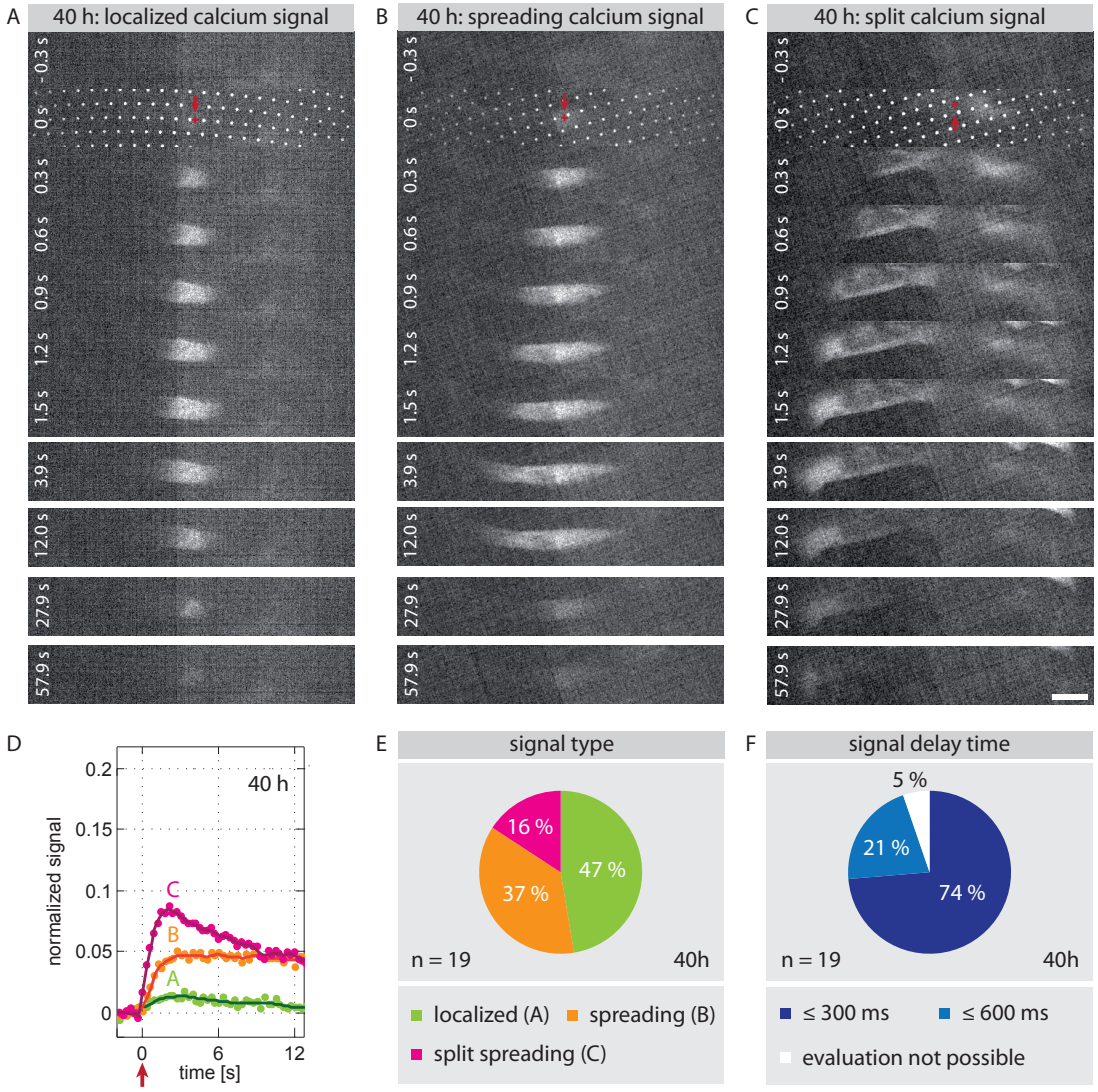

Figure 4.17.: Optically induced calcium signals in early abdominal muscles at 40 h APF. A-C| Time sequences of typical GCaMP6f signals in abdominal muscles of [☿ UAS-GCaMP6f x ♂ Mef2-GAL4, UAS-Cherry-Gma] responding to optical severing (1 point, 1 pulse/point) at 40 h APF. Time refers to frame of cut (0 s), readily identifiable through the pattern of points of the SD caused by additional fluorescence due to cutting. Red arrows point at position of cut (crosses). A| Localized and weak signal. B| Signal spreading throughout most of the muscle length. C| Split, widely spreading calcium signal. Signals originate from target point and start in the frame of stimulation. Signal duration is variable. Scale bar 10 µm, anterior left, dorsal up. D| Visualization of intensity evolution of areas shown in (A-C): A<B<C. Signal was normalized on mean intensity before cut, which was set to zero, and corrected for background bleaching. E| Distribution of signal types shown in (A-C). Different laser intensities were used to collect examples of all types. F| Delay time between cut and GCaMP6f signal onset. Full circles (E-F) refer to total number of induced GCaMP6f signals ($n = 19$).

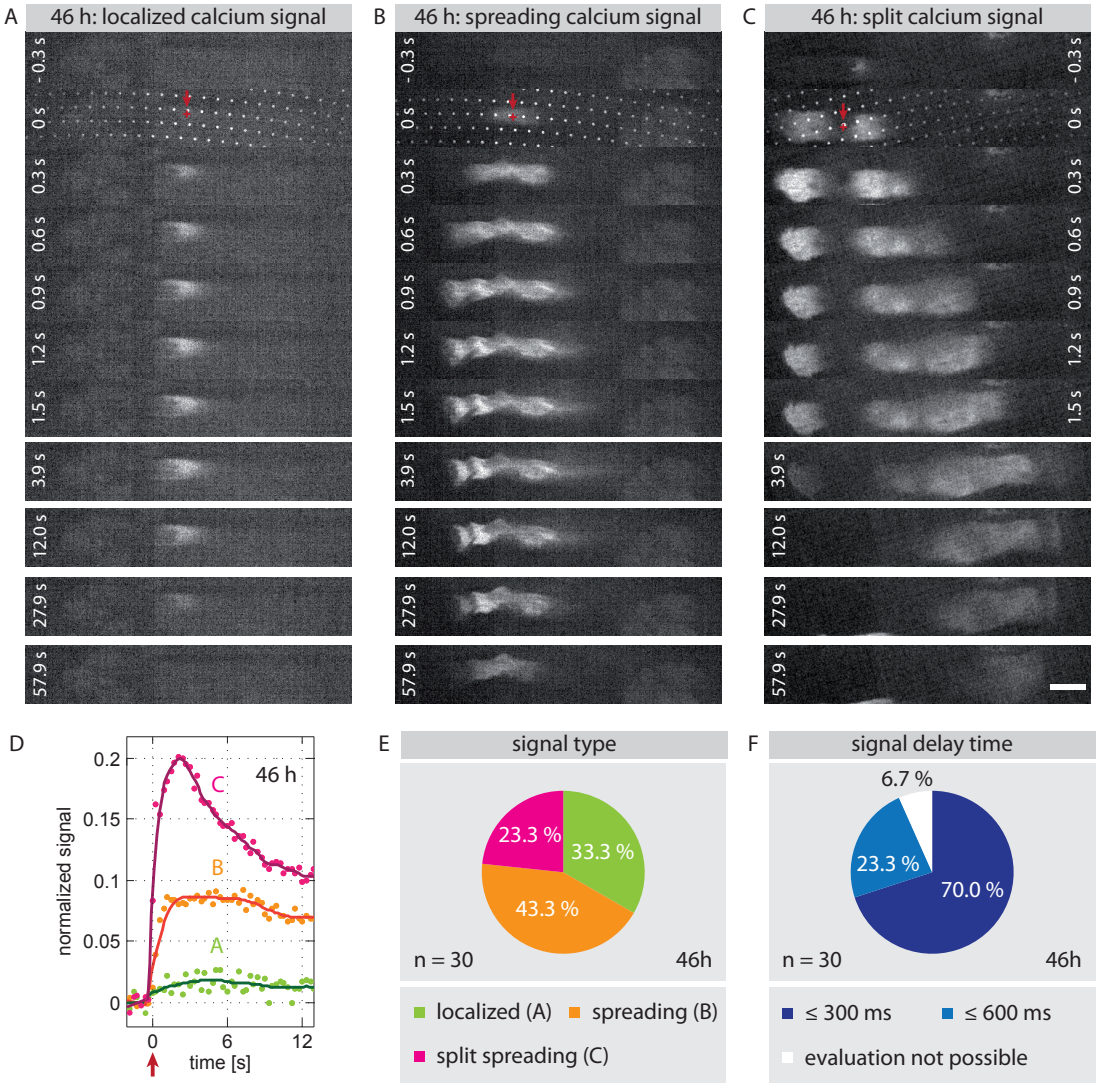

Figure 4.18.: Optically induced calcium signals in late pre-sarcomeric abdominal muscles at 46 h APF. A-C| Time sequences of typical GCaMP6f signals in abdominal muscles of [♀ UAS-GCaMP6f x ♂ Mef2-GAL4, UAS-Cherry-Gma] responding to optical severing (1 point, 1 pulse/point) at 46 h APF. Time refers to frame of cut (0 s), readily identifiable through the pattern of points of the SD caused by additional fluorescence due to cutting. Red arrows point at position of cut (cross). A| Localized and weak signal. B| Signal spreading throughout most of the muscle length, clearly showing *induced contraction* (seen from undulations and movement of attachment site). C| Split, widely spreading calcium signal. Signals originate from target point and start in the frame of stimulation. Signal duration is variable. Scale bar 10 µm, anterior left, dorsal up. D| Visualization of intensity evolution of areas shown in (A-C): A<B<C. Signal was normalized on mean intensity before cut, which was set to zero, and corrected for background bleaching. E| Distribution of signal types (shown in A-C). F| Delay time between cut and GCaMP6f signal onset. Full circles (E-F) refer to total number of induced GCaMP6f signals ($n = 30$).

ferent intensities (A<B<C).
The distribution of observed signals among the different signal types (A-C) is shown in figs. 4.17 E and 4.18 E. The ratio of spreading/split spreading target signals to localized target signals was different at the two investigated time points. At 46 h, the ratio was approx. 2/3 spreading and split spreading signals to 1/3 of localized signals (≅ ratio 2). At 40 h APF, the ratio was approx. 1/2 spreading and split spreading signals to 1/2 of localized signals (≅ ratio 1). Importantly, this distribution reflects the intention of the experiment to span the phase space of signal types by using more or less laser power during optical stimulation. Hence, it is not a system inherent response type analysis.
As shown in figs. 4.17 F and fig. 4.18 F most signals were first confirmed in the frame that also contained stimulation (74 % and 70 % of signals at 40 h and 46 h, respectively). This corresponds to a signal delay time of less than 300 ms with respect to optical stimulation. The remaining signals occurred in the first frame after the stimulation frame (40 h: 21 % and 46 h: 23 % of signals), corresponding to a signal delay time smaller than 600 ms. Despite their differences, signals always originated from the point of stimulation.
Bleeding of fluorophores from the muscle into the surrounding area was only detected, when the muscle was badly injured, such as the muscle shown in fig. 4.18 C. A rupture of the muscle membrane may, however, not be completely excluded for smaller signals. Small leakages might be undetectable due to a poor contrast.

Signal induction at 40 h APF Reliability of Ca^{2+} influx as inferred from the GCaMP6f signal upon optical stimulation in pupae at 40 h APF is shown in fig. 4.19. All $n = 19$ optical stimulations in sixteen 40 h old pupae induced GCaMP6f signals. Hence, Ca^{2+} could be reliably induced at 40 h APF.

Signal induction at 46 h APF With 91 % the majority of all $n = 33$ stimulation attempts induced a GCaMP6f signal (see fig. 4.19). In 43 % of all induced GCaMP6f signals (39 % of all evaluated cuts) both, *induced contraction* and a GCaMP6f signal were simultaneously observed upon stimulation. This is a direct verification of simultaneous occurrence of GCaMP6f (and hence Ca^{2+}) signal and *induced contraction*. 17 % of observed signals were not accompanied by *induced contraction* (only two of the five cases showed a spreading signal). In 36 % of all evaluated cuts a signal was observed but *induced contraction* could not be evaluated due to different reasons already mentioned above: Part of the muscle was either out of focus, without enough fluorescent signal, or the fluorescent signal appeared too late in the respective part of the muscle. Accordingly only 9 % of all cases did not show a GCaMP6f signal. In none of the muscles, that did not show a GCaMP6f signal upon stimulation (9 % of stimulation attempts), *induced contraction* was observed (seen from baseline fluorescence of muscles).
In summary, Ca^{2+} could be reliably induced in dorsal abdominal muscles of 46 h old pupae. No cases of *induced contraction* without Ca^{2+} induction were observed. Hence, Ca^{2+} influx upon optical stimulation is a very likely candidate for the ultimate triggering of *induced contraction*.

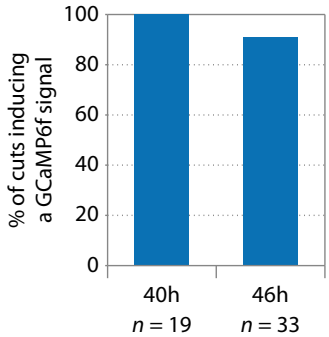

Figure 4.19.: Calcium in dorsal abdominal muscles during optical stimulation of [☿ UAS-GCaMP6f x ♂ Mef2-GAL4, UAS-Cherry-Gma] and [☿ UAS-GCaMP6f x ♂ Mef2-GAL4, UAS-CD8-Cherry] pupae at 40 h or 46 h APF. Bars show percentage of stimulation attempts in pupae of respective age, that induced a GCaMP6f signal in abdominal target muscles.

4.2.3.3. Ca^{2+} in neighboring muscles

The previous subsection presented the results on Ca^{2+} in target muscles. However, neighboring muscles (other dorsal abdominal muscles of the same abdominal segment as the target muscle; in the following referred to as neighbors) often showed fluorescence signals after target muscle (referred to as target) stimulation. Neighbor signals showed a variety of morphologies, ranging from small localized signals in a single neighbor to muscle spanning cascades, where one muscle after the other fluoresced. In the following an analysis of neighbor signal occurrence is given. Due to the variety of neighbor signals, signal counting did not account for different neighbor signal morphologies.
Neighbor signals occurred only in combination with target signals. Neighbor signals were not observed without target signals (3 cases at 46 h APF). Among those target muscles that showed a GCaMP6f signal upon optical stimulation (40 h: $n = 19$; 46 h: $n = 30$), the percentage of cases with additional signals in neighbors differed for developmental time points (see fig. 4.20). At 40 h APF neighbor signals were only observed for 26 % of targets, whereas in the group of 46 h old targets neighbor signals were confirmed for 60 % of target signals.

This result might reflect a time point property and/or a dependence of neighbor signals on disturbance, which is enhanced at 46 h due to induced contraction. Arguments for or against these possibilities may be inferred from a correlation of neighbor signals with other observables of the system: A correlation of neighbor signals with the corresponding target signal size revealed a clear preponderance of spreading or split spreading signals as compared to localized target signals (see fig. 4.21 A-B). This finding by itself indicates that induction of neighbor signals might depend on target signal size. However, further conclusions concerning the higher percentage of neighbor signals at 46 h may only be drawn in the context of the occurrence of different target signal types themselves. As mentioned in the previous subsection and indicated in figs. 4.17 E and 4.18 E the ratio of (split) spread-

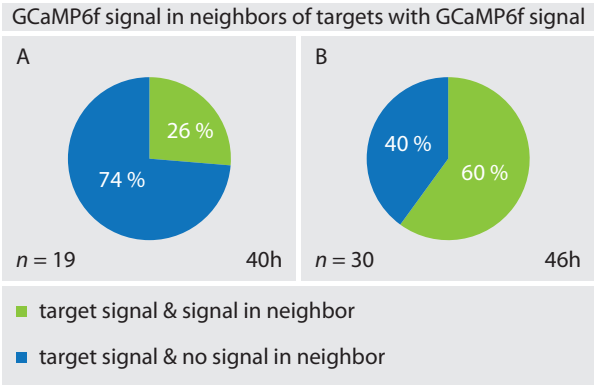

Figure 4.20.: Calcium in neighboring muscles of targets in 40 h or 46 h old, optically stimulated pupae as inferred from GCaMP6f signals. Full circle represents all cases with induced GCaMP6f signal in the target. A| $n = 19$, 40 h APF. B| $n = 30$, 46 h APF. Neighbor signals were observed at both developmental time points.

ing target signals to localized target signals is larger at 46 h (approx. 2 as compared to approx. 1 at 40 h). Hence, at 46 h the percentage of strong target signals is higher (67 % as opposed to 53 % at 40 h). Therefore, the difference in neighbor signal occurrence as shown in fig. 4.20 (60 % at 46 h as opposed to 26 % at 40 h) can, at least partially, be explained by a neighbor signal dependence on target signal strength. However, the difference in the percentage of large target signals that resulted in neighbor signals could indeed be a time point property.
However, a dependence on mechanical disturbance is also conceivable. It would also contribute to an increased observation of neighbor signals at 46 h APF, because an *induced contraction* of the target might provide the required mechanical stimulation. To underpin this argument, concomitant bubble formation was analyzed. Interestingly, bubble formation was more often (percentaged) observed with neighbor signals at 40 h APF than with neighbor signals at 46 h APF (see fig. 4.21 C-D). Nevertheless, this could still indicate that mechanical disturbance is indeed a requirement for neighboring signals: At 46 h, mechanical disturbance might be mainly induced by *induced contraction* of the target. This is not possible at 40 h APF, where instead bubble formation could play a more important role.

4.2.4. Dorsal abdominal muscle structure

For further interpretations of the results regarding dorsal abdominal muscles, it is essential to place them in the context of structural changes during muscle development. However, neither a detailed knowledge of the developmental evolution of sarcomeric structures nor a complete picture of its regulation exists. In order to shed light on the structural stages in abdominal muscle development and to compare it to muscle functionality, dorsal abdominal muscle structure was investigated by our collaboration partners Manuela Weitkunat and Frank Schnorrer (Max-Planck-Institute for Biochemistry in Martinsried, Germany). This subsection summarizes their results.

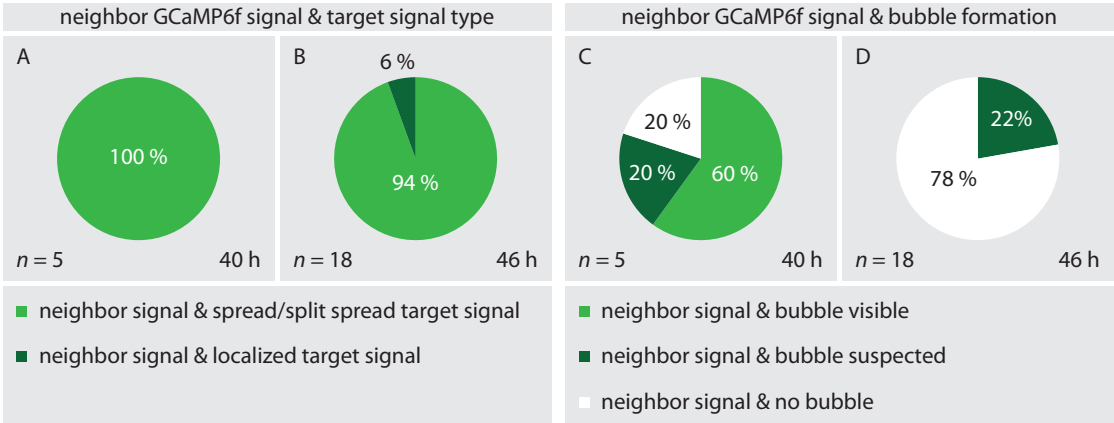

Figure 4.21.: Origin of Ca^{2+} flux in neighboring muscles of targets in 40 h (A, C) or 46 h (B, D) old, optically stimulated pupae as revealed from GCaMP6f signals. A-B| Classification of target signals, which were accompanied by neighbor signals. The majority of the corresponding target signals were spreading/split spreading. (For a classification of different target signal types see text and figs. 4.17 and 4.18.) C-D| Neighbor signals with concomitant bubble formation. Full circles refer to all $n = 5$ (40 h) or $n = 18$ (46 h) neighbor signals.

M. Weitkunat manually dissected, fluorescently stained, and imaged (spinning disc confocal microscopy) dorsal abdominal muscles in [wt^-] pupae of different age APF as previously described [93]. Figure 4.22 shows a synopsis of abdominal muscles, which were stained for actin and mhc. The evolution of the sarcomeric structure from a rather disordered appearance at 36 h APF to their almost final ordered structure at 72 h APF is clearly visible. At 36 h APF actin is already organized in a patchy filamentous pattern, which is slightly more pronounced at 40 h. Mhc, in contrast, is seen as rather homogeneously distributed dots, which are not yet associated with the filamentous actin structure. At 46 h the myosin dots start to associate with the increasingly parallel but still laterally separated actin fibers (immature myofibrils). At 52 h in addition to the fibrillar organization alternating stripes of mhc and actin are visible and a lateral alignment of myofibrils has started to evolve. By 72 h APF the sarcomeric pattern of actin and myosin resembles very much the final muscle pattern right before eclosion. Hence, a structural switch from lateral and sarcomeric disorder to lateral and sarcomeric order between 46 h and 52 h APF was observed.

4.3. Summary

Experiments in dorsal-longitudinal (indirect flight) muscles (DLMs) were carried out in order to extend the knowledge about tension in this muscle type. Optical severing of DLM tendons (complete cuts) was performed in pupae aged to 30 h APF. At this time point muscle-tendon attachment maturation and muscle compaction take place (see section 4.1, 4.1.1). Neither the exact time point nor this developmental stage have been investigated so far. A manual, quantitative analysis of tendon tip velocities revealed a retraction of the cut tips along the tendon axis away from the cut, demonstrating the presence of tension.

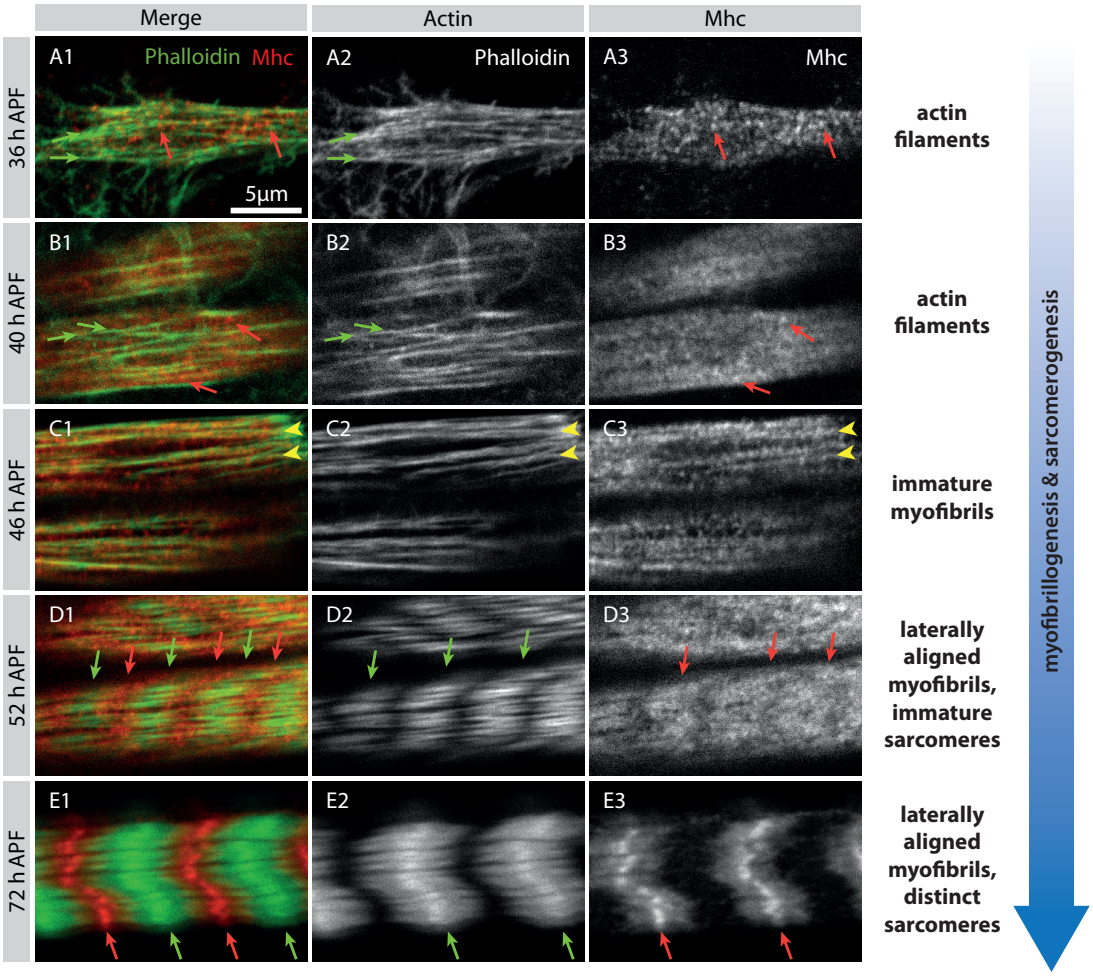

Figure 4.22.: Actin and myosin in dorsal abdominal muscles of [w$^-$] pupae at 36 h (A), 40 h (B), 46 h (C), 52 h (D), and 72 h (E) APF. The first column is a merge of the second and third column, which show actin (green, phalloidin staining) and myosin (red, mhc antibody staining), respectively. Red and green arrows point at prominent structures of mhc (red) and actin (red). Yellow arrowheads indicate parallel but laterally separated immature myofibrils. Although immature myofibrils are already present at 46 h APF, a sarcomeric pattern and lateral alignment only start to evolve later (52 h). Images (A1-E3) by M. Weitkunat.

The mean value of initial tendon tip velocity along the tendon axis away from the cut was found to be $v_{\text{parallel}}(0) = 138 \pm 112\,\mu\text{m/min}$.
As the sub-cellular components and the tissues (muscles, tendons, or epidermis) that are responsible for tension built up still need to be confirmed, two cytoskeletal components were investigated, microtubules in section 4.1.2 and myosin in section 4.1.3.
Optical DLM microtubule severing on the NDD was possible without destroying muscle integrity. The microtubule tip velocity after cutting was estimated to be between 5 µm/min and 64 µm/min, which is in the range of microtubule depolymerization rates [10, 69, 88]. This finding impeded tension verification or falsification and suggested depolymerization as the driving mechanism behind microtubule tip retraction.
In order to investigate the role of myosin for tension creation, a new mounting technique for the application of blebbistatin solutions was established. Application of blebbistatin in a solution of DMSO and ddH_2O was tested in order to find a concentration regime where blebbistatin visibly causes a muscle defect, while DMSO doesn't cause significant effects. DMSO was found to diffuse at least as deep into the pupae as DLMs and to cause visible defects in DLMs, specifically the inhibition of transport machineries as well as the inhibition of muscle compaction and accordingly tendon elongation. However, a visible effect that could exclusively be assigned to blebbistatin was not found.

In order to clarify, whether tension during muscle development is a unique feature of DLMs or a general mechanism, dorsal abdominal muscles were investigated at four different developmental time points (section 4.2). Complete rupture or partial rupture (micro-lesions) with subsequent relaxation upon optical severing of dorsal abdominal muscles at 36 h or 40 h APF revealed the presence of tension in the system. At later time points, 46 h and 52 h APF, tension could neither be verified nor excluded due to a contractile muscle response to optical severing, which is referred to as *induced contraction*. *Induced contraction* also occurred with (almost) invisible destruction of labeled cytoskeletal components in the muscle (nano-lesions). It is unclear, whether *induced contraction* is an active or a passive process. In some cases of *induced contraction* in target muscles, neighboring muscles showed autonomous contractile movement. This correlated with an increased severity of target muscle disturbance.
Investigations of calcium ions (Ca^{2+}) gave interesting insights into muscle functionality. Ca^{2+} was visualized via the cytosolic Ca^{2+} sensor GCaMP6f. Ca^{2+} influx into the cytosol occurred upon optical stimulation at 40 h as well as 46 h. Most Ca^{2+} signals appeared faster than the exposure time of one frame (300 ms). Signals originated at the site of optical stimulation. Their duration, spread and intensity was heterogeneous but, apart from concomitant *induced contraction*, it could not be distinguished according to the age of the pupae. Considering possible origins of neighbor Ca^{2+} stimulation, it seems likely, that a large target signal and/or mechanical disturbance cause Ca^{2+} signals in neighbors.
Attachments to tendons did not suffer from *induced contractions* as seen from direct observation of epidermal cells around muscle tendon attachments, which followed the contractile movement of the muscles.
Observation of undisturbed muscle behavior revealed the occurrence of muscle inherent contraction processes, which are referred to as auto-twitching. The probability of auto-twitching at 46 h APF is not zero but very low and increases slightly at 52 h. This indicates stable attachments as well as the capability of muscles to actively, though rarely, contract as early as 46 h APF. Turning back to the behavior of neighbors, this finding rendered

it very unlikely that neighbor behavior is an autonomous behavior and not provoked by optical stimulation and subsequent processes in the pupa.
The investigation of internal abdominal muscle structure by our collaboration partners M. Weitkunat and F. Schnorrer revealed a pronounced structural switch between 46 h and 52 h APF. Muscles change from a rather disordered state without sarcomeric patterning or lateral order to an ordered state with lateral alignment of pre-myofibrils and an emerging sarcomeric structure.

The experiments, which were performed in the course of this thesis and which were presented in this chapter, gave interesting new insights into adult muscle development in *Drosophila*. An interpretation of the results in their full bandwidth is presented in the next chapter.

5. Discussion and outlook

The goal of this thesis was to gain new insights into adult muscle development in the model system *Drosophila melanogaster*. Despite extensive investigations in this field, several central questions are yet to be answered. This thesis focused on tension and contraction as contributors in muscle development. In the following, the results, which were presented in the previous chapters, are discussed and an outlook on continuative experiments is given. The publication of parts of this chapter is in preparation.

Tension is present during DLM compaction The presence of tension during development of dorsal-longitudinal (indirect flight) muscles (DLMs) and their tendons has been shown previously for developmental stages between 13 h and 22 h APF by means of optical severing experiments [92]. Work of this thesis confirmed tension in the DLM tendon system at 30 h APF, the stage of attachment maturation, muscle compaction and myofibrillogenesis. First, this strengthens the observation of Weitkunat *et al.* that tension is required for myofibrillogenesis. Second, it extends the period with tension from a 10 h window to a 18 h window, indicating that tension might be non-transient and could remain throughout DLM development. Optical severing experiments at later time points, during muscle elongation and tendon shortening, are necessary to confirm this expectation.

Tension evolution in the myotendious system of DLMs In order to extrapolate tension evolution to later developmental stages, a comparison of the characteristic values of the recoil behavior, specifically the initial recoil velocity of the cut tendon, is necessary. However, due to different data analysis techniques it is difficult to place the results in context of previous results from Weitkunat *et al.* ([92]). The result from the manual tip velocity analysis presented in this thesis is in general larger than the result from a velocity analysis of a certain area around the tip as performed by Weitkunat *et al.* because the cut edges are the part of the target that is moving fastest (if a simple elastic material is assumed). Hence, a comparison of initial recoil velocities is restricted to the conclusion that recoil velocities are of the same order of magnitude.

Tension is a universal feature in *Drosophila* adult muscle development In addition to its role in DLM formation, tension was found to be present in developing dorsal abdominal muscles at 36 h and 40 h APF. These muscles belong to the class of tubular muscles, while DLMs are fibrillar muscles (see section 3.2). Hence, the presence of tension was confirmed as a universal feature in adult muscle development in fibrillar and tubular *Drosophila* muscles. Fibrillar muscles have only been found in insects [38], but tubular muscles are considered to be closer to vertebrate skeletal muscles [35, 77], suggesting a contribution of tension not only in other insect species but also in vertebrates and thus humans.

Microtubules and myosin II in DLMs The key molecules, which contribute to tension formation in DLMs and dorsal abdominal muscles, are not known. Cellular proteins that are known for their participation in cell motility are likely to also contribute to tension formation. Most promising candidates are cytoskeletal components and motor proteins, first and foremost actomyosin networks. Therefore, myosin II and microtubules in the DLM system were investigated.
Optical severing of DLM microtubules was performed in order to investigate, whether tension is present in the DLM microtubule system. Experiments revealed retraction velocities of cut edges that were in the range of microtubule depolymerization. This strongly suggests that the retraction of cut microtubule edges was caused by a depolymerization process. However, a contribution of tension or even an active transport can neither be verified nor excluded. Further experiments are required to clarify the situation. One major difficulty in microtubule experiments was the high density of microtubule bundles, which resulted in poor contrast. Analogous experiments in abdominal muscles are an obvious option. Due to the smaller size of abdominal muscles, microtubule bundles might present a better contrast, thus facilitating data evaluation. Moreover, the measurement of DLM tendon recoil velocities upon optical severing in genotypes with altered microtubule systems, for instance different expression levels and different polymerization or binding kinetics, are interesting possibilities to gain more insights into tension creation.
In order to investigate the contribution of myosin II to tension formation during DLM development, the use of blebbistatin (diluted in DMSO and water) was tested. A visible effect on the DLM-tendon system was found for DMSO but not for blebbistatin alone. Several explanations for this finding are possible: First, DMSO but not blebbistatin could reach the target. Second, blebbistatin could reach the target but cause an effect that is not visible (either in the used genotype or in general). Third, blebbistatin could reach the target, but have no inhibiting effect on *Drosophila* myosin II: Blebbistatin was found to inhibit certain myosins in certain cells of certain species [79], but controversial findings were made on its impact on *Drosophila* cells, for instance the capability to stop *Drosophila* heart beating [16, 43, 79]. Here, optical severing experiments provide means for further investigations. If the retraction velocity of cut DLM tendon tips depends on blebbistatin but not DMSO concentration, (which will only happen, if myosin II cannot be substituted by other motor proteins,) then two questions would be answered. It would proof the contribution of myosin to tension formation as well as the inhibition of myosin by blebbistatin. An alternative for the usage of blebbistatin are genetically encoded alterations in myosin function. However, due to the universal occurrence of myosin, a manipulation is difficult and an adequate, viable yet significantly disturbed genotype remains to be found.

***Induced contraction* in dorsal abdominal muscles can be an active or a passive process** Optical severing of dorsal abdominal muscles at later developmental time points (46 h and 52 h APF) caused *induced contraction*. These contraction processes resembled normal muscle contraction during auto-twitching in their contraction morphology, suggesting an active process on the basis of actomyosin contraction. However, *induced contraction* was often caused by complete rupture or micro-lesions, which caused in part severe and potentially destabilizing structural damages in the muscle. Therefore, a passive contraction mechanism, where the muscle behaves like a passive visco-elastic material, is also conceivable. In the following, both scenarios with supporting arguments are presented and discussed.

Both mechanisms, active as well as passive, are theoretically capable of reproducing the behavior of all observed regions of interest during *induced contraction*. In the case of complete rupture, which is the clearest situation, the behavior of stimulated muscles was the following:

- a stable situation is disturbed by a first optical lesion
- contractile movement of the muscle: attachment sites move towards each other and the muscle undulates
- a continuous rupture process or a second optical severing process results in a complete separation of the muscle into two pieces (not necessarily of the same size)
- attachments move back into or beyond their initial position, cut edges and structures along the muscle move away from the rupture site

A scheme of both models for *induced contraction* is shown in figs. 5.1 A (passive scenario) and B (active scenario). In the passive scenario the muscle as well as surrounding tissues, specifically tendons, epidermis and extracellular matrix (ECM), are represented by (passive) Hookean springs, which are connected at the attachment sites (as). The system is stable, microtubules (MTs) form a scaffold that spans the muscle and keeps it in a stretched state by pushing the muscle ends apart from the inside. ECM/tendon/epidermis springs may or may not be pre-stressed. In a first step (step 1), the MT scaffold gets destroyed by a first optical severing (cut 1), whereas muscle integrity remains intact. Step 2, representing *induced contraction* follows: With appropriate values for the spring constants, the muscle spring applies more force on the attachment sites than do the tendon/ECM/epidermis springs. This causes a movement of attachment sites (as) towards the center until the spring system has reached the new force equilibrium (without MTs). The shortening of the distance between the attachment sites (as) results in undulations of the muscle (for clarity not drawn in sketch). Now a second severing (cut 2) causes the complete rupture of the muscle. (This may alternatively be caused by a continued sequential rupture.) All springs relax back into their equilibrium length (step 3). If tendon/ECM/epidermis springs were not pre-stressed in step 1, attachment points move back into their initial position (step 3'). If tendon/ECM/epidermis springs were pre-stressed, attachments move beyond their initial position (step 3"). The additional movement in step 3" as compared to step 3' results from the relaxation and thus shortening of tendon/ECM/epidermis springs. This passive model is a conceivable scenario that reproduces all characteristics complete rupture after induced contraction, as summarized above.
In the active scenario the muscle is not a simple passive visco-elastic material but can reorganize and actively generate force in its actomyosin network (represented as red network). Before optical severing the system is in a stable state. Tendons/ECM/epidermis, which are still acting as a simple visco-elastic material, may or may not be pre-stressed. Optical severing (cut 1) is performed (step 1). It does not cause a complete rupture of the muscle but sufficiently disturbs the actomyosin system to perform an active contraction process (step 2). This results in *induced contraction* and attachment sites (as) move towards the center.The shortening of the distance between the attachment sites (as) results in undulations of the muscle (for clarity not drawn in sketch). Thereby, tendons/ECM/epidermis are (further) stretched. Then, a complete disruption of the muscle (cut 2) is performed

(alternatively caused by a continued sequential rupture). The movement of attachment sites away from the cut is equivalent to the passive scenario (step 3' without pre-stressed tendon/ECM/epidermis springs, step 3" with pre-stressed tendon/ECM/epidermis springs) with the difference that now an active contraction process of the separated muscle pieces is superimposed on the passive relaxation movement of the cut edges. Hence, also an active scenario can describe *induced contraction*.
Notably, these models can also be used for the case of micro-lesions, where muscles are only partially cut. In this case, the structures in fig. 5.1 do not represent the whole muscle but functional subunits that get disrupted during optical severing. The causes and consequences for the different regions of interest are less pronounced but do otherwise stay the same.
Both models presented above, the active one as well as the passive one, adequately reproduce the behavior of optically stimulated *induced contraction*. Hence, active as well as passive processes have to be considered as the underlying mechanism for *induced contraction*.

A distinction of active and passive contraction processes is not straight forward. Both, passive visco-elastic as well as active visco-elastic scenarios, can be modeled with Hookean spring systems [45, 67, 68] and will thus result in an exponential decay of the retraction velocity of cut edges. Moreover, active and passive processes could occur individually or in combination. Therefore, in the simplest cases, the recoil velocity will either show a single exponential decay (if exactly one mechanism applies) or a double exponential decay (if there are active and passive contributions). A distinction is only possible if active and passive contributions differ substantially in their amount and time scales. However, due to the diversity of retraction morpholgies a quantitative recoil velocity analysis is difficult and not expected to result in adequate data. Hence, this parameter could not be used to reveal the underlying process. Instead, indirect arguments needed to be inferred from observations of calcium ions and natural muscle behavior during *induced contraction*, as will be discussed in the following.

Optical severing induces release into and subsequent clearance of Ca^{2+} out of the muscle cytosol By causing induced contraction in 46 h old dorsal abdominal muscles with cytosolically expressed GCaMP6f, a fluorescent artificial Ca^{2+} reporter, a concomitant increase of the cytosolic Ca^{2+} concentration was revealed. In most cases, a subsequent decrease of the signal was observed. Interestingly, Ca^{2+} signals were also observed upon optical stimulation of abdominal muscles at 40 h APF, a time point, when induced contraction was not yet possible. Duration, spread and intensity of the observed signals varied in different pupae but, apart from undulations due to *induced contraction*, not for different developmental time points.
These findings demonstrate, that the machinery for Ca^{2+} regulation are present before the muscles are capable of contractions. Moreover, the finding of Ca^{2+} participating in the optical severing process is a convincing indicator for an active process behind *induced contractions*, resembling normal muscle contraction.
The origin of the Ca^{2+} influx is supposedly an intra-cellular Ca^{2+} storage, the sarcoplasmic reticulum or its precursors, which are perforated by the optical severing process. Depending on how long the leakage persists, the Ca^{2+} concentration and thus the signal remain because ions can constantly escape from the storage into the cytosol and maintain an el-

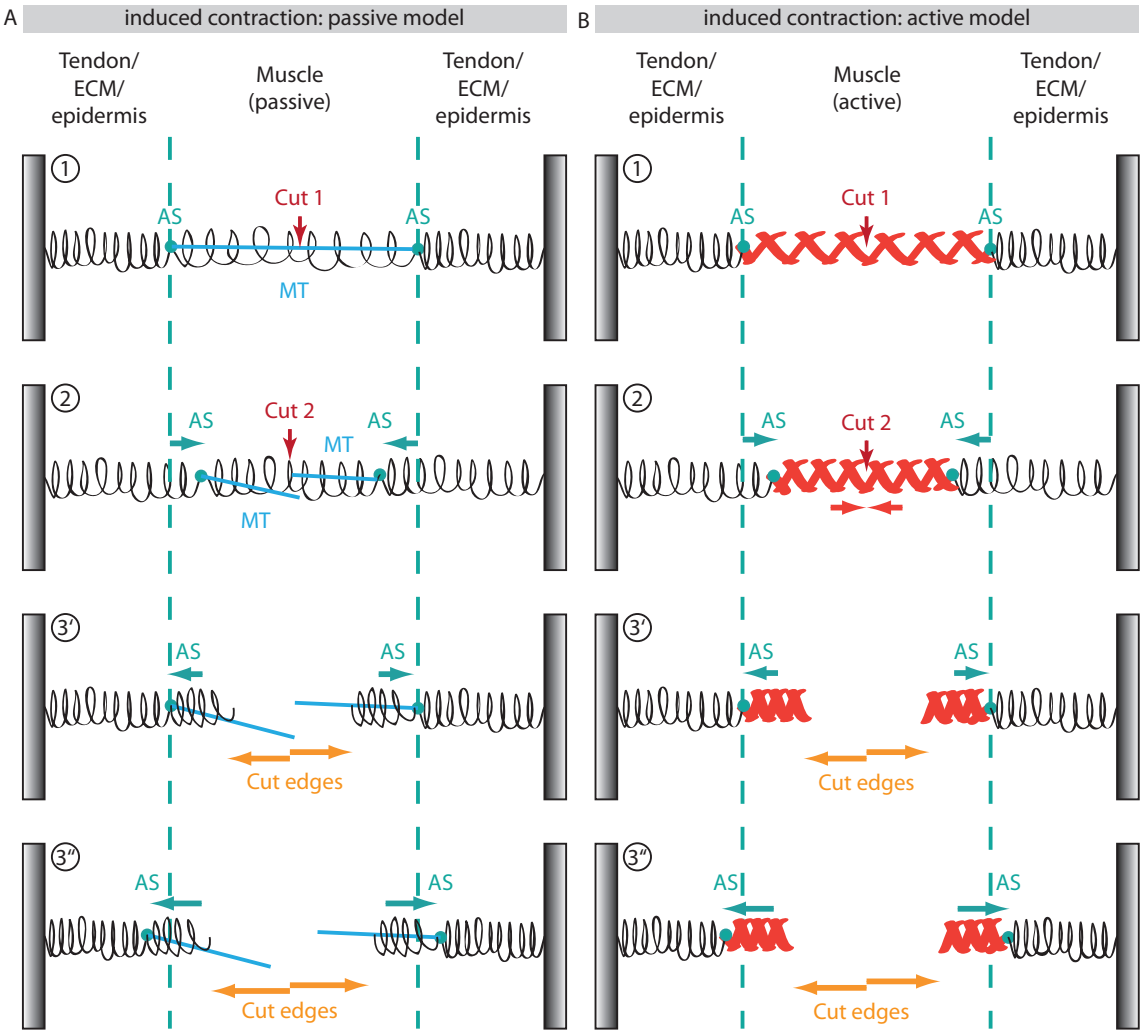

Figure 5.1.: Scheme of models for *induced contraction*. A| Passive scenario. B| Active scenario. Passive components (tendons/ECM, muscle) are represented as Hookean springs (black). The active muscle is represented as a red network. Microtubules (MT, blue lines), attachment points (as). Dashed blue-green lines guide eyes to initial positions of (as). Arrows indicate movement of (as) (blue-green) and cut edges (orange). For simplicity, movement of structures along the muscle are not indicated. Dark red arrow points at cutting position. Light red arrows indicate active contraction.

evated concentration. Nevertheless, Ca^{2+} is obviously pumped out of the cytosol as seen from transient signals.
An influx of Ca^{2+} from the ECM is also conceivable. Such a flux would be possible on the basis of a concentration gradient between cytosol and extra-cellular space [55]. However, two facts argue against this scenario. First, the laser was focused on a target inside the muscle, which reduced the probability, that the muscle membrane was ruptured. Second, if a leakage in the plasma membrane was the cause of Ca^{2+} influx, GCaMP6f molecules would be expected to escape into the extra-cellular space. Such a bleeding of GCaMP6f fluorophores was only observed for badly injured muscles but not for small lesions. This renders an extra-cellular Ca^{2+} origin unlikely.

***Induced contraction* and Ca^{2+} in neighboring muscles suggest a connectivity among individual dorsal abdominal muscles** Ca^{2+} signals upon induced contraction in target muscles were often accompanied by contractions and Ca^{2+} signals in neighboring muscles of the same segment (muscles of other segments were not observed). The morphology of neighbor contraction as well as the occurrence of Ca^{2+} signals in neighbors strongly suggest an active mechanism. A coincidental independent neighbor twitching is excluded on the basis of the very low auto-twitching probability at the investigated time points. Responding neighbors were often seen at a significant distance to the target, rendering a direct stimulation via optical severing unlikely. Hence, the active response of neighbors to target stimulation suggests a connectivity among dorsal abdominal muscles of the same segment. The correlation of events in neighbors with larger lesions supports three hypotheses. First, neighbor muscle activity might be a reflex of the animal in response to signals in sensory neurons. Second, muscles might be mechanically activatable. However, this second scenario is probably not the exclusive mechanism behind neighbor activity: Although stretch-activation has been found to be a mechanism of varying importance depending on the muscle type [24], it still requires increased Ca^{2+} levels, which has to be triggered somehow. In functional muscles this increased Ca^{2+} level is triggered by neuronal stimulation (see section 3). It is therefore likely that the suspected connectivity is based on a transduction of action potentials, either directly via connected plasma membranes, or indirectly via neurons. Such a connectivity would support orchestrated muscle contractions.
The investigations of these hypotheses require extensive experiments. In a first step Ca^{2+} signals and contraction could be induced in pupae with disturbed neuronal signaling. This would reveal the role of neurons.

Structure and functionality: *Induced contraction* and auto-twitching suggest the requirement of contractions for sarcomere formation The observation of *induced contraction* at 46 h and 52 h APF but not at 36 h and 40 h APF has major implications. First, it suggests a structural connection and cooperativeness of the whole muscle cell. Second, it proofs the ability of dorsal abdominal muscles, to contract as early as 46 h APF. This was not entirely clear from the observation of auto-twitching events in pupae of 46 h, 48 h, and 52 h APF. Observation of auto-twitching revealed that muscles did twitch at such early time points, but the probability of such a muscle contraction was very small. In contrast, the induction of a contraction by means of optical stimulation was very robust, indicating a general capability of these muscles to contract at 46 h APF and later.

This observation is particularly noteworthy in the context of concomitant structural changes in the muscle. Interestingly, M. Weitkunat observed that muscles at 46 h contain immature myofibrils, but a striated pattern had not yet developed. A significant increase in striation and lateral alignment was found to occur between 46 h and 52 h APF. Hence, the switch in function from non-contractility to contractility between 40 h and 46 h as seen from *induced contractions* (this thesis) precedes the structural switch from a laterally disordered and non-striated to a laterally ordered and striated pattern between 46 h and 52 h APF. From this finding we conclude that contractions might support or even be required for sarcomere formation. This is supported by the observation of auto-twitching as early as 46 h APF. Moreover, findings in skeletal muscle cell cultures also point in this direction. In rat myotubes, sarcomeric order is only established and/or maintained in contracting myotubes but not in passively stretched cells in which contractile activity is chemically inhibited [20]. Combining this finding with the results on dorsal abdominal muscles in this thesis, different pathways for sarcomerogenesis are conceivable. First, repeated tension formation with subsequent tension release could be required (as opposed to permanent tension). In a second scenario, contractile activity is a by-product of other necessary signaling pathways. It is conceivable that for instance Ca^{2+} transients are the ultimately required signals and not the mechanical stimulus of the contractions. Finaly, a combination of both scenarios is also possible.
To test these hypotheses, several different experiments may be performed. If muscle contraction triggers sarcomere patterning an increased contraction rate in abdominal muscles should lead to a preponed sarcomere pattern. An increased contraction rate could be achieved by repeated stimulation of *induced contraction* via optical severing on the NDD. However, this method hazards the possibility of additional undesired structural damage, that might in turn delay sarcomere formation. An alternative are pupae with exogenous light-gated cation channels, such as channelrhodopsins [83, 95]. Here, a completely non-invasive induction of muscle-contraction as a response to light-induced Ca^{2+} influx could be possible. A sufficiently high rate of light-induced contractions could lead to a preponed appearance of the sarcomeric pattern and confirm the presented hypothesis. Complementary, a genotype with reduced auto-twitching should lead to a delayed sarcomeric pattern. An interesting approach are pupae, where neurotransmission is inhibited after a temperature shift shortly before the start of the experiment. This is important for the reduction of artifacts, because nervous system and muscles rely on each other for proper development (see section 3). The disturbed neurotransmission should inhibit auto-twitching and cause a delayed or absent sarcomere formation. Both approaches should be used in order to best possibly verify or falsify the hypothesis of sarcomere formation upon muscle contraction.

Developmental roles of tension and contractile activity in early dorsal abdominal muscles As mentioned in the previous paragraph, it has been found in cell culture experiments that contractile activity was the crucial factor for sarcomere formation and maintenance, while passive tension alone only leads to an alignment of myotubes, but it is not sufficient to induce sarcomere formation or maintenance [20]. Nevertheless, tension has been found to be essential for sarcomere structures in DLM myofibrillogenesis [92]. Moreover, results in this thesis verified passive tension to be present during the early phases of dorsal abdominal muscle formation at 36 h and 40 h APF. At first glance, these observations appear to be contradictory. However, they may still be unified in a conceivable scenario for abdominal

muscles: Passive tension could play a crucial role during the early stages of muscle formation. It could help to align structures in the early myotube, sarcomere building blocks as well as immature myofibrils, which still lack their sarcomeric structures at this stage. After this pre-organization, contractile activity becomes important to further organize the building blocks into sarcomeres.

Summary The results presented in this thesis gave exciting new insights into *Drosophila* adult muscle development. Tension was found to be a universal cue in muscle development, independent of muscle type. Hints for a non-transient role of tension in DLMs were found. Abdominal muscles were optically stimulated to contract (*induced contraction*). Due to the observation of concomitant Ca^{2+} signals in the cytosol, *induced contraction* was classified as an active process resembling endogenous muscle contractions. In abdominal muscles the Ca^{2+} machinery preceded the capability of contraction (as revealed by *induced contraction*). Additional responses in neighbors of target muscles suggested that dorsal abdominal muscles of the same half of one segment are interconnected. When comparing the results on contractility (this thesis) to structural data (by M. Weitkunat) we found lateral alignment and sarcomeric structures to appear after the onset of contractility, suggesting that lateral as well as sarcomeric order are enhanced by or even rely on contractions. A pre-ordering mechanism based on passive tension, which triggers the formation of immature myofibrils, was found to be conceivable.

A. Appendix: Flies

A.1. Strains and crosses

Experiments in this thesis are based on fluorescence imaging techniques. Therefore, it was necessary to use genetically altered flies as samples, which expressed a fluorophore (GFP or Cherry) in the structures of interest. All genetic alterations were realized with the GAL4-UAS-System, which is briefly explained. Afterwards all genetic constructs, all recombinated fly strains and all crosses that have been used in the course of this thesis are listed. Each strain or cross that was used in an experiment is briefly described with genotype and phenotype. All fly strains were obtained from our collaboration partners F. Schnorrer and M. Weitkunat at the Max Planck Institute of Biochemistry in Martinsried, Germany.

A.1.1. The GAL4-UAS-system

The GAL4-UAS-System is a versatile tool in *Drosophila* genetics. The key idea is that a genetic manipulation is separated into an activator, GAL4, and a target gene, UAS. GAL4 is a transcription factor from yeast. It is controlled by a promotor or enhancer, that ensures its expression in a certain pattern. For example, Mef2-GAL4 encodes for GAL4 expression in the muscles (see section A.1.3). As long as there is no suitable target for GAL4, and this is the case unless UAS is added, its expression in the fly has no effect. The second component is UAS (upstream activating sequence), which is usually cloned into a second transgenic line. In the fly UAS is silent until it gets activated by GAL4. Only then it directs the expression of the associated gene, for instance GFP, in the GAL4-imprinted pattern. [54]
In principle it is possible to clone fly strains, which contain both, GAL4 and UAS. An example is [Mef2-GAL4, UAS-GFP-Gma], which has been used in this thesis. The advantages are that time consuming crossings are not necessary, and that the strain is homozygous, which might be important for the occurrence of certain phenotypes. But the real advantage of the GAL4-UAS-system is its capability to be separated. Only then is it possible to work with otherwise lethal genotypes. Moreover since its invention in 1998 libraries of GAL4 lines and UAS lines have been created, which can be easily combined without the need of cloning every combination individually. [54]

A.1.2. Constructs

GAL4-lines

- **sr-GAL4**: Tendon cells; [92].
- **Mef2-GAL4**: Myoblasts and myotubes (all developmental stages); [92].

UAS-lines

- **UAS-GFP-Gma**: Actin; [92].
  Indirectly GFP-labeled actin via globular moesin actin binding domain (Gma).
- **UAS-GCaMP6f**: Artificial Ca^{2+} reporter protein [11]; [6].
  This UAS-construct enables visualization of calcium ions when crossed to a GAL4-strain. GCaMP6f is a genetically encoded calcium indicator. It contains a circularly permuted GFP, the calcium-binding calmodulin and the M13 peptide. The construct needs to bind a Ca^{2+}-ion to undergo a conformational change, thus enabling fluorecence. The brightness of the sample therefore depends on the presence of available Ca^{2+}-ions. [11]
- **UAS-Cherry-Gma**: Actin; [46].
  Indirectly Cherry-labeled actin via Gma.
- **UAS-CD8-Cherry**: Membrane [65].
  Indirectly Cherry labeled membrane via CD8.
- **UAS-CD8-GFP**: Membrane; [92].
  Indirectly GFP labeled membrane via CD8.
- **UAS-rhea-GFP**: Muscle ends/attachment sites [65].
- **UAS-α-tubulin-GFP**: Tubulin/Microtubules [65]. GFP-labeled microtubules and microtubule bundles.
- **UAS-β-tubulin-60D-GFP**: Tubulin/Microtubules; (fosmid: fTRG958) publication in preparation by F. Schnorrer [65].
  GFP-labeled microtubules and microtubule bundles.
- **ubi-Cad-GFP**: Cadherins [65]. GFP-labeled cadherins in epidermal cells.
- **UAS-palmitoylated-Cherry**: [26].

Others

- **w^-**: Wild type (except for white eyes).

A.1.3. Recombined constructs

This subsection presents all fly strains used in this thesis, which were recombined from the previously existing constructs listed (including references) in section A.1.2.

- **Mef2-GAL4, UAS-GFP-Gma**: homozygous; recombined by M. Weitkunat.
  All progeny of this strain express GFP-Gma in all myocites and myotubes at all times, and thus have indirectly GFP-labeled actin in all muscles.
- **Mef2-GAL4, UAS-Cherry-Gma**: homozygous; recombined by Aynur Kaya-Çopur.
  All progeny of this strain express Cherry-Gma in all myocites and myotubes at all times, and thus have indirectly Cherry-labeled actin in all muscles.

- **Mef2-GAL4, UAS-rhea-GFP**: homozygous; recombiner unknown.
  All progeny of this strain express rhea-GFP in all myocites and myotubes at all times, and thus have GFP-labeled muscle ends/attachment sites.

- **Mef2-GAL4, UAS-CD8-Cherry/TM3(Sb)**: recombined by M. Weitkunat.
  All progeny of this strain express CD8-Cherry in all myocites and myotubes at all times, and thus have indirectly Cherry-labeled membranes in all muscles.

- **y, w, UAS-CD8-GFP; y, w, UAS-CD8-GFP**: recombined by M. Weitkunat.
  The duplication of the construct increased the number of GFP molecules for a higher intensity in fluorescence microscopy.

- **y, w, UAS-CD8-GFP; Mef2-GAL4, sr-GAL4/TM3(Ser)**: recombined by M. Weitkunat.
  All progeny of this strain express CD8-GFP in all myocites and myotubes at all stages and in tendon cells, and thus have indirectly GFP-labeled membranes in all muscles and tendons.

- **UAS-palmitoylated-Cherry; Mef2-GAL4, sr-GAL4/TM3**: recombined by M. Weitkunat.
  Cherry-labeled muscles and tendons.

A.1.4. Crosses

In the following, all crosses used in the course of thesis are listed. For more information (including references) on recombined straines and original contructs see sections A.1.3 and A.1.2.

- **UAS-Gma-GFP x sr-GAL4/TM6(Tb) [♂ x ☿ & ☿ x ♂]**: Indirect GFP-labeling of actin in stripe-expressing tendon cells via GFP-Gma. Only balancer-free progeny have a GFP-label.

- **☿ y, w, UAS-CD8-GFP; y, w, UAS-CD8-GFP x ♂y, w, UAS-CD8-GFP; Mef2-GAL4, sr-GAL4/TM3(Ser)**: Indirect GFP-labeling of the membrane in stripe-expressing tendon cells and via Mef2 in muscle cells. Only balancer-free progeny have a GFP-label.

- **Mef2-GAL4 x UAS-α-tubulin-GFP**: GFP-labeled microtubules in all muscles.

- **Mef2-GAL4 x UAS-β-tubulin-60D-GFP**: GFP-labeled microtubules in all muscles.

- **Mef2-GAL4, UAS-GFP-Gma x ubi-Cad-GFP**: Indirectly GFP-labeled actin in all muscles and GFP-labeled cell-outlines via cadherins.

- **UAS-palmitoylated-Cherry; Mef2-GAL4, sr-GAL4/TM3 x UAS-GCaMP6f**: Cherry-labeled muscles and tendons, which also contain the cytosolic Ca^{2+} reporter GCaMP6f.

- **♂ y, w; *Mef2*-GAL4 x ☿ UAS-GCaMP6f**: All muscles contain the cytosolic Ca^{2+} reporter GCaMP6f.

- ♂ ***Mef2*-GAL4, UAS-Cherry-Gma x ☿ UAS-GCaMP6f**: All muscles have indirectly Cherry-labeled actin and contain the cytosolic Ca^{2+} reporter GCaMP6f.
- ♂ ***Mef2*-GAL4, UAS-CD8-Cherry x ☿ UAS-GCaMP6f**: All muscles have indirectly Cherry-labeled membranes and contain the cytosolic Ca^{2+} reporter GCaMP6f.
- ☿ **UAS-GCaMP6f x ♂ Mef2-GAL4, UAS-rhea-GFP**: All muscles have GFP-labeled muscle ends/attachment sites and contain the cytosolic Ca^{2+} reporter GCaMP6f.

A.2. Fly maintenance

Flies were kept in bottles at room temperature. Bottles with ready made standard food were obtained from the Schnorrer lab (Group of Muscle Dynamics) at the Max Planck Institute of Biochemistry in Martinsried, Germany. It was made from the ingredients listed in table A.1 [91]. Dry yeast and additional ddH_2O were added at least 1 - 2 hours before use. For crossings, inevitable anesthesia was done with CO_2.

Agar	117 g
Diamalt	400 g
Ethanol (20%)	200 ml
Maize flour	1 kg
Nipagin	25 g
Phosphoric acid	100 ml
Soya flour	100 g
Sugar beet syrup	400 g
Water	30 l
Yeast	185 g

Table A.1.: Fly food recipe. [91]

A.3. Fly sample preparation

Staging For sample preparation pupae of certain developmental stages were needed. For staging pupae were collected in the prepupa stage, which is an intermediate stage between the third instar larva and the pupa, and lasts for approximately half an hour [3]. Pupae were kept on wet filter papers in petry dishes at 27°C in a custom made incubation chamber and investigated at different points in development, given in time after *puparium* formation (APF). The incubation chamber was made from a styrofoam box equipped with copper tubing. The tubing was connected to a Julabo water bath (F10, MH controller). As the water bath was not feedback controlled by chamber temperature, room temperature was stabilized with air conditioning at 21°C to reduce temperature fluctuations. The water bath was

calibrated to maintain the required temperature with a set temperature of 28.3 °C. Room and chamber temperature were recorded with a VOLTCRAFT K202 Datalogger Thermometer to ensure temperature stability. Chamber temperature stability was compared to temperature stability in a commercially available incubator (RUMED Typ 3001, Rubarth Apparate GMBH). The custom built temperature chamber was found to have comparable mean temperature and standard deviation on a typical working day with repeated openings and closings of the lids.

Classical mounting technique Samples were prepared for live imaging according to Weitkunat *et al.* [93]: A properly aged pupa was transferred from the filter paper to a Scotch double-faced adhesive tape on a microscope slide. A small opening was cut into the pupa case right above the region of interest (DLMs in thorax or abdominal muscles). The pupa was mounted on a custom made carrier (acrylic glass) the size of a microscope slide with a furrow just wide enough to carry a pupa. The pupa was set dorsal side up but slightly turned around the long axis, such that the region of interest was facing upwards. The hole in the pupa's case was covered with 86 % glycerol to prevent drying-out and improve image quality in fluorescence microscopy. Finally, a cover slip was added and fixed with nail polish. If necessary, different pupa sizes were leveled with additional layers of cover slips as spacers between the carrier and the imaging cover slip in order to not squeeze the pupa. [93]

B. Appendix: Keratin

In vitro keratin networks were used to investigate the cutting regimes of the NDD in aqueous samples (section 2.3.4). In the following, a summary of keratin production and sample preparation is provided.

B.1. Keratin production

All steps of Keratin production followed Kayser *et al.* [39]: *E. coli* expressed human keratins K8 and K18 (BL21 cells, using the PET expression vectors) were purified and stored in 8 M urea at -80 °C. For experiments equal quantities of proteins K8 and K18 with Atto488-label were mixed. Four steps of dialysis against more and more diluted urea/TRIS buffers led to refolding of the proteins.

B.2. Keratin sample preparation

Atto488-labeled keratin and 10 fold concentrated assembly buffer (20mM Tris, pH 7.5, 10mM MgCl2, 2mM CaCl2, 2mM DTT, 5mM ATP, 1M KCl) were used for network formation in *droplet fusion technique* as developed by Kayser *et al.* [39]: Keratin network assembly happens so quickly, that it is impossible to pipette assembly buffer into a keratin solution without network formation in the pipette tip. Because network formation already starts at the very beginning of pipetting, the shear forces in the process of continuously adding buffer leads to clustering and disruption of previously formed network structures. Nevertheless, homogeneous keratin networks can be created when a droplet of 4.5 µl keratin solution on one cover slip is carefully brought into contact with a droplet of 0.5 µl buffer on a second cover slip. To ensure a three dimensional sample, silicone grease (Bayer AG) is used as spacer between (and glue) for the cover slips. Additionally the grease prevents evaporation and concomitant drift in the sample. In this way a homogeneous sample with a volume of 5 µl is formed.

C. Appendix: Nanodissection device

C.1. Hardware

The following list contains all currently used components of the NDD, as described in chapter 2.2. Listed are model numbers, manufacturer and relevant specifications.

- **Laser 355 nm** [teem photonics]: Model no. PNV-B02510-130. Repetition rates between 10 Hz and 1000 Hz, 350 ps puls length, 27 mW average power and 70 kW peak power. Only the laser head is installed on the optical table, whereas electronics and power supply are installed on a seperate table to minimize disturbances due to vibrations (fan) or heat generation.
- **Imaging laser unit of spinning disc pathway** [Acal BFi Germany]: All components were purchased from and aligned by Acal BFi.
  - **Laser 488 nm** [Cobolt AB]: Imaging laser. Model: COBOLT MLD^{TM} 60 mW 488 nm. Model no. 0488-06-01-0060-100. Couples into the SD unit via an optical fiber. Intensity control internally or with AOTF. Rated power: 63 mW, end of fiber power: 32.8 mW.
  - **Laser 561 nm** [Cobolt AB]: Imaging laser. Model: COBOLT Jive 50^{TM} 50 mW 561 nm. Model no. 0561-04-01-0050-100. Couples into the SD unit via an optical fiber. Intensity control only with AOTF possible. End of fiber power: 28.7 mW.
  - **AOTF** [Gooch & Housego]: Model no. MSD040-150-0-0.2ADM-A5H-8X1.
  - **Dichroic mirror** [not known]: not known.
  - **Optical fiber** [Qioptiq]: KINEFLEX-P-3-S-488..640-0.7-FCP8-P2.
- **Voltage supply for imaging lasers** [TTi]: QL355TP power supply.
- **Spinning disc unit** [Yokogawa Electric Corporation]: CSU-X1, manual filter holder, up to 5000 rpm.
- **Camera for confocal imaging** [Andor, Neo sCMOS]: 2560x2160 px, global and rolling shutter, trigger input and output, LabVIEW compatible.
- **Camera bright field** [Thorlabs]: CMOS sensor 1280x1024 px, monochromatic, model no. DCC1545M.
- **dichroic mirror DM1** [AHF]: F73-039.
- **dichroic mirror DM2** [AHF]: F33-356, laser beam splitter z355 RDC, # 244715.
- **Galvanometric mirrors** [Cambridge Technology (Excel Technology Europe GmbH)]: 6220HM60 Scanner with mirrors for 5 mm beam, controlled via MicroMax dual axis

servo driver (G67322H-1). Mirrors were delivered with their deviation angle calibrated on control voltage, but the calibration factor was incorrectly specified. Wiring for connection of NI-board to controller was built according to manufacturer specifications by the electronics division of the physics department of the TU Munich. Power supply: Farnell CPX400D.

- **DCm power supply for galvanometric mirrors** [TTi]: Model no. CPX400D. Provides 24 V/20 A, as required by mirror electronics.
- **F1** [AHF]: F76-366. A 364 nm long pass.
- **F2, in SD unit** [AHF, semrock]: F57-488.
- **F3** [AHF]: F39-740 (band-pass filter: 740/13).
- **Beam expander** [Sill Optics]: Model no. S6EXP0040/075. Magnification factor: 4x. With divergence correction.
- **STL1, new** [Sill Optics]: Model no. S4LFT3050/075. A fused silica telecentric f-theta lens for 355 nm. $f = 56.0$ mm.
- **STL2, new** [CVI melles griot]: LAPQ-200.0-40.0-SLMF-400-700-P. $f(248\,\text{nm} = 200.0\text{ mm} \leq f(1064\,\text{nm} = 226.1\text{ mm}$.
- **L3** [Qioptiq]: G31130600, $f = 200$ mm.
- **L4** [Qioptiq]: G31130600, $f = 200$ mm.
- **Shutters** [Servo motors, no model no. available]: Servo motors, as commonly used in rc model building, were equipped with black paper blades. Software control via custom built controllers (curtesy of Heinrich Grabmayr).
- $\lambda/2$ **plate** [Laser2000]: First order Quartz waveplate for 355 nm, model no. SIG-068-1360.
- **AOM** [AA optoelectronics, AA Sa]: The NI board in the PC did not provide enough power for the control signal (voltage) for the AOM, which resulted in wrong intensities of the laser beam. Therefore a custom built impedance converter (curtesy of Benjamin Pelz) was installed to amplify the control signal as necessary.
- **stage** [ASI]: xy-stage (S4162100FT) with integrated z-piezo (PZ-2150FT) and MS3 controller suitable for LabVIEW and manual control (joystick).
- **63x1.40 Oil λ blue** [Leica Microsystems]: Oil immersion objective, model: HCX PL APO 63x/1.40-0.60 OIL Lbd Bl, transmission at 355 nm according to specifications of technical support $T_{\text{objective}}(355\,nm) = 40\,\%$ (no error available).
- **63x1.20 Water** [Leica Microsystems]: Water immersion objective, model: HC PL APO 63x1.20 W CORR CS2. Transmission at 355 nm according to specifications of technical support $T_{\text{objective}}(355\,nm) = 40\,\%$ (no error available).
- **LED 740 nm** [ROITHNER Laser Technik]: Model no. LED740-01AU.

- **PCIe board** [National Instruments]: Board: NI PCIe-6259 M Series. 32 analog input channels, 4 analog output channels and 48 bidirectional digital channels. Connection to output boxes: Shielded cables SHC68-68-EPM. Two output boxes: BNC2110.
- **Optical Table** [Newport]: Bread board M-ST-UT2 (1100 x 2000 mm) on S-2000 stabilizer isolators with M-TBC tie bar caster system. The isolators are connected to the compressed-air system of the building to achieve damping.

C.2. Laser power measurement

It was necessary to estimate the mean power of the cutting laser that is delivered to the sample plane ($< P_{\text{sample}} >$). Mean laser powers at different positions in the optical path were measured using a PM100D power meter with a S142C sensor (Thorlabs). Due to the high peak power of the short laser pulses, the power meter was not capable of measuring the correct mean power of the laser. This problem was overcome by inserting a neutral density filter, which reduced laser intensity to a measurable amount. The filter position was right in front of the power meter sensor.
Power measurements were performed in the following way: Values from $n = 5$ power measurements at the same position were averaged to obtain the measured laser power at the respective position in the optical path. Pauses between measurements were 2 min. Measurements were carried out with 1000 Hz repetition rate and 20000 pulses. The measured value decreased during the first part of the 20000 pulse packet and increased towards the end of the packet. Therefore, the measured power was evaluated as the mean value of maximum and minimum measured power.

The transmission of the filter (T_{filter}) had to be determined experimentally because its transmission specifications were found to not apply, presumably due to the pulsed nature of the laser beam. T_{filter} was estimated from a laser power measurement ($< P_{1,+\text{filter}} >$) at the first possible position after the laser head, between the beam expander (collimation of laser beam) and the $\lambda/2$-plate (position 1; see fig. 2.1):

$$T_{\text{filter}} = \frac{< P_{1,+\text{filter}} >}{< P_1 >} = \frac{< P_{1,+\text{filter}} >}{T_{\text{BE}} \cdot < P_0 >},$$

where $< P_{1,+\text{filter}} >$ is the measured mean laser power and $< P_1 >$ is the real mean laser power. T_{BE} is the transmission of the beam expander for 355 nm according to the specifications, which was used to correct for losses in the beam expander.
The resulting value ($\pm$ standard deviation) was $T_{\text{filter}} = 11 \pm 0.08\,\%$. After evaluation of T_{filter} power measurements at any position behind position 1 are possible.

Bibliography

[1] AA Opto Electronic. Acousto-optic theory - application notes. http://www.aaoptoelectronic.com/Documents/AAOPTO-Theory2013-4.pdf, 2013. Download: Aug-07 2015, 11:00 a.m.

[2] A. Badura, X. R. Sun, A. Giovannucci, L. A. Lynch, and S. S.-H. Wang. Fast calcium sensor proteins for monitoring neural activity. *Neurophotonics*, 1(2):025008, 2014.

[3] S. P. Bainbridge and M. Bownes. Staging the metamorphosis of *Drosophila melanogaster*. *Journal of Embryology and Experimental Morphology*, 66(1):57–80, 1981.

[4] N. Q. Balaban, U. S. Schwarz, D. Riveline, P. Goichberg, G. Tzur, I. Sabanay, D. Mahalu, S. Safran, A. Bershadsky, L. Addadi, and B. Geiger. Force and focal adhesion assembly: a close relationship studied using elastic micropatterned substrates. *Nature Cell Biology*, 3(5):466 – 472, 2001.

[5] M. Bate, E. Rushton, and D. A. Currie. Cells with persistent *twist* expression are the embryonic precursors of adult muscles in *Drosophila*. *Development*, 113(1):79–89, 1991.

[6] Bloomington Drosophila Stock Center at Indiana University (NIH P40OD018537). # 42747.

[7] C. Brennan, M. Mangoli, C. E. F. Dyer, and R. Ashworth. Acetylcholine and calcium signalling regulates muscle fibre formation in the zebrafish embryo. *Journal of Cell Science*, 118(22):5181–5190, 2005.

[8] T. B. Brody. The interactive fly. URL: http://www.sdbonline.org/fly/aimain/ 1aahome.htm. Download: Apr-03 2010, 11:22 p.m.

[9] B. Bullard, Ch. Burkart, S. Labeit, and K. Leonard. The function of elastic proteins in the oscillatory contraction of insect flight muscle. *Journal of Muscle Research & Cell Motility*, 26(6-8):479–485, 2005.

[10] L. Cassimeris. Regulation of microtubule dynamic instability. *Cell Motility and the Cytoskeleton*, 26(4):275–281, 1993.

[11] T.-W. Chen, T. J. Wardill, Y. Sun, St. R. Pulver, S. L. Renninger, A. Baohan, E. R. Schreiter, R. A. Kerr, M. B. Orger, V. Jayaraman, L. L. Looger, K. Svoboda, and D. S. Kim. Ultrasensitive fluorescent proteins for imaging neuronal activity. *Nature*, 499:295 – 300, 2013.

[12] T. Chorna and G. Hasan. The genetics of calcium signaling in *Drosophila melanogaster*. *Biochimica et Biophysica Acta (BBA) - General Subjects*, 1820(8):1269 – 1282, 2012.

[13] C. A. Collins and A. DiAntonio. Synaptic development: insights from *Drosophila*. *Current Opinion in Neurobiology*, 17(1):35 – 42, 2007. Development.

[14] J. Colombelli, S. W. Grill, and E. H. K. Stelzer. Ultraviolet diffraction limited nanosurgery of live biological tissues. *Review of Scientific Instruments*, 75(2):472–478, 2004.

[15] J. Colombelli, E. G. Reynaud, J. Rietdorf, R. Pepperkok, and E. H. K. Stelzer. *In vivo* selective cytoskeleton dynamics quantification in interphase cells induced by pulsed ultraviolet laser nanosurgery. *Traffic*, 6(12):1093–1102, 2005.

[16] M. Cozhimuttam Viswanathan, G. Kaushik, A. J. Engler, W. Lehman, and A. Cammarato. A *Drosophila melanogaster* model of diastolic dysfunction and cardiomyopathy based on impaired troponin-T function. *Circulation Research*, 114(2):e6–e17, 2014.

[17] G. L. Crawford and R. Horowits. Scaffolds and chaperones in myofibril assembly: putting the striations in striated muscle. *Biophysical reviews*, 3(1):25–32, 2011.

[18] D. A. Currie and M. Bate. The development of adult abdominal muscles in *Drosophila*: myoblasts express *twist* and are associated with nerves. *Development*, 113(1):91–102, 1991.

[19] S. Morais da Silva and J.-P. Vincent. Oriented cell divisions in the extending germband of *Drosophila*. *Development*, 134(17):3049–3054, 2007.

[20] P. G. De Deyne. Formation of sarcomeres in developing myotubes: role of mechanical stretch and contractile activation. *American Journal of Physiology - Cell Physiology*, 279(6):C1801–C1811, 2000.

[21] D. Dutta, S. Anant, M. Ruiz-Gomez, M. Bate, and K. VijayRaghavan. Founder myoblasts and fibre number during adult myogenesis in *Drosophila*. *Development*, 131(15):3761–3772, 2004.

[22] D. Dutta, S. Shaw, T. Maqbool, H. Pandya, and K. VijayRaghavan. *Drosophila* Heartless acts with Heartbroken/Dof in muscle founder differentiation. *PLoS Biol*, 3(10):e337, 09 2005.

[23] D. Dutta and K. VijayRaghavan. *Metamorphosis and the Formation of the Adult Musculature*. In Sink [73], 2006.

[24] C. C. Eldred, A. Katzemich, M. Patel, B. Bullard, and D. M. Swank. The roles of troponin C isoforms in the mechanical function of *Drosophila* indirect flight muscle. *Journal of Muscle Research and Cell Motility*, 35(3-4):211–223, 2014.

[25] J. Fernandes, M. Bate, and K. Vijayraghavan. Development of the indirect flight muscles of *Drosophila*. *Development*, 113(1):67–77, 1991.

[26] D. Forster and S. Luschnig. Src42A-dependent polarized cell shape changes mediate epithelial tube elongation in *Drosophila*. *Nature Cell Biology*, 14:526 – 534, 2012.

[27] H. Fujita, T. Nedachi, and M. Kanzaki. Accelerated *de novo* sarcomere assembly by electric pulse stimulation in C2C12 myotubes. *Experimental Cell Research*, 313(9):1853 – 1865, 2007.

[28] S. Gordon and M. H. Dickinson. Role of calcium in the regulation of mechanical power in insect flight. *Proceedings of the National Academy of Sciences of the United States of America*, 103(11):4311–4315, 2006.

[29] CVI Melles Griot. All Things Photonic - the CVI Melles Griot Technical Guide. Ordered 2011.

[30] V. Hartenstein. *Atlas of* Drosophila *Development.* Cold Spring Harbor Laboratory Press, 1993. Downloaded from [8].

[31] V. Hartenstein. *The Muscle Pattern of* Drosophila. In Sink [73], 2006.

[32] S. Hebbar, R. E. Hall, S. A. Demski, A. Subramanian, and J. J. Fernandes. The adult abdominal neuromuscular junction of *Drosophila*: A model for synaptic plasticity. *Journal of Neurobiology*, 66(10):1140–1155, 2006.

[33] F. Hecht. Unpublished protocol: Embedding beads in polyacrylamide gels. July 2015.

[34] H. Holtzer, T. Hijikata, Z. X. Lin, Z. Q. Zhang, S. Holtzer, F. Protasi, C. Franzini-Armstrong, and H. L. Sweeney. Independent assembly of 1.6 µm long bipolar mhc filaments and I-Z-I bodies. *Cell Structure and Function*, 22(1):83–93, 1997.

[35] A. M. Hudson, L. N. Petrella, A. J. Tanaka, and L. Cooley. Mononuclear muscle cells in *Drosophila* ovaries revealed by GFP protein traps. *Developmental Biology*, 314(2):329 – 340, 2008.

[36] H. E. Huxley. The mechanism of muscular contraction. *Science*, 164:1356–1365, 1969.

[37] R. K. Josephson. *Comparative Physiology of Insect Flight Muscle.* In Vigoreaux [85], 2006.

[38] R. K. Josephson, J. G. Malamud, and D. R. Stokes. Asynchronous muscle: a primer. *Journal of Experimental Biology*, 203(18):2713–2722, 2000.

[39] J. Kayser, H. Grabmayr, M. Harasim, H. Herrmann, and A. R. Bausch. Assembly kinetics determine the structure of keratin networks. *Soft Matter*, 8:8873–8879, 2012.

[40] J. Kolega. Phototoxicity and photoinactivation of blebbistatin in UV and visible light. *Biochemical and Biophysical Research Communications*, 320(3):1020 – 1025, 2004.

[41] T. P. Lele, J. Pendse, S. Kumar, M. Salanga, J. Karavitis, and D. E. Ingber. Mechanical forces alter zyxin unbinding kinetics within focal adhesions of living cells. *Journal of Cellular Physiology*, 207(1):187–194, 2006.

[42] J. Limouze, A. F. Straight, T. Mitchison, and J. R. Sellers. Specificity of blebbistatin, an inhibitor of myosin ii. *Journal of Muscle Research & Cell Motility*, 25(4-5):337–341, 2004.

[43] N. Lin, N. Badie, L. Yu, D. Abraham, H. Cheng, N. Bursac, H. A. Rockman, and M. J. Wolf. A method to measure myocardial calcium handling in adult *Drosophila*. *Circulation Research*, 108(11):1306–1315, 2011.

[44] X. Ma, H. E. Lynch, P. C. Scully, and M. Sh. Hutson. Probing embryonic tissue mechanics with laser hole drilling. *Physical Biology*, 6(3):036004, 2009.

[45] M. Mayer, M. Depken, J. S. Bois, F. Juelicher, and S. W. Grill. Anisotropies in cortical tension reveal the physical basis of polarizing cortical flows. *Nature*, 467:617–621, 2010.

[46] T. H. Millard and P. Martin. Dynamic analysis of filopodial interactions during the zippering phase of drosophila dorsal closure. *Development*, 135:621–626, 2008.

[47] A. Miller. *The Internal Anatomy and Histology of the Imago of* Drosophila melanogaster.

[48] M. H. Niemz. Threshold dependence of laser-induced optical breakdown on pulse duration. *Applied Physics Letters*, 66(10):1181–1183, 1995.

[49] M. H. Niemz, editor. *Laser-Tissue Interactions. Fundamentals and Applications.* Springer-Verlag, 3rd edition, 2007.

[50] J. Noack, D. X. Hammer, G. D. Noojin, B. A. Rockwell, and A. Vogel. Influence of pulse duration on mechanical effects after laser-induced breakdown in water. *Journal of Applied Physics*, 83(12):7488–7495, 1998.

[51] J. Noack and A. Vogel. Laser-induced plasma formation in water at nanosecond to femtosecond time scales: Calculation of threshold, absorption coefficients, and energy density. *IEEE JOURNAL OF QUANTUM ELECTRONICS*, 35:1156–1167, August 1999.

[52] F. Oswald. A precise and rapid UV laser ablation system for cell biology. Diploma thesis, Technische Universität Dresden, 2010.

[53] S.J. Peterson and M.A. Krasnow. Subcellular trafficking of FGF controls tracheal invasion of *Drosophila* flight muscle. *Cell*, 160(1Ű2):313 – 323, 2015.

[54] C. B. Phelps and A. H. Brand. Ectopic gene expression in *Drosophila* using gal4 system. *Methods*, 14(4):367 – 379, 1998.

[55] T. D. Pollard and W. C. Earnshaw. *Cell Biology.* SAUNDERS-ELSEVIER, 1st edition, 2004.

[56] J. W. S. Pringle. The excitation and contraction of the flight muscles of insects. *The Journal of Physiology*, 108(2):226 – 232, 1949.

[57] J. W. S. Pringle. The bidder lecture, 1980. The evolution of fibrillar muscle in insects. 1981.

[58] A. Razzaq, I. M. Robinson, H. T. McMahon, J. N. Skepper, Y. Su, A. C. Zelhof, A. P. Jackson, N. J. Gay, and C. J. O'Kane. Amphiphysin is necessary for organization of the excitationŰcontraction coupling machinery of muscles, but not for synaptic vesicle endocytosis in *Drosophila*. *Genes & Development*, 15(22):2967–2979, 2001.

[59] S. Roy and K. VijayRaghavan. Muscle pattern diversification in *Drosophila*: the story of imaginal myogenesis. *BioEssays*, 21(6):486–498, 1999.

[60] Y. Rui, J. Bai, and N. Perrimon. Sarcomere formation occurs by the assembly of multiple latent protein complexes. *PLoS Genet*, 6(11):e1001208, 11 2010.

[61] M. Ruiz Gomez and M. Bate. Segregation of myogenic lineages in *Drosophila* requires numb. *Development*, 124(23):4857–4866, 1997.

[62] J. W. Sanger, J. Wang, Y. Fan, J. White, and J. M. Sanger. Assembly and dynamics of myofibrils. *Journal of Biomedicine and Biotechnology*, 2010:858606, 2010.

[63] V. Schaller, Ch. Weber, Ch. Semmrich, E. Frey, and A. R. Bausch. Polar patterns of driven filaments. *Nature*, 467:73 – 77, 2010.

[64] C. Schönbauer. *Genetic analysis of* Drosophila *adult muscle type specification.* PhD thesis, Ludwig-Maximilians-Universität München, 2013.

[65] F. Schnorrer. Personal communication, 2013-2015.

[66] C. Schönbauer, J. Distler, N. Jahrling, M. Radolf, H.-U. Dodt, M. Frasch, and F. Schnorrer. Spalt mediates an evolutionarily conserved switch to fibrillar muscle fate in insects. *Nature*, 479(7373):406–409, 2011.

[67] M. Schuppler, F. Keber, M. Kröger, and A. R. Bausch. Shaped actomyosin contractility. July 2015.

[68] M. Sheinman, A. Sharma, J. Alvarado, G. H. Koenderink, and F. C. MacKintosh. Active biopolymer networks generate scale-free but euclidean clusters. *arXiv:1402.2623v1 [physics.bio-ph]*, 2014.

[69] E. Shelden and P. Wadsworth. Observation and quantification of individual microtubule behavior in vivo: microtubule dynamics are cell-type specific. *The Journal of Cell Biology*, 120(4):935–945, 1993.

[70] Sigma-Aldrich. Product information: (-)-Blebbistatin. https://www.sigmaaldrich.com/content/dam/sigma-aldrich/docs/Sigma/Product_Information_Sheet/b0560pis.pdf. Download: Jun-17 2015, 10:55 a.m.

[71] Sigma-Aldrich. Product information: Dimethyl sulfoxide. https://www.sigmaaldrich.com/content/dam/sigma-aldrich/docs/Sigma/Product_Information_Sheet/d2650pis.pdf. Download: Jun-17 2015, 10:49 a.m.

[72] D. G. Simpson, M. L. Decker, W. A. Clark, and R. S. Decker. Contractile activity and cell-cell contact regulate myofibrillar organization in cultured cardiac myocytes. *The Journal of Cell Biology*, 123(2):323 – 336, 1993.

[73] H. Sink, editor. *Muscle Development in Drosophila.* Eurekah.com and Springer Science+Business Media, Inc., 2006.

[74] J. Solon, A. Kaya-Çopur, J. Colombelli, and D. Brunner. Pulsed forces timed by a ratchet-like mechanism drive directed tissue movement during dorsal closure. *Cell*, 137(7):1331 – 1342, 2009.

[75] J. C. Sparrow and F. Schöck. The initial steps of myofibril assembly: integrins pave the way. *Nature Reviews Molecular Cell Biology*, 10(4):293 – 298, 2009.

[76] Special Optics. Scanning Lens Theory. URL: http://specialoptics.com/pdf/wp_scanning_lens_theory.pdf. Download: Mar-20 2015, 02:37 p.m.

[77] M. L. Spletter and F. Schnorrer. Transcriptional regulation and alternative splicing cooperate in muscle fiber-type specification in flies and mammals. *Experimental Cell Research*, 321(1):90 – 98, 2014.

[78] J. A. Spudich. The myosin swinging cross-bridge model. *Nat Rev Mol Cell Biol*, 2(5):387 – 392, 2001.

[79] A. F. Straight, A. Cheung, J. Limouze, I. Chen, N. J. Westwood, J. R. Sellers, and T. J. Mitchison. Dissecting temporal and spatial control of cytokinesis with a myosin II inhibitor. *Science*, 299(5613):1743–1747, 2003.

[80] W. Thielicke. PIVlab 1.32. http://www.mathworks.com/matlabcentral/fileexchange/27659-pivlab-time-resolved-particle-image-velocimetry--piv--tool, 2011. Download: Feb-12 2015.

[81] O. W. Tiegs. The flight muscles of insects-their anatomy and histology; with some observations on the structure of striated muscle in general. *Philosophical Transactions of the Royal Society of London. Series B, Biological Sciences*, 238(656):pp. 221–348, 1955.

[82] N. Turner and R. Grose. Fibroblast growth factor signalling: from development to cancer. *Nature Reviews Cancer*, 10:116–129, 2010.

[83] V. Venkatachalam and A.E. Cohen. Imaging GFP-based reporters in neurons with multiwavelength optogenetic control. *Biophysical Journal*, 107(7):1554 – 1563, 2014.

[84] J. O. Vigoreaux. *Molecular Basis of Muscle Structure.* In Sink [73], 2006.

[85] J. O. Vigoreaux, editor. *Nature's Versatile Engine: Insect Flight Muscle Inside Out.* Eurekah.com and Springer Science+Business Media, Inc., 2006.

[86] V. Vishnudas and J. O. Vigoreaux. *Sustained High Power Performance: Possible Strategies for Integrating Energy Supply and Demand in Flight Muscle.* In Vigoreaux [85], 2006.

[87] A. Vogel, J. Noack, K. Nahen, D. Theisen, S. Busch, U. Parlitz, D. X. Hammer, G. D. Noojin, B. A. Rockwell, and R. Birngruber. Energy balance of optical breakdown in water at nanosecond to femtosecond time scales. *Applied Physics B*, 68(2):271–280, 1999.

[88] R. A. Walker, E. T. O'Brien, N. K. Pryer, M. F. Soboeiro, W. A. Voter, H. P. Erickson, and E. D. Salmon. Dynamic instability of individual microtubules analyzed by video light microscopy: rate constants and transition frequencies. *The Journal of Cell Biology*, 107(4):1437–1448, 1988.

[89] Q. Wang, C. Zhao, and D.M. Swank. Calcium and stretch activation modulate power generation in *Drosophila* flight muscle. *Biophysical Journal*, 101(9):2207–2213, 2011.

[90] C. A. Weber, R. Suzuki, V. Schaller, I. S. Aranson, A. R. Bausch, and E. Frey. Submitted. 2015.

[91] M. Weitkunat. *Mechanistic dissection of adult muscle formation in* Drosophila. PhD thesis, Ludwig-Maximilians-Universität München, 2014.

[92] M. Weitkunat, A. Kaya-Çopur, S.W. Grill, and F. Schnorrer. Tension and force-resistant attachment are essential for myofibrillogenesis in *Drosophila* flight muscle. *Current Biology*, 24(7):705 – 716, 2014.

[93] M. Weitkunat and F. Schnorrer. A guide to study *Drosophila* muscle biology. *Methods*, 68(1):2 – 14, 2014.

[94] N. Yoshinaga, J.-F. Joanny, J. Prost, and P. Marcq. Polarity patterns of stress fibers. *Phys. Rev. Lett.*, 105:238103, Dec 2010.

[95] W. Zhang, W. Ge, and Z. Wang. A toolbox for light control of *Drosophila* behaviors through channelrhodopsin 2-mediated photoactivation of targeted neurons. *European Journal of Neuroscience*, 26(9):2405–2416, 2007.

Acknowledgements

Bringing it to a close, I want to thank all those who accompanied and supported me during my work on this thesis:

- Prof. Andreas Bausch for his encouraging support, numerous ideas, his confidence in the project, and his enthusiasm for flies or, as he would say, ”bugs”.
- Frank Schnorrer and Manuela Weitkunat, our collaboration partners at the Max Planck Institute for Biochemistry in Martinsried, for opening the world of flies to me and for never loosing track, for the supply with a lot of hardware, particularly flies and fly food, for fruitful discussions and project ideas.
- Prof. Stephan Grill, who shared his knowledge on nanodissection devices with me.
- Heinrich Grabmayr, Benjamin Pelz, Matthias Schuppler, Uli Kleßinger, Leone Rossetti and Christine Wurm, my personal "‘technical support"’ when it came to construct the NDD.
- Carina Pelzl, my office mate, for endless discussions, for always listening to all my ”what, if” s, ”but” s and ”I dont know” s.
- Joanna Deek, for her cheerfulness, uncounted group dinners, the never ending cake supply, and for her ever available advice.
- Jona Kayser, for introducing me to keratin and to the art of froth making, and for endless discussions on basically everything.
- Fabian Hecht, Felix Keber, Katharina Henneberg and Philip Bleicher for helpful discussions.
- Pablo Fernandez, who supported me during my first steps in biophysics.
- Rudi Lehrhuber, who built half the components of the NDD.
- The TAs, for keeping the lab running, and especially Gabi Chmel for repeated fly-sitting.
- The administrative staff, for navigating me beyond the hollows of bureaucracy.
- All E27/E22 members for the fantastic atmosphere.
- My parents and Matthias, for their unlimited support, encouraging words, helpful discussions and for just being always there.

Thank you!